



Max-Planck-Institut für Metallforschung
Stuttgart

Vortex Dynamics Studied by Time-Resolved X-ray Microscopy

Kang Wei Chou

Dissertation
an der
Universität Stuttgart

Bericht Nr. 201
August 2007

VORTEX DYNAMICS
STUDIED BY
TIME-RESOLVED X-RAY MICROSCOPY

VON DER FAKULTÄT MATHEMATIK UND PHYSIK DER UNIVERSITÄT STUTTGART
ZUR ERLANGUNG DER WÜRDE EINES DOKTORS DER NATURWISSENSCHAFTEN
(DR. RER. NAT.) GENEHMIGTE ABHANDLUNG

VORGELEGT VON
KANG WEI CHOU
AUS MOUSCRON (BELGIEN)

HAUPTBERICHTER: PROF. DR. G. SCHÜTZ
MITBERICHTER: PROF. DR. M. MEHRING

TAG DER MÜNDLICHEN PRÜFUNG: 3. AUGUST 2007

MAX-PLANCK-INSTITUT FÜR METALLFORSCHUNG
STUTTGART • 2007

*“Experiments are that what you cannot explain,
theory is something you don’t understand”*

— ALEKSANDAR PUZIĆ

ACKNOWLEDGEMENTS

My deepest gratitude to Gisela Schütz, Hermann Stoll and Bartel Van Waeyenberge, without whom this work would never have been started, and Aleksandar Puzić, without whose gentle guidance and advice it would certainly never have been completed... thank you!

A sincere token of my appreciation goes to my co-examiner, Michael Mehring, and chairman, Günter Wunner, for their willingness to handle the “matter” so well and accurately under the existing time pressure.

I would also like to thank the various people who provided me with useful and helpful assistance. Without their care and consideration, this work would likely not have matured.

First I would like to thank the whole Advanced Light Source crew who provided an exquisit working place. Special thanks to the electronic workshop for being there at three in the night, and the users’ office for the lovely unnamed chit chats. To Tolek Tyliczszak, beamline scientist at the STXM, for his patience and many valuable tricks.

I would also like to use the opportunity to address the Bielefeld and Regensburg people for the careful and extremely fast sample preparation. Two persons I have to thank specifically are Georg Woltersdorf and Christian H. Back for their flexibility, great interest, and competent advice.

This is also the place to express many thanks towards the group of Joachim Stöhr. My gratitude goes especially to Yves Acremann for his valuable time helping us with the experimental setup, and Hans Christoph Siegmann for being who he is.

It would seem conspicuous if I wouldn’t certify the Max Planck Institute for Metals Research, and especially the department Schütz, so here it is. To Monika Kotz for taking care of all administrative drags with so much patience. My deep-

est sympathy and gratitude to Herrn Heinz-Dieter Carstanjen for his simplicity and his unending support, and of course for proofreading my work. To the mechanical workshop for the smaller and the bigger things. To Manfred Fähnle and Kai Fauth, for dragging them into this strange world of vortex dynamics. May it blow their heads away as it did for me.

Many thanks and much more respect to Richard Weber for being our *deus ex machina* in solving the electronic problems during all those last evenings before we had to leave on our long beamtime-journeys. Those handy hands and bright mind saved us more than once.

To my fellow measuring mates: Arne Vansteenkiste, Denis Dolgos and Edward Prabu. Do you guys also still spot bubbles and penguins everyday?

Finally, I would like to thank my close surrounding, friends and family, for always being there.

K. W. Chou ☺

CONTENTS

Acknowledgements	vii
Contents	ix
List of Abbreviations	xi
Zusammenfassung	xv
1 To cut a long story short	1
1.1 Applications of magnetism	1
1.2 Time scales in magnetism	2
1.3 Magnetic imaging techniques	4
1.4 Outline	6
2 Magnetism in confined structures	7
2.1 Magnetization precession and micromagnetics	8
2.2 The magnetic microstructure	12
2.2.1 Magnetic domains and domain walls	12
2.2.2 Magnetic thin film structures of ideally soft materials	15
2.3 Fast magnetization dynamics	16
2.3.1 Spin dynamics of the magnetic vortex state	18
2.3.2 Micromagnetic simulations	20
3 X-rays: theoretical concepts and applications	21
3.1 Interaction of photons with matter	22
3.2 Soft x-ray imaging	24
3.2.1 XMCD as magnetic contrast mechanism	24
3.2.2 X-ray microscopy methods	25
3.3 Synchrotron radiation	25
3.3.1 Undulator radiation	26
3.3.2 Monochromator	29
3.3.3 Time structure of synchrotron radiation	30
3.4 Scanning transmission x-ray microscopy	31
3.4.1 Zone plate	33

3.4.2	Detection system	35
3.5	Time-resolved scanning transmission x-ray microscopy	37
3.5.1	Sample and stripline configuration for in-plane field excitation	38
3.5.2	Excitation types	39
3.5.3	Experimental setup and data acquisition	42
4	Characterization of ferromagnetic vortex structures	47
4.1	In-plane magnetization of a vortex structure	47
4.1.1	Setup considerations	47
4.1.2	Magnetic contrast at one specific polarization	48
4.1.3	Magnetic contrast - dichroism	49
4.1.4	Element specificity	49
4.2	Out-of-plane magnetization of a vortex structure	52
4.2.1	Setup considerations	52
4.2.2	Magnetic contrast of the vortex core	52
5	Magnetization dynamics in ferromagnetic vortex structures	55
5.1	Differential imaging of magnetic vortex structures	56
5.2	Gyrotropic mode	58
5.2.1	Resonant behaviour under pulsed excitation	59
5.2.2	Resonant sine excitation	63
5.2.3	Driven oscillatory behaviour under burst excitation	70
5.3	Dynamics in coupled ferromagnetic layers	73
5.4	Non-linear response of magnetic vortex structures	75
5.4.1	Vortex core reversal by sine excitation	76
5.4.2	Hysteresis behaviour I: multiple levels	81
5.4.3	Vortex core reversal by burst excitation	83
5.4.4	Vortex core reversal – mechanism	87
5.4.5	Hysteresis behaviour II: circular structures	91
5.4.6	Hysteresis behaviour III: breaking of symmetry	94
5.4.7	Discussion	99
6	Conclusions and perspectives	103
6.1	Conclusions	103
6.2	Perspectives	104
A	The Advanced Light Source (ALS)	109
B	Stripline characterization	111

Bibliography	113
List of Figures	123
List of Tables	127
List of publications	129
Curriculum vitae	131

LIST OF ABBREVIATIONS

AC	alternating current
ALS	Advanced Light Source
APD	avalanche photodiode
DC	direct current
EPU	elliptically polarizing undulator
ECL	emitter-coupled logic
EUV	extreme ultraviolet
FIB	focussed ion beam
FMR	ferromagnetic resonance
FWHM	full width at half maximum
GMR	giant magnetoresistance
IR	infrared
LL	Landau-Lifshitz
LLG	Landau-Lifshitz-Gilbert
MFM	magnetic force microscopy
MRAM	magnetic random access memory
MOKE	magneto-optical Kerr effect
NIM	nuclear instrumentation module
OOMMF	object oriented micromagnetic framework
OSA	order-selecting aperture
PIMM	pulsed inductive microwave magnetometry
rms	root-mean-square
rf	radio frequency
SEMPA	scanning electron microscopy with spin polarization analysis
STXM	scanning transmission x-ray microscopy
SP-STM	spin-polarized scanning tunneling microscopy
SP-LEEM	spin-polarized low-energy electron microscopy
SVS	spin valve system
TRMOKE	time-resolved magneto-optical Kerr effect
TR-STXM	time-resolved scanning transmission x-ray microscopy
TEM	transmission electron microscopy

TMR	tunneling magnetoresistance
UV	ultraviolet
VUV	vacuum-ultraviolet
VNA-FMR	vector network analyzer ferromagnetic resonance
XMCD	x-ray magnetic circular dichroism
XPEEM	x-ray photo-emission electron microscopy
XTM	x-ray transmission microscopy

ZUSAMMENFASSUNG

*“...also noch einmal, du hast völlig Recht aber
gib mir ein Alternativvorschlag ...”*

— HERMANN STOLL

Fortschritte in der Herstellung nanostrukturierter magnetischer Schichten und Schichtsysteme haben in jüngster Zeit neue Entdeckungen hervorgebracht, so unter anderem den Riesenmagnet-Widerstands-Effekt (GMR: giant magnetoresistance) und das spinabhängige quantenmechanische Tunneln von Elektronen (TMR: tunneling magnetoresistance). Dadurch wurden neue Anwendungen möglich, wie die heute gebräuchlichen GMR-Leseköpfe in Festplatten oder die nichtflüchtigen magnetischen Speicher (MRAM: magnetic random access memory). Ein vollständiges Verständnis der Magnetisierungsdynamik in nanostrukturierten ferromagnetischen dünnen Schichten steht allerdings noch aus. Zudem verlangt die magnetische Datenspeicherung nach immer kleineren magnetischen Strukturen und erhöhten Schreib- und Lesegeschwindigkeiten. Möchte man dieser Entwicklung folgen, müssen neue technologische Konzepte für zukünftige Anwendungen entworfen werden. Eine gründliche Kenntnis der dynamischen Eigenschaften wird zunehmend wichtiger, wofür geeignete experimentelle Untersuchungsmethoden unentbehrlich sind. Im Rahmen der vorliegenden Arbeit wurde die Magnetisierungsdynamik an nanostrukturierter ferromagnetischen Schichten mit Hilfe eines zeitaufgelösten magnetischen Raster-Transmissions-Röntgenmikroskops (STXM: scanning transmission x-ray microscope) untersucht.

Nach einer kurzen Einführung zur Motivation der Arbeit, wird zuerst ein Überblick über die physikalisch-theoretischen Grundlagen des Mikromagnetismus gegeben, die durch die mikromagnetische Kontinuumstheorie beschrieben werden. Dabei wird sowohl auf die statische Theorie eingegangen als auch auf die dynamischen Gleichungen, die zur Lösung zeitabhängiger magnetischer Probleme benötigt werden. Danach wird die Spindynamik in magnetischen Wirbelstrukturen (Vortexstrukturen) behandelt. In ferromagnetischen Strukturen,

in deren Zentrum sich ein einzelner Vortextkern befindet, treten verschiedene Anregungsmoden auf, die durch externe zeitabhängige Magnetfelder beeinflusst werden können. Insbesondere regen sinusförmige Magnetfelder in der Strukturebene die gyrotrope Mode an, bei der die Vortexstruktur rund um das Zentrum kreiselt. Der Drehsinn dieser Bewegung hängt ausschließlich von der Richtung der Magnetisierung des Vortextkerns (Polarisation) ab, die nach oben oder nach unten zeigen kann. Am Ende dieses Abschnitts wird auf die Lösung mikromagnetischer Probleme mit Hilfe mikromagnetischer Simulationen eingegangen.

Die wichtigsten Methoden zur zeitaufgelösten Abbildung magnetischer Domänen werden im nächsten Abschnitt der Arbeit vorgestellt, darunter insbesondere die magnetische Raster-Transmissions-Röntgenmikroskopie auf der Basis des zirkularen magnetischen Röntgendichroismus (XMCD: x-ray magnetic circular dichroism). Der Aufbau des ALS Speicherrings wird beschrieben wie auch die beim Experiment verwendete Synchrotronstrahlung mit ihren herausragenden Eigenschaften. Die Implementierung zeitlich aufgelöster stroboskopischer Messungen an einem magnetischen Raster-Transmissions-Röntgenmikroskop wird dargestellt und verschiedene Anregungsarten bei stroboskopischen Messungen werden erörtert. Schnelle Magnetfeldpulse erzeugen eine breitbandige Anregung der ferromagnetischen Struktur, so dass viele Anregungsmoden beobachtet werden können. Spezifische Moden können dagegen gezielt angeregt werden mit einem Wechselfeld mit einer Frequenz nahe ihrer Eigenfrequenzen. Beide Anregungsarten lassen sich auch kombinieren, indem ein gepulstes Wechselfeld die Probe aus dem Grundzustand heraus anregt.

Im nächsten Abschnitt werden die experimentellen Messergebnisse vorgestellt und anschließend diskutiert. Die statische Magnetisierungsverteilung von Vortexstrukturen wird als erstes beschrieben. Untersucht wurden Strukturen aus Permalloy ($\text{Ni}_{80}\text{Fe}_{20}$) mit einem einzelnen Vortextkern. Dabei wurde der magnetische Kontrast sowohl in der Schichtebene als auch senkrecht dazu beobachtet und die Breite des Vortextkerns sowie der maximale magnetische Kontrast im Vortextkerns abgeschätzt. Auch Mehrschichtsysteme, bestehend aus zwei ferromagnetischen Schichten (Permalloy & Co) mit einer nichtferromagnetischen Cu Zwischenschicht, wurden untersucht. Hier treten durch die magnetische Kopplung zwischen den ferromagnetischen Schichten komplizierte Magnetisierungsverteilungen auf.

In einem weiteren Abschnitt der Arbeit werden die Ergebnisse dynamischer Messungen vorgestellt. Als erstes wird eine differenzielle Abbildungsmethode

beschrieben, mit deren Hilfe die gyrotrope Bewegung in den Vortexstrukturen mit verbessertem Signal-Rausch-Verhältnis untersucht werden können. Der magnetische Kontrast sowohl in der Schichtebene als auch senkrecht dazu wurde gemessen. Vortexstrukturen in verschiedenen Geometrien, mit unterschiedlicher Dicke und Durchmesser, wurden mit schnellen Magnetfeldpulsen angeregt. Aus dem Relaxationsprozess konnte dabei die Resonanzfrequenz abgeleitet werden. Es ergab sich ein linearer Zusammenhang zwischen der Resonanzfrequenz und der Dicke sowie dem Kehrwert des Durchmessers der Probe. Die Resonanzfrequenz verläuft auch linear mit der Dicke der Probe. Daraufhin wurde die gyrotrope Mode durch ein magnetisches Wechselfeld mit einer Frequenz in der Nähe der Resonanzfrequenz angeregt. Hierbei konnte eine Veränderung des magnetischen Kontrasts senkrecht zur Strukturebene beobachtet werden, die eine Verformung des Vortexkerns anzeigt. Die Ausdehnung der Trajektorien des Vortexkerns bei Variation der Amplitude des Wechselfeldes wurde ebenfalls untersucht. Für niedrige Amplituden ergibt sich dabei ein annähernd linearer Zusammenhang.

Nichtlineare Effekte treten bei einer leichten Erhöhung der Amplitude auf und bewirken ein Umschalten der Magnetisierungsrichtung des Vortexkerns. Dieses Umschalten konnte nachgewiesen werden sowohl über die Änderung des Drehsinns der gyrotropen Bewegung als auch direkt über die Änderung des magnetischen Kontrasts senkrecht zur Strukturebene. Die Schwellen für dieses Schalten, die für die praktische Anwendung in magnetischen Speicherelementen von großer Bedeutung sind, wurden ausführlich untersucht. Bei schneller Änderung der Amplitude des Wechselfeldes konnten Hysterese-Effekte festgestellt werden. Ein Umschalten des Vortexkerns konnte auch beobachtet werden bei Anregung durch eine einzelne Periode eines Hochfrequenzfeldes. Die Erklärung für das in dieser Arbeit beschriebene Schalten der Polarisation des Vortexkerns besteht in einer Erzeugung und Vernichtung eines Vortex-Antivortex-Paars, wie durch mikromagnetische Simulationen gezeigt werden konnte.

Die Geschwindigkeit (\sim Ausdehnung der Trajektorie) des Vortexkerns wurde als Funktion der Amplitude des Wechselfeldes bestimmt. Bei der Schaltschwellen werden Sprünge in der Geschwindigkeit beobachtet. In einem bestimmten Amplituden-Bereich stellt man auch einen großen Unterschied in der Geschwindigkeit fest, je nachdem ob der Vortexkern nach oben oder unten orientiert ist. Dieser Unterschied deutet möglicherweise auf eine Abweichung der Resonanzfrequenz der gyrotroper Mode hin, in Abhängigkeit von der Polarisation (Magnetisierungsrichtung) des Vortexkerns.

Die gyrotrope Bewegung bei Anregung mit einem Wechselfeld wurde ebenfalls in Mehrschichtsystemen, bestehend aus zwei ferromagnetischen Schichten (Permalloy & Co) und einer nichtferromagnetischen Cu Zwischenlage, untersucht. Durch die Kopplung der beiden magnetischen Schichten wird die gyrotrope Bewegung in diesen Schichten vollständig verändert. Verschiedene dynamische Effekte konnten beobachtet werden zwischen beiden ferromagnetischen Schichten, aber es handelt sich nicht mehr um eine einfache Gyrationbewegung.

Abschließend wird ein Ausblick auf zukünftige Messungen gegeben und mögliche Verbesserungen der Messanordnung erörtert.

CHAPTER 1

TO CUT A LONG STORY SHORT

“Just relax, you might enjoy it!”

— ALEKSANDAR PUZIĆ

Magnetism provided astonishing scientific discoveries combined with vast technological potential and economic impact. Recent years have seen the advent of magneto-electronics and spintronics, fields in which magnetism and solid state electronics are joined to exploit spin dependent transport processes. This creates novel electronic functionalities that in part already have entered the market, for example in hard disk read heads and non-volatile, magnetic random access memories (MRAMs). The continuing need for increasing storage density leads to smaller and smaller magnetic entities. Nevertheless, the impact of these nanomagnets is not limited to technology. At the cutting edge of research several new phenomena, such as spin-torque transfer, spin-current induced magnetic switching or spin-current induced microwave generation, have been found. Their discovery was made possible on account of the ability to fabricate magnetic nanostructures in the 100 nm range. Clearly, a challenge for the future is to understand and control magnetism and magnetic phenomena on very small time scales and in reduced dimensions. The relevant physical systems range from thin films through quantum wires and quantum dots down to individual clusters, magnetic molecules, or even single magnetic atoms on a surface.

1.1 APPLICATIONS OF MAGNETISM

A large variety of applications employs either magnetic principles, magnetic materials, or both. The continuous quest for high density, non-volatile data storage media has been stimulating major research activities in the area of magnetic thin films. More recently, the dominant driving force comes from the immense technological potential promised by spintronics, i.e. the exploitation of spin dependent electrical transport phenomena. Hallmarks in this development are

the successful implementation of hard disk read heads containing GMR (giant magnetoresistive) sensor elements and the current transition towards devices based on tunneling magnetoresistance (TMR). Another major step will be the introduction of TMR-based magnetic random access memories, which is currently pushed by all major micro-electronics companies. In basically all of these applications, nanoscale magnetic structures with a high chemical complexity constitute the essential building blocks. It is this combination of nanoscale magnetism and spintronics which currently drives the field of magnetism at an amazing speed.

Each magnetic structure is characterized by a spatial magnetization distribution, which in turn is a result of energy minimization. In very small particles, one often finds a single domain state where the magnetization is homogeneously oriented along one direction, creating a sizable magnetic stray field outside the particle. For larger particles, the stray field increases up to the point where the total energy of the system may be reduced at the expense of exchange energy by the spontaneous formation of domains, domain walls and non-collinear magnetization distributions. The details of the magnetic microstructure depend sensitively on the shape of the magnetic particle and the material parameters. As a result, one observes a large zoo of magnetic domain structures, even in the static case.

Understanding the formation of these domain structures and their dynamic response to external fields is at the heart of magnetization reversal processes. The experimental visualization of magnetic structures in both the static and dynamic case provides a major key to this understanding.

1.2 TIME SCALES IN MAGNETISM

Magnetic phenomena can be observed on time scales covering almost 30 orders of magnitude. On a larger scale, geologists find signatures of the reversal of the earth's magnetic field by measuring the direction of the magnetization of haematite (Fe_2O_3) minerals of volcanic origin in the deep sea ditch. There the gap between the continental shelves moving away from each other is being filled continuously with material from the inner earth. When this material is cooled down below its Curie temperature, the magnetization is being aligned to the direction of the magnetic field of the earth present at that time. Today, one can measure the magnetic field at the ground of the ocean and can find the magnetization direction oscillating with the distance from the deep sea

ditch, i.e. as a function of the age of the volcanic material. Over a time of several ten million years, this magnetic information has been preserved, while the external magnetic field has reversed several times, in average every 100 000 years.

Today's magnetic data storage devices keep their magnetization state several years, yet the influence of the degradation of the domain structure due to magnetic creep at the domain boundaries is already measurable. The information is stored in oppositely magnetized regions on the surface of disks coated with ferromagnetic material. After 10 years, the information stored on a floppy disk is often damaged. On magnetic audio tapes, after several years, the high frequency component of the stored music is lost because higher frequencies involve smaller magnetic domains, which degrade much faster by a slow moving of the domain walls than the larger domains representing the low frequency component of the music.

Spin glasses, in which the magnetic moments experience frustration due to a coupling with alternating sign to different neighbours, show a logarithmic relaxation time as a reaction to external field changes, which extends into an order of magnitude of seconds to hours.

The slowest mechanism of changing the magnetization state in a ferromagnetic material with an externally applied field, is the motion of magnetic domains. This corresponds to the propagation of domain walls and results in an increase in size of those domains which have a net magnetization parallel to the applied field. The mechanisms are the nucleation of domains and the propagation of domain walls. These are driven by fundamental processes like the dipolar interaction and the magnetocrystalline anisotropy. The time scale for the motion of magnetic domains varies with the structure, the exchange strength and the inhomogeneity of the material. Structural defects or chemical inhomogeneities (e.g. for alloys) tend to pin the domain walls, resulting in slower and more complex switching patterns. In weakly coupled magnetic nanoparticle arrays, characteristic time scales are seconds, while in homogeneous and clean transition metal ferromagnets, the time scale for the domain wall motion is in the μs range.

A faster mechanism concerns the reversal of a single domain or the rotation of domains with the magnetization misaligned with respect to the applied field. It occurs when the energy brought by the magnetic field overcomes the anisotropy energy barrier. The time scale associated with this mechanism (0.1 – 10 ns) depends also on extrinsic factors.

Even faster are the magnetic excitations of the electronic system. The spin wave (magnon) relaxation due to spin-lattice interactions occur on the time scale of ps. The fastest relaxation process is the relaxation of Stoner excitations. The excitation of the electronic system of a ferromagnetic material, e.g. by the absorption of photons, affects the magnetic state because the band structure for the two spin states is different. When the electronic system is heated, e.g. by a laser pulse, the magnetization is reduced and will be re-established by the transfer of energy from the electronic system to the lattice. These relaxations take place on a time scale of 100 fs.

1.3 MAGNETIC IMAGING TECHNIQUES

A large variety of imaging techniques has been developed over the years in order to visualize static magnetic structures on different length scales [1, 2]. They range from most widely used magneto-optical approaches to spin-polarized tunneling microscopy, thereby covering spatial resolution values from a few hundred nanometers down to the atomic scale. In order to meet the challenges posed by contemporary magnetic systems, the ideal magnetic imaging technique should meet as many of the following criteria as possible:

- high lateral resolution,
- strong magnetic contrast,
- well defined information depth,
- chemical selectivity,
- compatibility with external fields, and
- fast data acquisition.

Any realistic imaging approach, however, will have specific advantages and deficiencies. For example, a widely used and well established approach is Kerr microscopy [3], exploiting the magneto-optical Kerr effect (MOKE) in the visible light range. The wavelength of the applied light renders the spatial resolution of this technique, limited by diffraction effects. On the other hand, it can be conveniently used in external magnetic fields. Lorentz microscopy [4, 5], being a special variant of transmission electron microscopy (TEM), offers a high spatial resolution but requires particular sample geometries and preparation. This is necessary as the electrons have to pass through the entire sample in order to accumulate a deflection (due to the Lorentz force) or a phase difference along

the trajectory, before they are imaged. Its counterpart may be seen in scanning electron microscopy with spin polarization analysis (SEMPA), which combines high lateral resolution with high surface sensitivity [6]. Both electron based approaches are compatible with only moderate external fields.

In general, the imaging techniques may be grouped into two classes:

- In a scanning technique, the magnetic information is obtained from a point-like area of interaction between the probe and the sample. This area of interaction is then moved across the sample by scanning the probe and the sample relative to one another, and the image is constructed in a point-by-point manner. The lateral resolution is basically determined by the size of the probe or the extension of the interaction volume.
- In contrast to this stands the parallel or wide field imaging technique. In most cases it involves the irradiation of the sample with a parallel beam of photons or electrons and image a certain area (field of view) with a magnification determined by an adapted electron or light optical lens system. The lateral resolution is then basically determined by the quality of the optical system.

Scanning microscopes with tip-like probes have recently gained particular importance in magnetic imaging. One of the most widely used is magnetic force microscopy (MFM), which maps the interaction between a magnetic tip and the stray field emanated from a sample [7]. The highest lateral resolution can be achieved by means of spin-polarized scanning tunneling microscopy (SP-STM) [8, 9]. It employs the spin dependent tunneling through a vacuum gap between a magnetic tip and the investigated magnetic surface, thus a magnetic contrast can be formed. With this approach, atomically resolved imaging of magnetic moments has come within reach [10].

At first glance, wide field techniques where an image of the magnetic system is collected on an areal detector seem to be predestined for time-resolved imaging purposes. Representatives of this configuration are Kerr and Lorentz microscopies, or electron based approaches such as spin-polarized low-energy electron microscopy (SP-LEEM) [11] and x-ray photo-emission electron microscopy (XPEEM) [12, 13], as well as an all-optical x-ray imaging technique, the x-ray transmission microscopy (XTM) [14]. Nevertheless, scanning approaches have also been successfully employed for stroboscopic imaging purposes [15, 16].

1.4 OUTLINE

The main topic of this work is the study of the magnetization dynamics in thin film, confined magnetic structures with a lateral size in the micron and sub-micron range, more specifically in structures with a single vortex. The change of the magnetization distribution was investigated under the influence of a time varying magnetic field. Time-resolved measurements, based on a stroboscopic measuring scheme, were therefore implemented into a scanning transmission x-ray microscope (STXM). A time and lateral resolution of about 70–100 ps and 30–40 nm can be achieved respectively.

In Chapter 2, a brief introduction is given to the physics of magnetism and the basic concepts of magnetization dynamics. The employed experimental technique is described in Chapter 3. Special attention goes to the experimental setup for time-resolved STXM measurements, where three different excitation types were developed: pulsed, sine and burst excitation. Chapter 4 deals with the static magnetic configuration of ferromagnetic vortex structures. Single layers as well as trilayer stacks have been imaged. Results of the dynamic measurements are collected in Chapter 5. A summary with outlook finalizes this work in Chapter 6.

CHAPTER 2

MAGNETISM IN CONFINED STRUCTURES

“This is boring, yet difficult.”

— DR. NILES CRANE

Magnetic matter is characterized by the fact that it can produce by itself a magnetic field in outer space as a consequence of its atomic structure. The microscopic currents responsible for the field originate from the electronic motion inside atoms and from the electron spin angular momentum. The nature and origin of these magnetization currents are clarified in the framework of quantum mechanics. In particular, the magnetism of ferromagnetic materials is basically due to the electron spin. These quantum features can conveniently be included in the classical macroscopic Maxwell equations by postulating the existence, in addition to electric charges, of elementary magnetic moments. The description of a magnetic medium as an assembly of such elementary moments provides a convenient basis for the interpretation of many magnetic phenomena.

Given the general relationship connecting the field induction \mathbf{B} , magnetic field \mathbf{H} and the magnetization \mathbf{M} :

$$\mathbf{B} = \mu_0(\mathbf{H} + \mathbf{M}), \quad (2.1)$$

the magnetic properties of a homogeneous medium are defined once the functional dependence $\mathbf{B}(\mathbf{H})$ or $\mathbf{M}(\mathbf{H})$ are known. $\mu_0 = 4\pi \times 10^{-7} \text{ H m}^{-1}$ is the permeability of vacuum. A study of the internal structure of a given medium is then needed in order to identify the processes controlling the onset of the macroscopic magnetization \mathbf{M} and the ensuing properties of $\mathbf{M}(\mathbf{H})$. In this respect, two basic mechanisms are at the roots of the behaviour of magnetic materials; the exchange interaction and the spin-orbit interaction. The competition of the corresponding energy terms, together with the magnetostatic energy, governs the formation of magnetic domains and is eventually responsible for the hysteresis phenomena observed in magnetic materials. The theory of micromagnetics uses the different energy contributions to determine the minimum energy states of the system.

The equations that express the condition of minimum of energy for a given magnetization configuration are known as Brown's equations and serve as the basis for the interpretation of magnetic domain structures and for the analysis of those situations where the domain concept fails [17]. Brown's equations, on the other hand, neglect two other important aspects: how the system will approach equilibrium if it is not initially in equilibrium, and how the magnetization will react to a time varying applied field. The following chapter is intended to give a brief overview of the existing theories relevant to this work.

2.1 MAGNETIZATION PRECESSION AND MICROMAGNETICS

Micromagnetics is a phenomenological theory which examines ferromagnetic materials on a scale small enough to reveal details of the transition regions between domains, yet large enough to permit the use of a continuous magnetization vector rather than of individual atomic spins. It represents the link between the atomistic, quantum mechanical description of the single atoms on the one hand and the macroscopic view of a material, characterized by the shape of its hysteresis curve, on the other hand. The starting point are the elementary magnetic moments, which tend to align parallel in a ferromagnetic material due to their quantum mechanical exchange interaction. If one takes into account only the local average over the magnetic moments in a certain neighbourhood instead of the individual spins, this local average can be described by a continuous vector field \mathbf{M} . The basic assumption consists of considering that the modulus of the magnetization remains constant and all vector quantities vary slowly on the atomic scale. The discrete, quantum mechanical and statistical properties of the elementary magnets cancel out in the micromagnetic approximation and can be ignored.

For a constant applied field \mathbf{H} , the rate of change of the angular momentum \mathbf{L} ($= \mathbf{M}/\gamma_0$) is described by the torque exerted on the magnetization by the applied field. An equation can then be found governing the magnetization motion [17]:

$$\frac{d\mathbf{M}}{dt} = -\gamma_0(\mathbf{M} \times \mathbf{H}). \quad (2.2)$$

A quantum mechanical approach of a circling electron with charge q_e and mass m_e , is needed to derive a theoretical value for the gyromagnetic constant γ_0 , and is given by:

$$\gamma_0 = -\frac{\mu_0 g q_e}{2m_e} > 0, \quad (2.3)$$

with g the so-called gyromagnetic splitting factor or Landé factor ($g \simeq 2$). Multiplication of Eq. (2.2) with \mathbf{M} and \mathbf{H} respectively, assuming the applied magnetic

field is time independent, leads to

$$\frac{d}{dt}(\mathbf{M}^2) = 0 \quad \text{and} \quad \frac{d}{dt}(\mathbf{M} \cdot \mathbf{H}) = 0. \quad (2.4)$$

During motion both the modulus of the magnetization vector and the angle between the magnetic field and the magnetization remain constant. Consequently the energy $-\mu_0(\mathbf{M} \cdot \mathbf{H})$ remains unchanged.

More generally, equation (2.2) can be written as

$$\frac{d\mathbf{M}}{dt} = -(\mathbf{M} \times \boldsymbol{\omega}), \quad (2.5)$$

with

$$\boldsymbol{\omega} = \gamma_0 \mathbf{H}, \quad (2.6)$$

the angular velocity vector. Equation (2.5) simply describes an instantaneous precessional motion of the magnetization vector around $\boldsymbol{\omega}$, as sketched in Figure 2.1, i.e., $d\mathbf{M}/dt$ lies continuously in a plane perpendicular to $\boldsymbol{\omega}$.

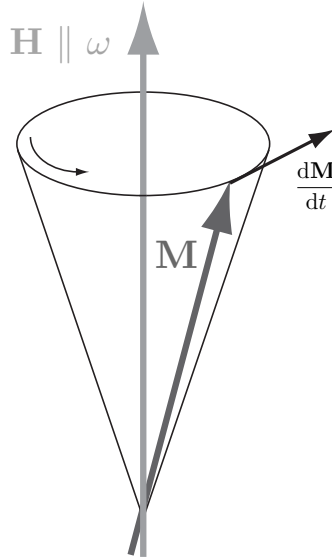


Figure 2.1: Precessional motion of the magnetization \mathbf{M} around the applied field \mathbf{H} .

Though direct use of torques is sometimes convenient, energy methods are generally more powerful. An expression is then required for the total free energy based on phenomenological expressions for the various contributions. Using variational calculus, the micromagnetic equations are derived by minimization of the total free energy with respect to the unit vector field $\mathbf{m}(\mathbf{r}, t) = \mathbf{M}(\mathbf{r}, t)/M_s$ under the constraint $\mathbf{m}^2 = 1$ [17, 18]. The resulting differential equations describe the thermodynamic equilibrium state at every point.

Energy expressions of a ferromagnet

The total free energy can be written as an integral over the sample volume:

$$E_{tot} = \int_{\Omega} (\varepsilon_{exch} + \varepsilon_{ani} + \varepsilon_{demag} + \varepsilon_{ext}) dv, \quad (2.7)$$

with the following, main contributions:

- *The exchange interaction* is a purely quantum mechanical effect and defines the spin system in a magnetic material. It is responsible for the existence of parallel, i.e. ferromagnetic, and antiparallel, i.e. antiferromagnetic, spin alignment. Deviations from the constant equilibrium magnetization direction, assuming an isotropic Heisenberg-like interaction, invoke an energy penalty

$$\varepsilon_{exch} = A_{exch} (\nabla \mathbf{m})^2, \quad (2.8)$$

where A_{exch} [J/m] is a material constant, the so-called exchange stiffness constant, which is in general temperature dependent. The exchange interaction is the strongest interaction between atoms in a ferromagnet and is the result of a correlation between the directions of the electron spins in individual atoms. It decreases rapidly (exponentially) with increasing distance between the nuclei, in contrast to the Coulomb interaction which falls off more slowly.

- In addition to the exchange interaction, there exist the magnetic dipole interaction between the magnetic moments of the atoms and the interaction between the magnetic moments and the electric field of the crystal lattice (spin-orbit interaction). Both these interactions are relativistic in origin and do not only provide a coupling of external heat sources with the spin system of the ferromagnet but also lead to the appearance of an *anisotropy energy*, i.e. the dependence of the magnetization relative to the structural axes of the material. One distinguishes crystal anisotropies of the undisturbed crystal structure, and induced anisotropies describing the effects of deviations from ideal symmetry as for example because of lattice defects or partial atomic ordering. Magnetic anisotropy arising from crystalline symmetries is referred to as magnetocrystalline anisotropy. Expansions in terms of powers of the components of \mathbf{m} are used to describe the most important contributions. Rarely more than the first two significant terms have to be considered, since thermal agitation of the spins tends to average out the higher order contributions. In a cubic crystal the energy density due to crystal anisotropy reads

$$\varepsilon_{ani}^c = K_1^c (m_x^2 m_y^2 + m_x^2 m_z^2 + m_y^2 m_z^2) + K_2^c m_x^2 m_y^2 m_z^2, \quad (2.9)$$

where m_i ($i = x, y$ and z) are the magnetization components along the cubic axes. K_1^c and K_2^c are the temperature dependent anisotropy coefficients in J/m^3 . For crystals exhibiting uniaxial anisotropy, the energy density is

$$\varepsilon_{ani}^u = K^u(1 - (\mathbf{m} \cdot \mathbf{u})^2), \quad (2.10)$$

with K^u again the anisotropy constant in J/m^3 , and \mathbf{u} defining the easy axis direction.

- A ferromagnetic body with net magnetization \mathbf{M} generates a magnetic field \mathbf{H} by itself. This is a direct consequence of the *magnetic dipole interaction*. The generated field \mathbf{H} satisfies the equations of magnetostatics:

$$\nabla \times \mathbf{H} = 0,$$

$$\nabla \cdot \mathbf{B} = \nabla \cdot (\mu_0 \mathbf{H} + \mathbf{M}) = 0,$$

as well as the continuity conditions on the boundary of the ferromagnet. The demagnetization field \mathbf{H}_d is defined by the field generated by the divergence of the magnetization \mathbf{M} :

$$\nabla \cdot \mathbf{H}_d = -\nabla \cdot (\mathbf{M}/\mu_0).$$

The sinks and sources of the magnetization act like positive and negative “magnetic charges” for the stray field. The energy connected to the stray field is

$$\varepsilon_{demag} = -\frac{1}{2}\mu_0(\mathbf{M} \cdot \mathbf{H}_d) = -\frac{1}{2}\mu_0 M_s(\mathbf{m} \cdot \mathbf{H}_d). \quad (2.11)$$

- The interaction of the magnetization vector field with an external field \mathbf{H}_{ext} is called the *Zeeman interaction* and its corresponding energy contribution is given by

$$\varepsilon_{ext} = -\mu_0(\mathbf{M} \cdot \mathbf{H}_{ext}) = -\mu_0 M_s(\mathbf{m} \cdot \mathbf{H}_{ext}). \quad (2.12)$$

For a uniform external field this energy depends only on the average magnetization and not on the particular domain structure or the sample shape. The Zeeman interaction of a magnetic moment is of great practical importance because it is used to align magnetic materials. In particular, if one wants to align a magnetic material in the hard direction, the Zeeman interaction has to overcome the spin-orbit interaction which determines the magnetocrystalline anisotropy.

2.2 THE MAGNETIC MICROSTRUCTURE

The macroscopic properties of a magnetic material are explained by the magnetic microstructure. Magnetic domains and the transition regions between the domains, called magnetic domain walls, are the elements of the magnetic microstructure. In most of the domain theory developed in the 1930's, domains were simply postulated and no attempt was made to explain their existence. Internal magnetostatic energies were also ignored but the work from Landau & Lifshitz [19] brought new insights in the domain theory with greater emphasis on magnetostatic energy and on the details of the domain geometry. A comprehensive review of the physical principles of domain theory along with the crucial experiments bearing the foundations of the subject can be found in the early work of Charles Kittel [20]. The work from Alex Hubert & Rudolf Schäfer provides a detailed description of magnetic domain structures [1].

2.2.1 Magnetic domains and domain walls

If the magnetic anisotropy would be the only energy determining the direction of the magnetization, a magnetic sample would tend, due to the exchange energy, to be homogeneously magnetized along one of its easy directions (Figure 2.2 (a)). However, depending on its physical shape, a homogeneously magnetized sample will have so-called magnetic surface charges, generating a magnetic stray field. The generation of such a magnetic field costs energy according to Eq. (2.11). The importance of this energy term increases gradually as the particle size increases. To reduce this energy, the magnetization will split up into domains, i.e., it will prefer to lie in multiple directions in order to minimize the stray field (Figure 2.2 (b)–(e)).

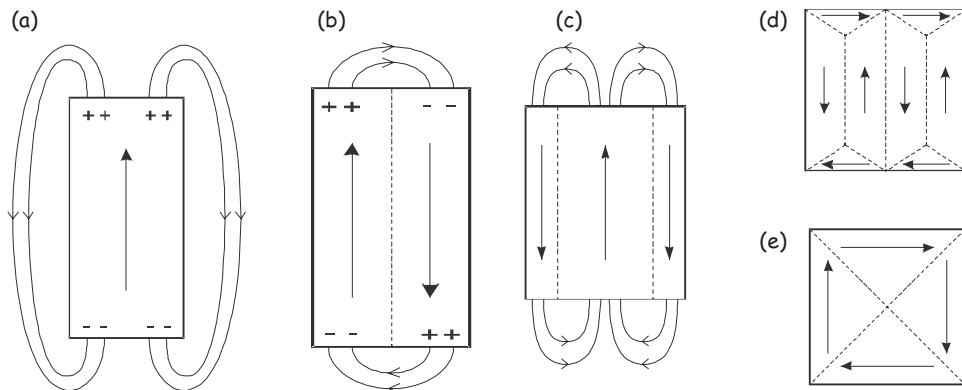


Figure 2.2: Illustration of the formation of domains and the corresponding stray field (a)–(c). Closure domains are formed to avoid any stray field (d) & (e) (taken from [21]).

In the presence of domains there have to be transitions from one direction of the spontaneous magnetization into another one. These transitions occur in domain walls, but the formation of the domain walls cost some energy as well. Small magnetic particles can thus support a domain wall if the stray field energy is larger than the wall energy. The calculation of domain walls is relatively easy for sufficiently extended and flat walls, using the methods of variational calculus, as first demonstrated by Landau & Lifshitz [19]. The treatment of two- and three-dimensional walls is more difficult but still possible. For example the internal structure of domain walls is different at the surface compared to the bulk, and it also changes with two-dimensional samples compared to three-dimensional samples.

Two common types of planar 180° domain walls are illustrated in Figure 2.3 for an infinite uniaxial medium separating two domains of opposite magnetization. In a Bloch wall, common in thick films, the magnetization rotates gradually in a plane parallel to the plane of the domain wall. In a Néel wall, favourable in very thin films, the magnetization rotates in a plane perpendicular to the wall, i.e. within the surface plane, avoiding in this way the creation of a stray field.

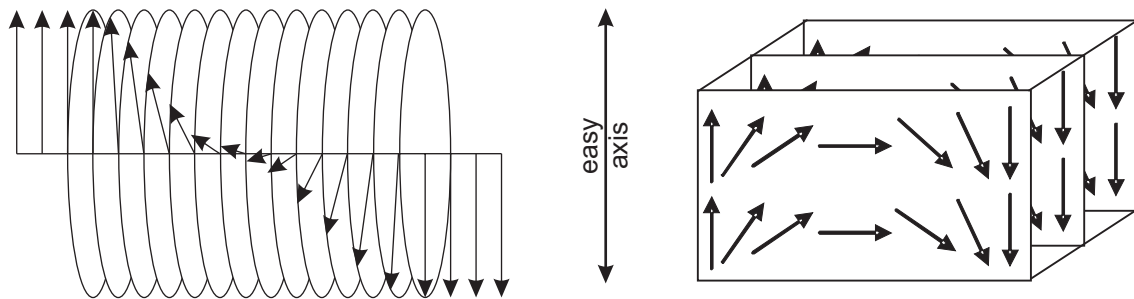


Figure 2.3: Sketch of the magnetization distribution in a Bloch wall (left panel) and Néel wall (right panel) (taken from [21]).

The properties of a domain wall are determined by the competition between the exchange energy and the magnetic anisotropy energy. The domain wall energy increases with both the exchange energy and the anisotropy energy, because both favour a collinear moment alignment. The domain wall width increases with the exchange energy but decreases with increasing magnetic anisotropy energy.

A wide range of scales appear in magnetic microstructures to classify certain general aspects of interest. The thickness δ_W for a Bloch wall can be calculated through energy considerations and is given by:

$$\delta_W = \pi \ell_W = \pi \sqrt{\frac{A_{exch}}{K^u}}, \quad (2.13)$$

with ℓ_W the Bloch wall thickness parameter, and is often also called the exchange length. Generally, for bulk material, this length gives the distance over which the magnetization is expected to change direction in the presence of magnetic anisotropies.

In thin films another scale ℓ_s is used for the exchange length, which reflects the exchange energy when it is in equilibrium with the stray field energy, and reads:

$$\ell_s = \sqrt{\frac{A_{exch}}{K^s}} = \sqrt{\frac{2A_{exch}}{\mu_0 M_s^2}}, \quad (2.14)$$

where $K^s = \mu_0 M_s^2/2$ is the stray field energy constant. A feature with this characteristic length is for instance the core of a magnetic vortex where the magnetization is perpendicular to the surface.

Both exchange lengths give a measure for the extent of the exchange interaction, thus the homogeneity of the magnetization. A quality factor Q can then be defined as a natural measure of the relative strength of anisotropy and stray field effects, and is defined by:

$$Q = \frac{K^u}{K^s} = \frac{2K^u}{\mu_0 M_s^2}. \quad (2.15)$$

Stray field effects dominate in soft materials with low magnetic anisotropy, for which $Q \ll 1$. Conversely, anisotropy tends to dominate in hard magnetic materials, where $Q \gtrsim 1$. Table 2.1 shows typical material parameters for several magnetic materials with Permalloy ($\text{Ni}_{80}\text{Fe}_{20}$) and $\text{Nd}_2\text{Fe}_{14}\text{B}$ examples of soft and hard magnetic materials, respectively [22, 23, 24].

Material	T_c [K]	$\mu_0 M_s$ [T]	A_{exch} [10^{-11} J m $^{-1}$]	K^u [10^5 J m $^{-3}$]	ℓ_W [nm]	ℓ_s [nm]	Q
Fe	1044	2.16	1.5	0.48	18	2.8	0.0259
Co	1398	1.82	1.5	5	5.5	3.4	0.3794
Ni	627	0.62	1.5	-0.057	51	9.9	0.0373
$\text{Ni}_{80}\text{Fe}_{20}$	869	1	1.3	5×10^{-3}	161	5.7	0.0013
$\text{Nd}_2\text{Fe}_{14}\text{B}$	585	1.61	0.77	44.4	1.3	2.7	4.3049

Table 2.1: Typical material parameters for several magnetic materials (with T_c the Curie temperature) [22, 23, 24].

2.2.2 Magnetic thin film structures of ideally soft materials

Magnetic films are defined as thin if their thickness is comparable to the Bloch wall width. Here the case for negligible anisotropy (i.e. $Q \ll 1$) is considered, where the patterns can be described as a two-dimensional system. Then, the energy contributions to be taken into account are the magnetic field energy terms and the exchange energy.

For sufficiently *small particles*, no domain structure will develop. The argument is the same as for high anisotropy materials (Figure 2.2 (a)). Only the magnetic stray field is favouring a non-uniform magnetization but it becomes effective only at large distances. The critical size for single domain particles can be calculated with a three-dimensional micromagnetic analysis [25, 26].

For dimensions of the specimen larger than the single domain limit, *closed-flux magnetization configurations* with vanishing stray field energy are favoured (Figure 2.2 (d) & (e)). A comprehensive analysis of such thin film elements of arbitrary shape was achieved by van den Berg [27, 28, 29]. The possible magnetization configurations in the system can be translated in an elegant mathematical procedure, based on the pole avoidance principle, using $\nabla \cdot \mathbf{M} = 0$ with $\mathbf{m}^2 = 1$, and $\mathbf{m} \cdot \mathbf{n} = 0$ at the film edge where \mathbf{n} is the unit vector normal to the film edge. These conditions can only be met if the magnetization stays parallel to the edges at every point along an edge-normal as long as no other edge interferes.

In square-shaped or circular patterns, depending on their lateral size and thickness, the closed-flux magnetization distribution results in a swirling magnetization and the magnetization turns perpendicular to the surface at the centre, thus avoiding the singularity (Figure 2.4). The configuration generates a strong

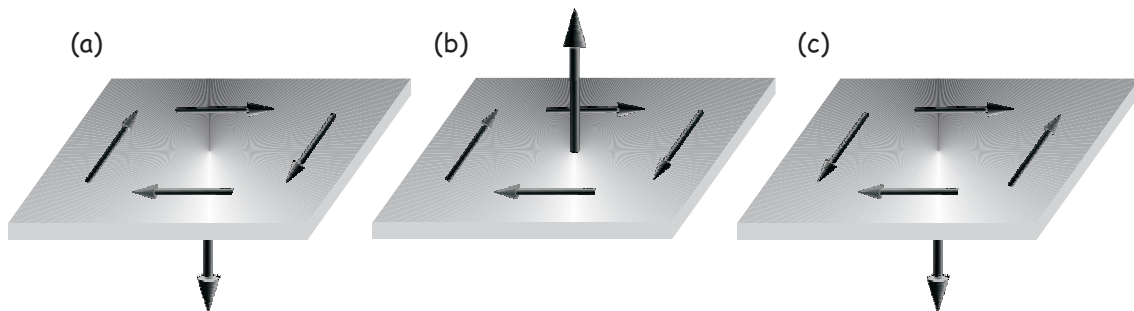


Figure 2.4: Illustration of magnetic structures with a single vortex with core magnetization pointing down (a) & (c), and up (b). The arrows sketch the direction of the magnetization distribution in the structures for circular magnetization (a) & (b) and crossed magnetization (c).

local stray field but is continuous and non-singular. The closed-flux configuration in those structures minimizes the cross-talk between neighbouring patterns and exhibits a high thermal stability. Square-shaped vortex structures, or also called Landau patterns, have four triangular domains separated by 90° Néel walls, and at the centre the magnetization turns perpendicular to the plane. The size of the core depends on the material parameters and the sample geometry. Analytical models [25, 30] were developed and micromagnetic simulations [30] were performed to describe the magnetization distribution $\mathbf{M}(\mathbf{r})$ in zero field for Permalloy nanodots with a radius of 100 nm and a thickness of 20 nm, and the calculated size of the magnetic vortex core ranges from 12–18.5 nm. Experimental results using spin-polarized scanning tunneling microscopy (SP-STM) on Fe islands with lateral dimensions of 200 to 500 nm by 150 to 250 nm along the [001] and the [110] direction, respectively, and an average thickness of 8 to 9 nm. even suggest a width of about 10 nm [31].

The direction of the out-of-plane component of the magnetization in the core is defined as the polarization (down & up in Figure 2.4 (a) & (b), respectively) and forms together with the sense of the in-plane flux closure (clockwise/counter-clockwise) a ground state configuration with fourfold degeneracy. A magnetic vortex can thus in principle store two bits of information: the sense of the in-plane flux closure can be used as an information carrier, and the out-of-plane polarization of the magnetic vortex core can also be regarded as a 0 or 1 of a bit element [26]. For data storage, a practical way of switching between these binary states is required. Magnetic fields needed to switch the corresponding states are in the order of 4 MA/m ($\hat{=} 0.5$ T) [32, 26, 33].

2.3 FAST MAGNETIZATION DYNAMICS

The rate of change of the angular momentum was described by Eq. (2.2) and is given by the torque exerted by the field on the magnetization. The reaction of a ferromagnetic system on a fast change of the field, e.g. by a field pulse applied opposite to the magnetization direction or by a time varying magnetic field in the GHz range, is classically described by the torque of the magnetic field component, perpendicular to the magnetization direction, on the magnetization. The equation of motion of the magnetization \mathbf{M} reads thus as:

$$\frac{\partial \mathbf{M}}{\partial t} = -\gamma_0 (\mathbf{M} \times \mathbf{H}_{\text{eff}}), \quad (2.16)$$

with the effective field \mathbf{H}_{eff} , the relevant field exerting a torque, defined as:

$$\mathbf{H}_{\text{eff}} = -\frac{1}{\mu_0 M_s} \frac{\delta \varepsilon}{\delta \mathbf{m}}. \quad (2.17)$$

This equation describes a purely precessional motion around the effective field direction.

Over a limited range of frequencies the departure from isothermal conditions, with resulting irreversibility, is taken into account by inclusion of a phenomenological damping term in the equation of motion. This allows a precessing magnetization vector to lose energy and thus approach its static equilibrium direction along \mathbf{H}_{eff} (Figure 2.5). T. L. Gilbert introduced such damping term with a suitable Rayleigh dissipation function to the effective field \mathbf{H}_{eff} of the form [34]:

$$\mathbf{H}_{\text{eff}} \rightarrow \mathbf{H}_{\text{eff}} - \frac{\alpha}{\gamma_0 M_s} \frac{\partial \mathbf{M}}{\partial t}, \quad (2.18)$$

with α a dimensionless damping constant. The insertion of former expression into Eq. (2.16) leads to the well known Landau-Lifshitz-Gilbert equation (LLG) [34]:

$$\frac{\partial \mathbf{M}}{\partial t} = \underbrace{-\gamma_0 (\mathbf{M} \times \mathbf{H}_{\text{eff}})}_{\text{precessional term}} + \underbrace{\frac{\alpha}{M_s} \left(\mathbf{M} \times \frac{\partial \mathbf{M}}{\partial t} \right)}_{\text{damping term}}. \quad (2.19)$$

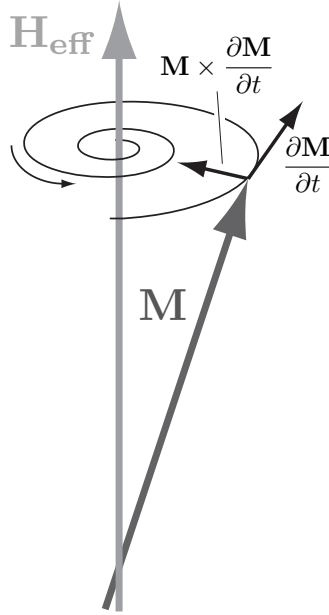


Figure 2.5: Damped precessional motion of the magnetization \mathbf{M} around the effective field \mathbf{H}_{eff} .

Multiplication of the LLG Eq. (2.19) on both sides with $\mathbf{M} \times$ gives the Landau and Lifshitz formulation (LL) [19]:

$$\mathbf{M} \times \frac{\partial \mathbf{M}}{\partial t} = -\gamma_0 \mathbf{M} \times (\mathbf{M} \times \mathbf{H}_{\text{eff}}) - \alpha M_s \frac{\partial \mathbf{M}}{\partial t}, \quad (2.20)$$

and substitution of the right-hand side of this equation in the LLG equation, leads to

$$\frac{\partial \mathbf{M}}{\partial t} = -\gamma_0^* (\mathbf{M} \times \mathbf{H}_{\text{eff}}) - \lambda [\mathbf{M} \times (\mathbf{M} \times \mathbf{H}_{\text{eff}})], \quad (2.21)$$

with

$$\gamma_0^* = \frac{\gamma_0}{1 + \alpha^2} \quad \text{and} \quad \lambda = \frac{\alpha}{1 + \alpha^2} \frac{\gamma_0}{M_s}. \quad (2.22)$$

The previous Eq. (2.22) shows that the corresponding values in both descriptions are the same only in the limit for small damping.

Furthermore, the relaxation mechanisms in these systems can be divided into intrinsic and extrinsic processes. Unavoidable processes, like the direct coupling of magnons to the lattice via spin-orbit interactions, and eddy currents mediated by free electrons present in conducting materials, are referred to as intrinsic processes. Scattering processes due to sample imperfections leading to magnon-magnon scattering are extrinsic contributions to the damping. In practice, conventional ferromagnetic resonance (FMR), vector network analyzer ferromagnetic resonance (VNA-FMR), pulsed inductive microwave magnetometry (PIMM) and time-resolved magneto-optic Kerr effect (TRMOKE) are the main methods used to study the damping mechanisms in ferromagnetic systems [35].

2.3.1 Spin dynamics of the magnetic vortex state

So far, magnetization dynamics was discussed in the limit of uniform precession of the magnetization throughout the sample volume. The so-called uniform mode implies that all magnetic moments precess at the same frequency and phase. However, higher order excitations may cause the magnetic moments to precess with the same frequency but at different phases and are referred to as spin waves. Since the exchange interaction acts on a short range compared to the dipolar interaction, spin waves can be classified into dipole and exchange dominated waves, depending on their wavelength. In the long wavelength range, spin waves are dipole dominated and referred to as magnetostatic. In contrast, for small wavelengths the spin wave properties are dominated by the exchange interaction. In this case it is simply referred to as spin waves.

The vortex magnetization distribution leads, due to its confinement, to a considerable spin wave spectrum with azimuthal and radial modes, and additional low frequency modes corresponding to the displacement of the vortex as a whole [36, 37, 38, 39]. The gyrotropic mode belongs to the latter case and can be observed by applying an in-plane field pulse to a vortex structure. The structure starts subsequently to gyrate as a whole around its centre [40]. The higher frequency modes appear then as low-amplitude oscillations superimposed on the gyrotropic motion [41, 42]. Domain walls, present in Landau flux-closure structures, bring an additional excitation spectrum. The excitation of a domain wall appears in an oscillation, analogous to an excited string, but complicated by the fact that one of the end points – the vortex core – is moving [41, 43].

Starting from the LLG formulation (Eq. (2.19)), a theory of the dynamics of micromagnetic structures, like domain walls and bubble domains, was introduced by Thiele [44, 45], and applied by Huber to the dynamics of vortices [46, 47]. The vortex mass M was accounted by Wysin [48], and the equation of motion of a vortex under influence of an external force \vec{F} is given at the vortex position \vec{X} by:

$$\vec{F} + \vec{G} \times \vec{V} = M\dot{\vec{V}}, \quad (2.23)$$

with the vortex moving at velocity $\vec{V} = \dot{\vec{X}}$. The right-hand term in Eq. (2.23) is analogous to the classical acceleration term. A moving magnetic vortex experiences a gyroforce $\vec{G} \times \vec{V}$ with \vec{G} the gyrovector. Considering the continuum description in a two-dimensional classical easy-plane ferromagnetic spin system, introduced by Hikami and Tsuneto [49], the gyrovector can be evaluated as:

$$\vec{G} = -2\pi pq\vec{e}_z, \quad (2.24)$$

where q is the topological vorticity, p the vortex core polarization and \vec{e}_z a unit vector in the out-of-plane direction. The topological vorticity $q = -1$ gives an antivortex structure with crossed magnetization distribution (Figure 2.4 (c)), but only the vortex structure with topological vorticity $q = +1$ appears in the ground state configuration (Figure 2.4 (a) & (b)). The dynamic response of a vortex structure ($q = +1$) to fast externally applied magnetic fields will therefore “force” the out-of-plane vortex core to perform a gyrotropic motion where the sense of gyration is only determined by its polarization p (Figure 2.6).

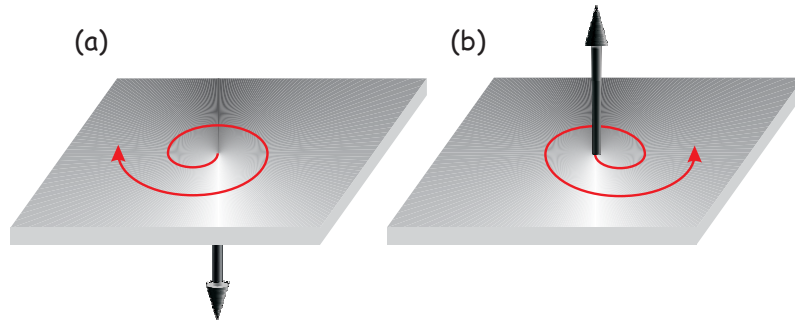


Figure 2.6: Illustration of the relation between the sense of gyration of a magnetic Landau structure and the direction of the out-of-plane vortex core magnetization. The vortex here gyrates clockwise for the core magnetization pointing down (a), and counterclockwise for the core pointing up (b).

2.3.2 Micromagnetic simulations

Study of the dynamic response of the magnetization in ferromagnetic elements requires the use of micromagnetic simulations to confirm the experimentally obtained data. The magnetic sample is therefore divided into small cells with uniform magnetization. For each cell the effective field \mathbf{H}_{eff} is calculated including external fields, nearest neighbour exchange interactions, local anisotropy, and dipolar interactions. Combining Maxwell's equations and the LL equation (Eq. (2.21)), both the magnetostatic fields and the temporal evolution of the magnetization can be calculated. The dynamic response is obtained by numerical integration of the equations of motion after disturbing the equilibrium configuration with an external field. When comparing the experimental results to the simulated data one has to keep in mind that simulations assume an ideal system without taking into account fluctuations of the magnetic properties of the sample. The numerical results presented in this thesis are obtained with the Object Oriented Micromagnetic Framework (OOMMF) programme [50].

CHAPTER 3

X-RAYS: THEORETICAL CONCEPTS AND APPLICATIONS

“Dit is niets anders dan een low level discriminator!”
— BARTEL VAN WAEYENBERGE

A portion of the electromagnetic spectrum from the infrared (IR) to the x-ray regions is depicted in Figure 3.1. The region between the ultraviolet and x-ray radiation is a region with a large number of atomic resonances. The x-ray energy is tuned to the absorption edge of a magnetic atom, and magnetic studies are done by looking at its core to valence transitions. The resonant x-ray signal is element and even chemical state specific since core-level binding energies depend on the atomic number and the chemical state. In addition, the measured resonant x-ray intensity is quantitatively linked by sum rules with the spin and orbital magnetic moments since it measures wavevector integrated properties of the valence shell, in contrast to optical methods which measure specific wavevector

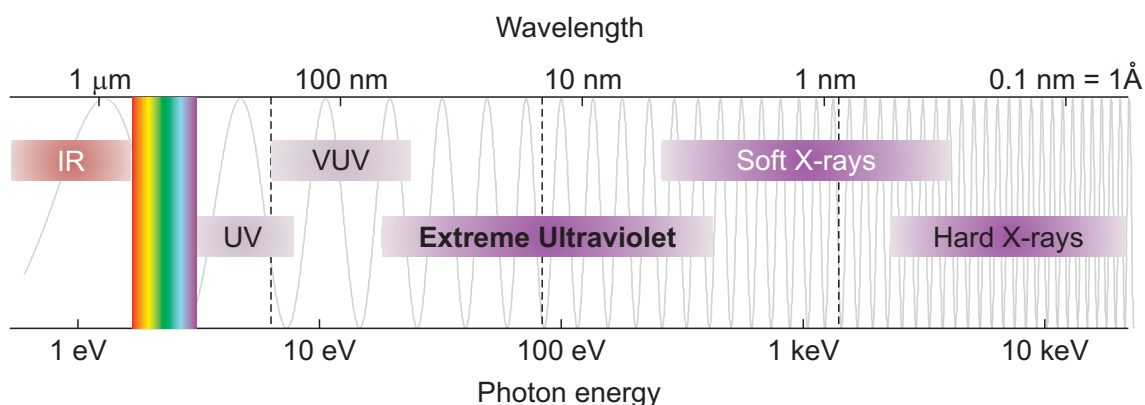


Figure 3.1: A portion of the electromagnetic spectrum from the infrared (IR) to the x-ray regions is depicted. Visible light is shown with red (650 nm), green (530 nm), and blue (470 nm) wavelengths. At shorter wavelengths are ultraviolet (UV) radiation, extreme ultraviolet radiation, soft x-rays, and hard x-rays. The vacuum-ultraviolet (VUV) radiation is the portion of the UV spectrum below 190 nm, where air and all materials are absorbing.

dependent transitions. Finally, as dimensions reduce down below 100 nm, visible light becomes insufficient and one needs shorter wavelength x-rays to study the magnetic nanostructures.

Theoretical concepts of the interaction of photons with matter are described in this chapter, and how this is providing a method to study ferromagnetic materials. Especially the discovery of the x-ray magnetic circular dichroism (XMCD) and its use in x-ray microscopy will be accounted. Therefore soft x-ray sources are needed which is at one's disposal at synchrotron radiation facilities. A detailed description of the implementation of time-resolved techniques into a scanning transmission x-ray microscope (STXM), to study the magnetization dynamics in ferromagnetic systems, is closing this chapter.

3.1 INTERACTION OF PHOTONS WITH MATTER

An incident beam with intensity I_0 is attenuated upon transmission through a sample with linear absorption coefficient $\mu(E, Z)$ (in m^{-1}), with $\mu(E, Z)$ independent of the depth x (in m), according to:

$$I(x) = I_0 e^{-\mu(E,Z)x}. \quad (3.1)$$

The x-ray absorption intensity $I(x)$ is strongly dependent on the photon energy E and the atomic number Z , and a quantitative analysis requires quantum mechanics in conjunction with time dependent perturbation theory. In a one-electron picture, the resonant absorption process is described by the incident photon with energy $\hbar\omega$ exciting a core electron in an atom from its initial state $|i\rangle$ at energy E_i to a higher lying final empty state $|f\rangle$ at energy E_f , and the transition probability per time unit or transition rate τ_{if} is given by Fermi's Golden rule:

$$\tau_{if} = \frac{2\pi}{\hbar} |\langle f | \mathbf{H}_{int} | i \rangle|^2 \delta(\hbar\omega - E_f + E_i) \rho_f(E), \quad (3.2)$$

with $\rho_n(E_n)$ denoting the density of levels on the energy scale, so that $\rho_n(E_n)dE_n$ is the number of final states n in an interval dE_n containing the energy E_n , and \mathbf{H}_{int} the interaction Hamiltonian describing the electron-photon interaction. This interaction term does not only provide the selection rules but its spin dependence also forms the basis of dichroic effects [51, 52, 53].

Optical effects are mainly described phenomenologically by means of a refractive index n . In general, this index is dependent on the frequency and polarization of the electromagnetic wave. For a given sample, the frequency dependence is

particularly important around specific resonance frequencies and near such resonances, the refractive index needs to be described as a complex dimensionless quantity according to [54, 55, 56]:

$$n(\omega) = 1 - \delta(\omega) + i\beta(\omega). \quad (3.3)$$

The real part $\delta(\omega)$ is associated with refraction and the imaginary part $\beta(\omega)$ with absorption of the electromagnetic wave in the medium. The absorptive part of the refractive index is connected to the absorption coefficient $\mu(E, Z)$ by the following relation:

$$\mu(E, Z) = 4\pi \frac{\beta(\omega)}{\lambda}, \quad (3.4)$$

with λ the wavelength of the photons. The polarization dependence of the refractive index is called “birefringence”. The polarization dependence of the absorptive part $\beta(\omega)$ is referred to as “dichroism”.

There are four main types of dependence of the photon absorption on the polarization. Linear dichroism and (natural) circular dichroism depend on the charge distribution. Magnetic linear dichroism and magnetic circular dichroism depend on the spin and charge distribution. This work is restricted to the use of x-ray magnetic circular dichroism (XMCD) where the absorption is different for left and right circularly polarized photons. Consider the 3d transition metals as an example (Figure 3.2), the magnetic properties are mainly determined by their d valence electrons. The XMCD effect arises during the excitation of $2p$ core elec-

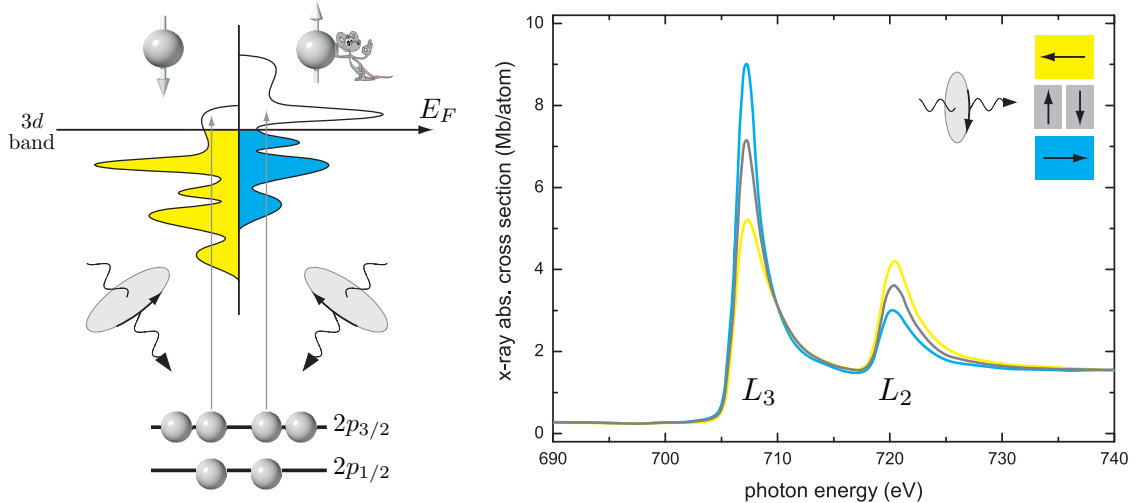


Figure 3.2: Illustration of the XMCD effect for the absorption at the L edge in Fe. The experimental data on the right are from Chen et al. [57] and have been corrected to correspond to 100% circular polarization. The case of circularly polarized x-rays with positive helicity is shown and the color coded spectra correspond to the shown sample magnetization directions.

trons to unfilled $3d$ valence states. Due to the spin-orbit coupling, the $2p$ level is split to a $2p_{3/2}$ level (L_3 edge) and a $2p_{1/2}$ level (L_2 edge). Conservation of angular momentum requires a transfer of the angular momentum of the incident circularly polarized x-rays to the excited photoelectrons. If the photoelectron is excited from, e.g. the $2p_{3/2}$ level, the angular momentum of the photon can be transferred in part to the spin through the spin-orbit coupling and the excited photoelectrons are spin polarized. The spin polarization is opposite for incident x-rays with positive ($+\hbar$) and negative ($-\hbar$) photon spin. Also, since the $2p_{3/2}$ and $2p_{1/2}$ levels have opposite spin-orbit coupling ($l + s$ and $l - s$, respectively) the spin polarization will be opposite at the two edges. In a second step the photoelectrons are excited to different final states as the exchange split valence shell causes unequal spin-up and spin-down populations. Therefore, one gets different absorption spectra if the magnetization is either parallel or antiparallel to the light polarization.

3.2 SOFT X-RAY IMAGING

3.2.1 XMCD as magnetic contrast mechanism

Circularly polarized x-rays are provided at synchrotron radiation facilities. When the photon energy is tuned to a prominent resonance in the x-ray absorption spectrum, like the L_3 or L_2 edges in the transition metals [58, 57] or the M_5 or M_4 edges for the rare earths [59], a large dichroism exists for magnetic materials, as described above. In general, this effect depends on the orientation of the photon polarization relative to the magnetic orientation, with a $\cos \vartheta$ dependence of the dichroism intensity [60], ϑ being the angle between the photon angular momentum and the sample magnetization. By tuning the photon energy to a specific absorption edge and fixing the photon polarization, a sample containing several microscopic regions with different magnetic orientations can be probed. The signal from the different regions will vary because of the dichroic absorption effect. In a transmission experiment, the absorption will thus be different in the different regions depending on the orientation of the magnetization with respect to the incoming photon beam. The different signal strengths can therefore be used as a contrast mechanism for microscopy, and the signal may vary by as much as 20–30% depending on the magnetic orientation. The signal obtained from such transmission experiments represents of course only an average over the sample thickness.

3.2.2 X-ray microscopy methods

Soft x-ray imaging techniques are based on the element and chemical state sensitive XMCD effect. There are three main variants of this x-ray based imaging technique. Photo-emission electron microscopes detect excited photoelectrons and can achieve a lateral resolution of around 50–100 nm [12, 13]. The other two variants are transmission x-ray microscopes in parallel or wide field mode [14], or in scanning mode [61]. The lateral resolution is hereby determined by the zone plate and is typically around 20–40 nm, though resolutions down to 15 nm were already reported [62]. Only spin-polarized scanning tunneling microscopy (SP-STM) can reach higher lateral resolutions down to the atomic scale [10, 31].

The results presented in this work, were acquired by means of the scanning transmission x-ray microscope at the Advanced Light Source, located at beamline 11.0.2 [63]. A schematic overview of the main beamline components, at beamline 11.0.2, is shown in Figure 3.3, and the important parts are described in the following sections.

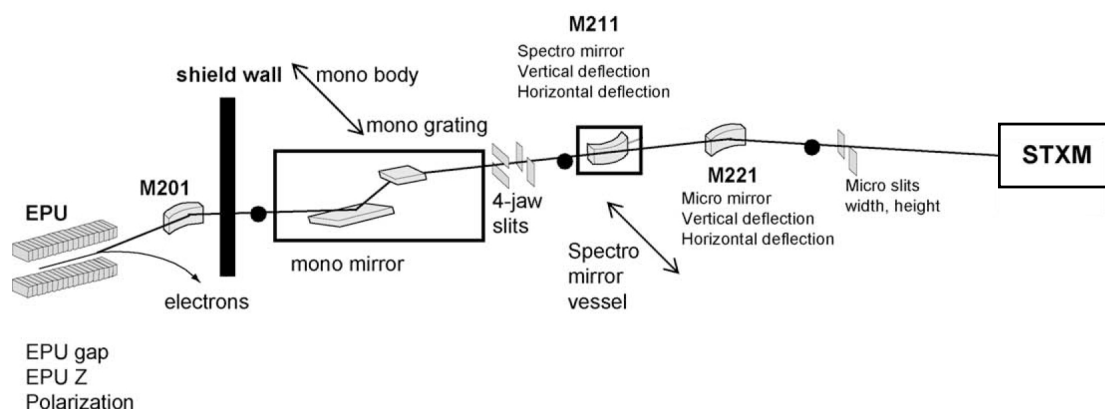


Figure 3.3: Schematic layout of the Molecular Environmental Science (MES) beamline (11.0.2) at the Advanced Light Source (taken from [64]).

3.3 SYNCHROTRON RADIATION

Synchrotron radiation is created by relativistic electrons (or positrons) that circle in a storage ring when they are accelerated in a magnetic field. The emission of synchrotron radiation dissipates energy from the electrons in the storage ring. In order to compensate this energy loss, the electrons are accelerated after each cycle in a microwave cavity. This process is most efficient if the electrons are not distributed evenly along the orbit, but are grouped into packets (or also called electron bunches), the distance of which is determined by the microwave

frequency. In the stationary frame of an observer such bunches have a typical length $\ell \simeq 10$ mm, corresponding to a pulse length of about $\tau = \ell/c \simeq 30$ ps, a lateral cross section of about $100 \mu\text{m}$, and one bunch contains in the order of 10^{10} electrons. The charged particles are kept on the desired horizontal orbit by vertical magnetic fields produced at locations around the ring by dipole electromagnets. Other magnets like quadrupoles and sextupoles help keep the bunches focused to a well defined cross section.

There are commonly three types of magnetic structures used to produce synchrotron radiation: bending magnets, undulators, and wigglers. A detailed description can be found in the work from D. Attwood [55]. Characteristic parameters for the synchrotron storage ring at the Advanced Light Source (ALS), Lawrence Berkeley National Laboratory (LBNL), is given in Appendix A.

3.3.1 Undulator radiation

Undulators are periodic magnetic structures with relatively weak magnetic fields. The periodicity causes the electron to experience a harmonic oscillation as it moves in the axial direction, resulting in a motion characterized by small angular excursions called undulations. The weak magnetic fields cause the amplitude of this undulation to be small, resulting in a narrow radiation cone of half angle $\theta \simeq 1/2\gamma$ (Figure 3.4). The resultant radiation is greatly reduced in

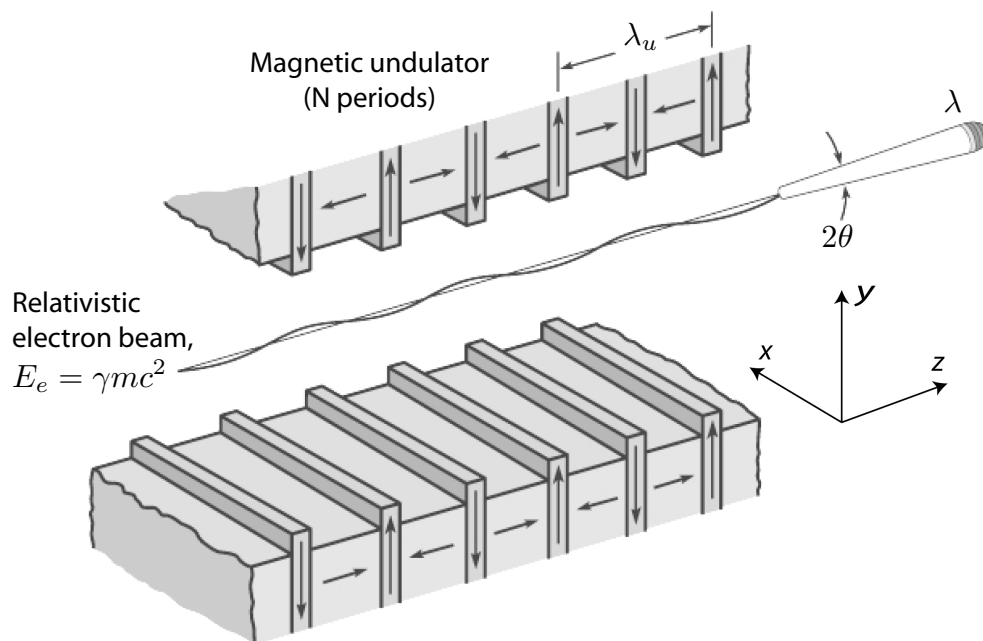


Figure 3.4: Illustration of narrow cone undulator radiation that is generated by electrons traversing a periodic magnet structure (taken from [55]).

wavelength λ from that of the magnet period λ_u , and is given by the undulator equation [55]:

$$\lambda = \frac{\lambda_u}{2\gamma^2} \left(1 + \frac{K^2}{2} + \gamma^2\theta^2 \right) \quad (3.5)$$

with

$$\gamma \equiv \frac{1}{\sqrt{1 + \frac{v^2}{c^2}}}, \quad (3.6)$$

and the magnetic deflection parameter K is defined by:

$$K \equiv \frac{eB_0\lambda_u}{2\pi mc}. \quad (3.7)$$

v is the relative velocity, c the velocity of light in vacuum, e the charge of the moving electron, m the mass of the moving particle, and B_0 the magnetic field amplitude. The case of small angular excursions ($K < 1$) is referred to as the undulator limit.

For the generation of variably polarized radiation, two pairs of arrays of permanent magnets are put together [65, 66, 67]. In Figure 3.5 the arrows show the orientation of the magnetization of each magnet block; g is the gap width between the upper pair of magnetic arrays and the lower pair of the magnetic arrays; λ_u is the magnetic period length which corresponds to four magnet blocks; h and w are the height and the width of each magnet block, respectively,

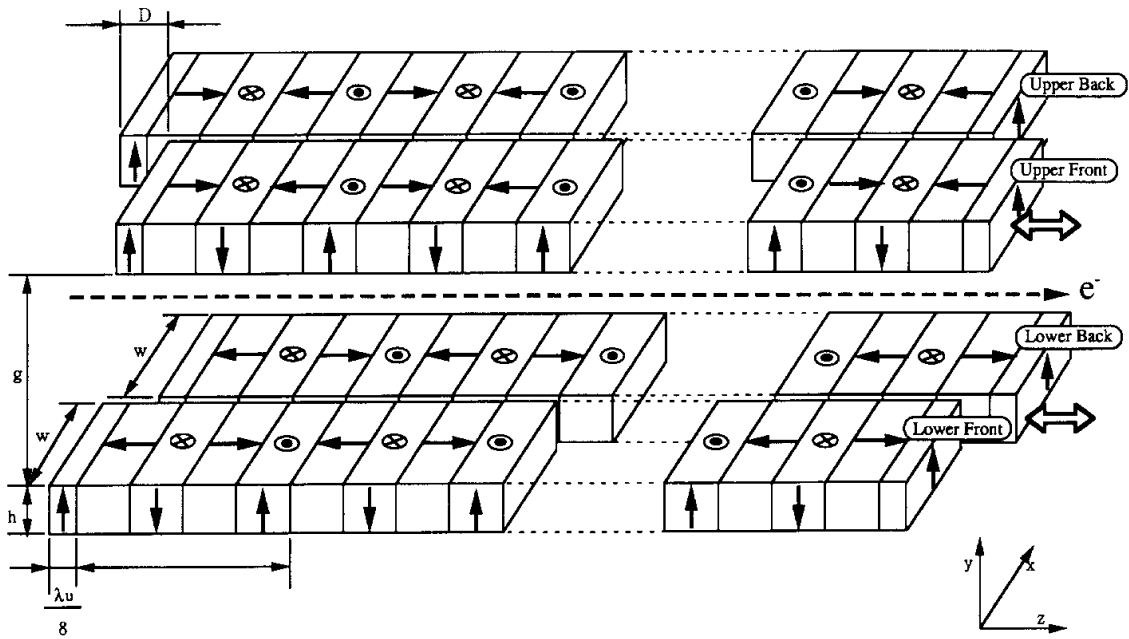


Figure 3.5: Schematic view of the magnetic structure for generating variably polarized undulator radiation (taken from [66]).

and D is the position shift distance (phasing distance) between the right and the left magnetic arrays in each pair. Two types of magnet blocks are required. One is the magnet block whose magnetization is parallel to the undulator axis (z -axis). The other is the block whose magnetization is along the y -axis. Two of the rows must be phase adjustable and these two rows (say the upper front and lower back) are moved together with respect to the fixed rows in order to change the polarization state.

The measurements in this work were performed at an elliptically polarizing undulator (EPU), as described above, with a period length of 5 cm and 37 periods. It can be used in four polarization modes: circular, elliptical, horizontal, and vertical. These modes can be chosen by appropriate phasing of the magnet rows. The minimum and maximum photon energies for each mode are given in Table 3.1.

	circular	elliptical	horizontal	vertical
min. energy [eV]	123	91	83	157
max. energy [eV]	660	2433	2600	2590

Table 3.1: Photon energy ranges for the EPU polarization modes at the Advanced Light Source (ALS), operated by the Lawrence Berkeley National Laboratory in California (USA).

The transversal oscillations in the motion of the electron also introduce higher order harmonics, used to extend the photon energy range of a given undulator. The observed wavelengths are then governed by an extension of the undulator equation (3.5):

$$\lambda_k = \frac{\lambda_u}{2\gamma^2 k} \left(1 + \frac{K^2}{2} + \gamma^2 \theta^2 \right) \quad (3.8)$$

with k the harmonic number. Even harmonics radiate a pattern that peaks off axis and has zero intensity on axis, resulting in less interesting coherence and brightness properties. Thus even harmonics are usually discarded. On the other hand, the odd harmonics radiate on axis with a narrow spectrum and into a narrow cone forward. Hence, they are quite interesting as source of high brightness and partially coherent x-rays. The spectral flux and brightness is illustrated in Figure 3.6 for circular and elliptical polarization modes from the elliptically polarizing undulator (EPU) at the Advanced Light Source.

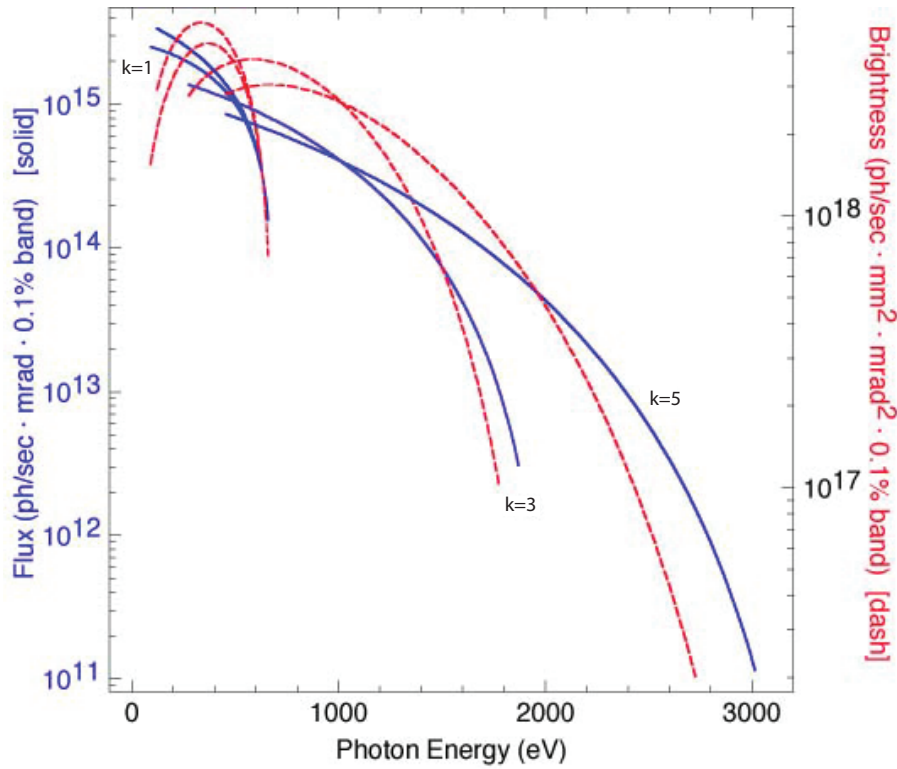


Figure 3.6: Spectral photon flux and brightness from the elliptically polarizing undulator at the Advanced Light Source in circular and elliptical mode. The circular mode only generates the first harmonic and this is depicted by the upper pair of curves for $k = 1$. The elliptical mode is shown for $k = 1, 3$ and 5 .

3.3.2 Monochromator

A monochromator operates on the general principle shown in Figure 3.7 [68]. Approximately collimated light from the source is incident directly on the grating and is diffracted by the grating. The beam is then focused by a mirror onto an exit slit. The wavelength is scanned by rotating the grating about an axis through its pole. The mirror remains fixed during the scanning as do the ingoing and outgoing directions at the grating. For different angles of the grating, different wavelengths are diffracted in the correct direction. Using the notation from Figure 3.7, the grating equation can be stated as:

$$Nk\lambda = \sin \alpha + \sin \beta, \quad (3.9)$$

where k is the order.

The monochromator used at the Advanced Light Source (beamline 11.0.2) is a very compact, entrance-slitless, plane-grating design with variable line-spacing. The mechanically ruled grating operates in the converging light from a spherical mirror working at high demagnification. Aberrations of the mirror are corrected

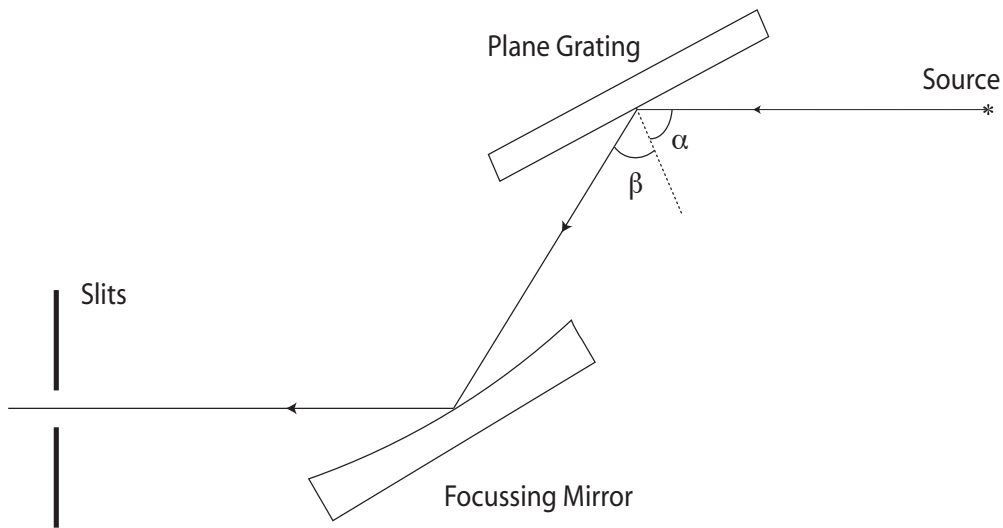


Figure 3.7: Principle monochromator.

by the line spacing variation, so that the spectral resolving power $\lambda/\Delta\lambda$ is limited by the ALS source size to about 7000. The wavelength is scanned by simple rotation of the grating with the fixed exit slit.

3.3.3 Time structure of synchrotron radiation

As mentioned in Section 3.3, the electron beam in a storage ring is not a continuous stream, but rather a highly modulated density function consisting of bunches with an axial charge distribution. The spacing of these bunches is set by the radio frequency (rf) used to restore the power of the electrons, once every turn around the storage ring, to compensate for the power lost to synchrotron radiation. The rf is fed to a microwave cavity operating in a mode with an axial electric field, synchronized so that slower electrons receive a small acceleration, while faster electrons experience a small deceleration. In this manner a sequence of potential wells is set up that tends to trap available electrons into a series of buckets that travel around the ring at velocities close to the speed of light, with a bunch-to-bunch separation equal to the rf wavelength. Depending on the operation mode of the storage ring, the light pulse width ranges in general between $\Gamma_{FWHM} = 1 - 100$ ps, at repetition frequencies from $f = 1 - 500$ MHz.

Figure 3.8 illustrates the electron bunch structure in the ALS storage ring for a multi bunch operation in which a pre-selected fraction of the buckets is filled. A less common, but regularly used mode of operation employs only two filled bunches. For the current case, a 500 MHz rf (499.644 MHz more specifically) pro-

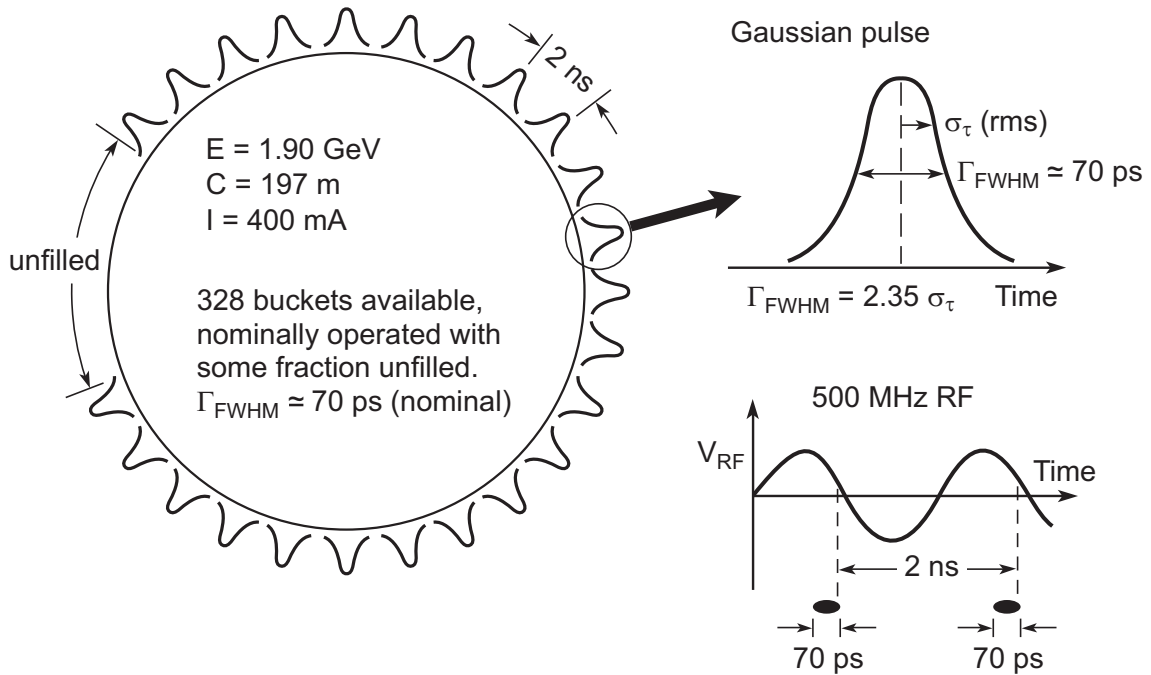


Figure 3.8: Illustration of the electron bunch structure in the ALS storage ring for multi bunch operation (taken from [55]). The radio frequency (rf) and storage ring circumference are matched for a 60 cm peak-to-peak structure of 328 axial buckets, of which a pre-selected fraction are filled with electrons. At the speed of light, 60 cm corresponds to a 2 ns x-ray pulse separation. The individual pulse duration, set by the rf voltage and beam dynamics, is 70 ps FWHM, which corresponds to a Gaussian axial bunch length ($2\sigma_z$) of 17.8 mm rms.

duces a bunch-to-bunch separation of 60 cm. A storage ring circumference of 197 m is set by the beam energy and the bending magnet fields, which accommodates 328 buckets. For the measurements in multi bunch mode, 276 of the 328 buckets are filled. Each of the electron bunches has a Gaussian pulse shape with a nominal 70 ps FWHM (full width at half maximum) duration, corresponding to an axial charge distribution of $\sigma_z = 9$ mm rms (root-mean-square). The pulse-to-pulse separation seen at any given position along the ring is 2 ns, corresponding to the 60 cm electron bunch separation traveling around the ring at nearly the velocity of light.

3.4 SCANNING TRANSMISSION X-RAY MICROSCOPY

The scanning transmission x-ray microscope at the Advanced Light Source, located at beamline 11.0.2 (Figure 3.3), uses thus photons from an elliptically polarizing undulator with a 5 cm period [69]. The ALS is operated at an energy of 1.9 GeV and provides photons in the energy range from 75 eV to 2150 eV. The x-rays from the undulator are focused vertically by a sagittal cylinder mirror onto the pre-mirror of a SX700 style plane-grating monochromator [69, 70, 71].

There is no entrance slit in front of the monochromator and the monochromator is equipped with two gratings (with 150 and 1200 lines/mm). The light from the monochromator is then focused by a toroidal focus mirror that generates a stigmatic focus at the exit slits of the STXM. These exit slits are illumination sources for the zone plate of the STXM.

The x-rays are subsequently admitted in the STXM chamber through a silicon nitride window (Figure 3.9). The photon beam is focused onto the sample by a zone plate with a working distance of 0.5–9 mm, depending on the photon energy. An order-selecting aperture (OSA) is placed between the zone plate and the sample, letting only the first order radiation through (see below). The sample is scanned relative to the focused x-ray beam, and the transmitted intensity is recorded as a function of the sample position using a photomultiplier tube or a photodiode. Several different zone plates are used depending on the photon energy, the required spatial resolution and the minimum working distance. The maximum energy resolution $E/\Delta E$ is better than 7500, and a resolution better than 3000 is achieved at a photon flux of $10^8 - 10^9 \text{ s}^{-1}$ in the sub-50 nm focused beam at energies of about 200–1600 eV. The maximum raster scan range is $20 \text{ mm} \times 4 \text{ mm}$, while the minimum step size is 2.5 nm. Images with up to 3000×2000 pixels can be acquired at any spatial size range within these limits. The very wide dynamic

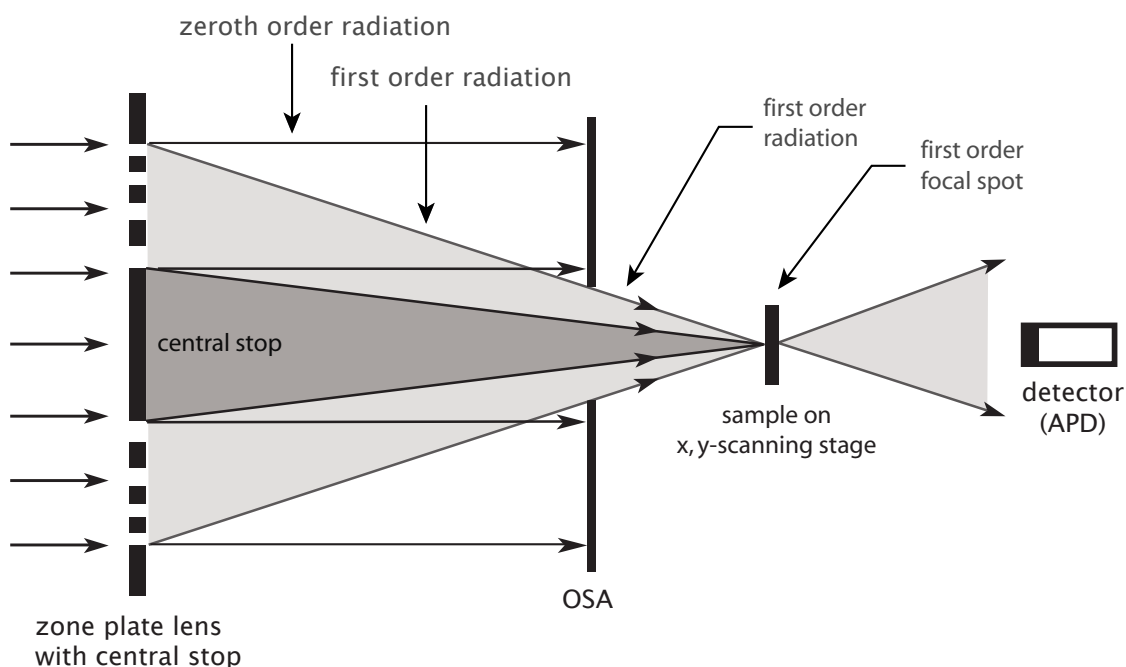


Figure 3.9: Principle drawing of a scanning transmission x-ray microscope with a central zone plate stop and an order sorting aperture (OSA) blocking all but the first order radiation from reaching the sample (higher order radiation is not shown).

range of the spatial scanning system has a continuous interferometric feedback of the positioning with an accuracy of 5 nm. Typical dwell times per pixel are 0.1–100 ms.

3.4.1 Zone plate

Light is usually focused with lenses using a refraction process, but in the EUV and the soft x-ray range, the refraction is practically non existing and the light is strongly absorbed. Therefore other focusing tools have to be used. In particular, Fresnel zone plates are very efficient using the diffraction of the photons with a periodic circular structure of opaque and transparent multilayer structures.

Sequential zones of radius r_n are specified such that the incremental path length to the focal point is $n\lambda/2$, with λ the wavelength of the incident photons. Considering the first order diffraction from a circular grating and using the notation of Figure 3.10, an expression is given for the zonal radii:

$$f^2 + r_n^2 = \left(f + \frac{n\lambda}{2}\right)^2, \quad (3.10)$$

which upon expansion and consolidation of like terms becomes

$$r_n^2 = n\lambda f + \frac{n^2\lambda^2}{4}. \quad (3.11)$$

The term $n^2\lambda^2/4$ represents the spherical aberration and can be ignored for $f \gg n\lambda/2$. This is often the case at x-ray wavelengths and so Eq. (3.11) simplifies to

$$r_n \simeq \sqrt{n\lambda f}, \quad (3.12)$$

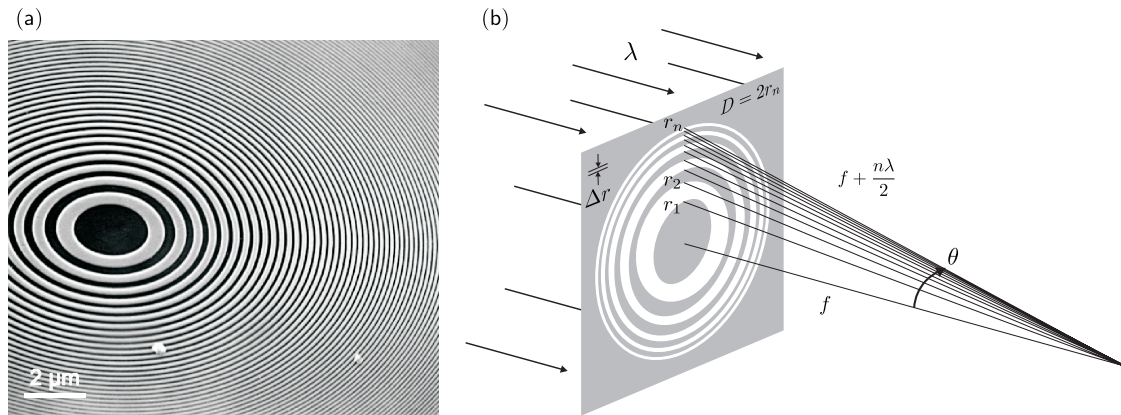


Figure 3.10: (a) Illustration of the inner part of a zone plate taken with a scanning electron microscope. (b) A Fresnel zone plate lens with plane wave illumination, showing only the convergent (+1st) order of diffraction [55].

which shows that a real first order focus is achieved when successive zones increase in radius by \sqrt{n} .

From Eq. (3.12), for a total number N of zones and the outer zone width Δr defined by:

$$\Delta r \equiv r_N - r_{N-1}, \quad (3.13)$$

the lens diameter D can be written as:

$$D \simeq 4N\Delta r, \quad (3.14)$$

and the focal length f is obtained as:

$$f \simeq \frac{D\Delta r}{\lambda}. \quad (3.15)$$

The wavelength dependence of the focal length illustrates the highly chromatic behaviour of zone plate lenses. In case no monochromator would be available, the zone plate could be deployed together with a pinhole as a linear monochromator.

Only the first order diffraction was considered till now, but a transmissive grating generates many diffraction orders m and the various orders are expected to come to focus on axis at focal distances:

$$f_m = \frac{r_1^2}{m\lambda}, \quad (3.16)$$

for diffractive orders $m = 0, \pm 1, \pm 2, \dots$. The diffraction efficiency η_m for a Fresnel zone plate of alternately opaque and transmissive zones, is then defined by the transmitted radiation of the m^{th} diffraction order with respect to the incident radiation, and is given by:

$$\eta_m = \begin{cases} \frac{1}{4} & m = 0 \\ \frac{1}{m^2\pi^2} & m \text{ odd} \\ 0 & m \text{ even} \end{cases} \quad (3.17)$$

where half the incident radiation is absorbed by the opaque zones. At a STXM only the first order radiation is let through by means of an OSA.

The corresponding spatial resolution can be derived using the Rayleigh resolution criterion and results in:

$$R = \frac{0.610\lambda}{NA} = 1.22 \frac{\Delta r}{m}, \quad (3.18)$$

with $NA \equiv \sin \theta$ the numerical aperture (see notation in Figure 3.10).

The parameters of the (Au) zone plates used for the measurements discussed in this work, are listed in Table 3.2. Measurements were performed at the L_3 absorption edges of Ni (852.7 eV) and Co (778.1 eV), corresponding to wavelengths of 1.454 nm, 1.5934 nm respectively, using the relationship:

$$\hbar\omega.\lambda = hc = 1239.842 \text{ eV nm}, \quad (3.19)$$

with $\hbar\omega$ the photon energy and c the velocity of light in vacuum.

	35 nm ⁽ⁱ⁾	35 nm ⁽ⁱⁱ⁾	25 nm
diameter D [μm]	155	240	120
central stop diameter [μm]	65	85	50
Au thickness [nm]	120	150	170
smallest zone thickness Δr [nm]	35	35	25
total number of zones N	1107	1714	1200
resolution R (first order) [nm]	42.7	42.7	30.5
focal length f (first order) [mm]			
L_3 Ni-edge @ 1.454 nm	3.731	5.777	2.063
L_3 Co-edge @ 1.593 nm	3.405	5.272	1.883

Table 3.2: Parameters of the zone plates used for the STXM measurements at the Advanced Light Source (ALS). (i) refers to measurements performed before June 2006, and (ii) for measurements after June 2006.

3.4.2 Detection system

Fast avalanche photodiode

During multi bunch operation mode at the Advanced Light Source, the photon flashes arrive with a spacing of 2 ns. In order to resolve this time structure, a fast enough detection system is necessary to perform time-resolved experiments. Therefore, a fast silicon avalanche photodiode (APD) is used for the detection of the transmitted photons, followed by high bandwidth electronics. An APD is a doped diode and when a reverse bias is applied, a region of high electric field ($\gtrsim 10^5$ V/cm) is created. X-rays are photoelectrically absorbed, forming charge carriers undergoing gain due to impact ionization, when they enter the high field region. The general specifications for the Si APD (Hamamatsu model S2382 [72]), used during the experiments, are given in Table 3.3.

For the measurements presented in this work the optical window of the Si APD was removed and the diode was placed in an isolated case. The x-rays enter

General characteristics

window material	borosilicate glass
active area size	\varnothing 0.5 mm
effective active area	0.19 mm ²

Electrical and optical characteristics ($T = 25^\circ\text{C}$)

spectral response range λ	400 nm – 1000 nm
peak sensitivity wavelength λ_p	800 nm
gain M ($\lambda = 800$ nm)	100
photon sensitivity S ($M = 1$, $\lambda = 800$ nm)	0.5 A/W
quantum efficiency QE ($M = 1$, $\lambda = 800$ nm)	75 %
dark current I_D (Typ./Max.)	0.1 nA / 1 nA
breakdown voltage V_{BR} (Typ./Max.), $I_D = 100$ μA	150 V / 200 V
temperature coefficient of V_{BR}	0.65 V/ $^\circ\text{C}$
cut-off frequency f_c ($R = 50$ Ω)	900 MHz
terminal capacitance C_t	3 pF
excess noise figure x ($\lambda = 800$ nm)	0.3

Table 3.3: General characteristics of Hamamatsu Si APD S2382 [72].

through a small pinhole and a good alignment is needed between the zoneplate, the OSA and the detector. A 50 nm thin Al foil can also be placed in front of the pinhole reducing the stray light of the laser interferometer.

Amplifier chain for the detector signals

The low level of the original APD signals does not provide a measurable count-rate. Therefore a well suited high bandwidth amplifier chain has to be set up (cf. Figure 3.11). The DC component of the signal is monitored by a bias tee [73] while the pulses, originating from the x-ray flashes, are transferred capacitively. A series of broadband amplifiers (with a bandwidth of 1.5 GHz and 7 GHz [74]) and impedance matching attenuators are used to amplify the signal, and the pulses are differentiated with a capacitor C_2 (= 6.8 pF). The output signal is afterwards transferred to a routing electronics where the counts, originating from the transmitted photons, are routed synchronously to individual counters. A data acquisition card is used to transfer the counts, corresponding to the particular time delays, to a computer controller where all images are stored (cf. Paragraph 3.5.3).

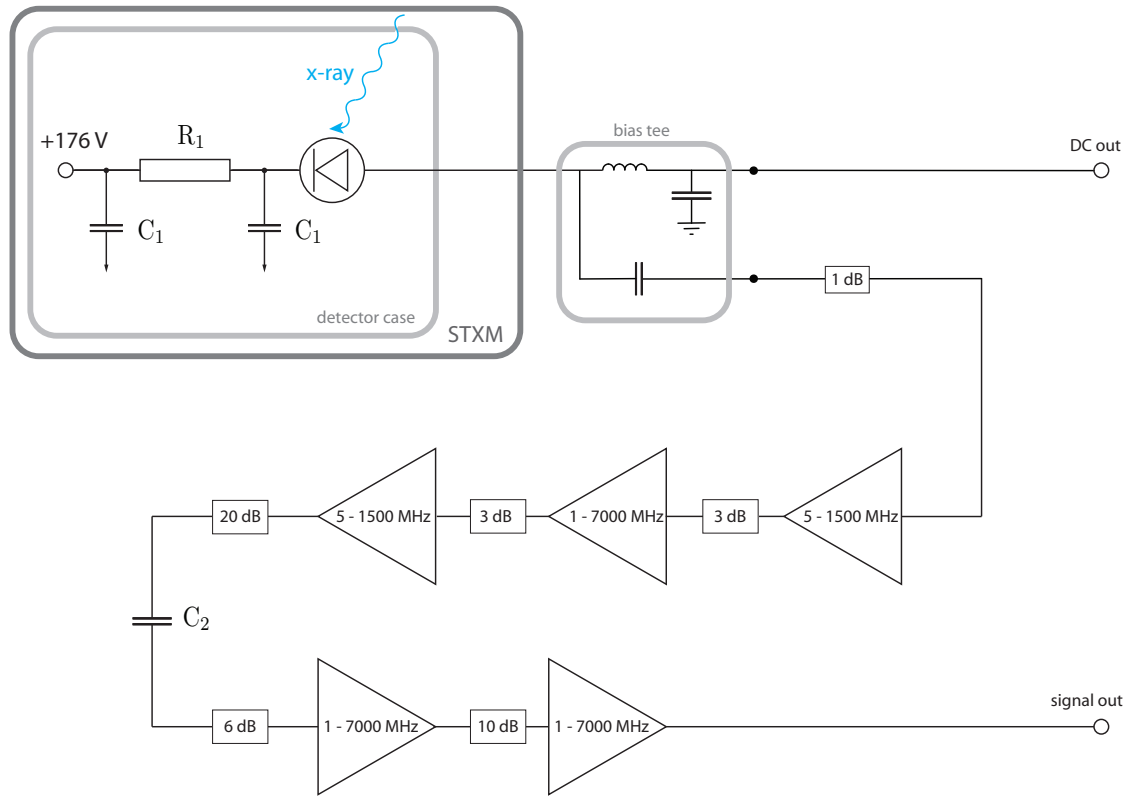


Figure 3.11: Block diagram of the amplifier chain for the amplification of the APD signals. Low noise amplifiers were used with a bandwidth of 1.5 GHz and 7 GHz [74]. The values of the indicated resistor and capacitors are: $R_1 = 1 \text{ M}\Omega$, $C_1 = 4.7 \text{ }\mu\text{F}$, and $C_2 = 6.8 \text{ pF}$.

3.5 TIME-RESOLVED SCANNING TRANSMISSION X-RAY MICROSCOPY

Time-resolved magnetic imaging experiments follow a stroboscopic acquisition scheme (Figure 3.12). The magnetic state of the sample is excited periodically by applying magnetic field pulses or an alternating field. The external field is applied synchronized with the image acquisition, i.e. with the probing photon flashes. The adopted procedure only allows to observe continuously repeating events in the magnetization distribution $\mathbf{M}(\mathbf{r}, t)$, i.e. those processes which occur during each cycle at the same location of the sample. Fluctuations and statistical events will thus be averaged out. Since synchrotron radiation is generated only at the moment when an electron bunch passes through an undulator or a bending magnet, the bunch structure results in a natural time structure of the synchrotron radiation, as described in Paragraph 3.3.3. At the Advanced Light Source, photon flashes, with a pulse width of about 70–100 ps, arrive every 328 ns in two bunch mode and every 2 ns in multi bunch mode. Several images can be recorded simultaneously at different time steps with respect to the excitation field, using an ap-

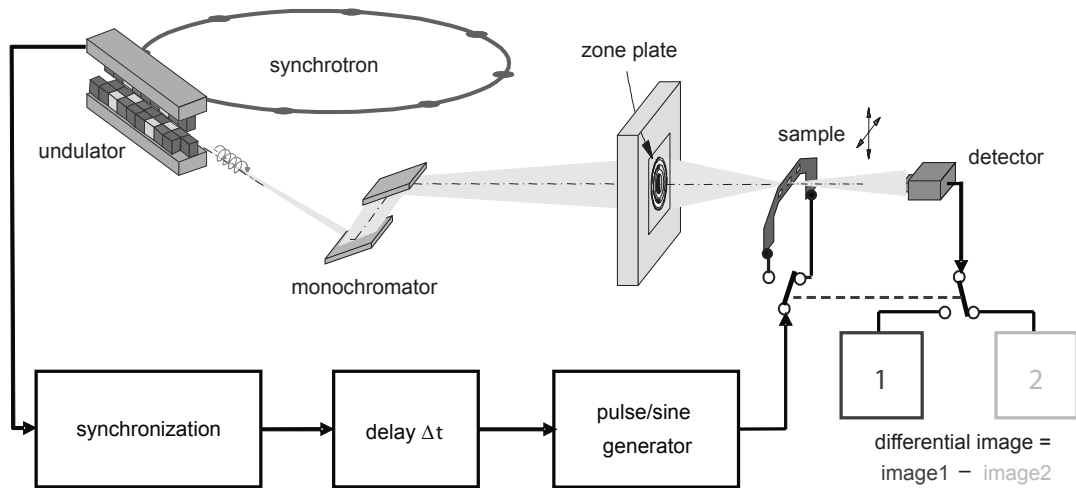


Figure 3.12: Time-resolved scanning transmission x-ray microscopy (TR-STXM). The imaging is performed in a stroboscopic way by delaying the excitation signal relative to the x-ray flashes. A differential technique is used for an improved signal-to-noise-ratio.

appropriate routing device (cf. Paragraph 3.5.3). Such acquisition method provides an adequate way to study the magnetization dynamics by means of differential images (cf. Section 5.1).

3.5.1 Sample and stripline configuration for in-plane field excitation

The magnetic microstructures were patterned by e-beam lithography onto a $10\ \mu\text{m}$ wide and $150\ \text{nm}$ thick Cu stripline. The samples and the stripline structure were evaporated on a $100\ \text{nm}$ thin Si_3N_4 membrane exhibiting a transmission of ca. 80% for photon energies around $800\ \text{eV}$. The complete structure was capped with a $2\ \text{nm}$ Al protective coating against corrosion [21].

Two different types of striplines were employed to produce an in-plane magnetic field, and are sketched in Figure 3.13. A current sent through a horizontally oriented straight stripline induces a field in the vertical direction. On the other hand, the samples are located at the two lower straight sections in a hairneedle-shaped stripline where the current flows vertically, inducing a field in the horizontal direction. Both types of striplines lead to distinct differences in the experimental results and the analysis of the data (cf. Section 5.4). Details of the calculations for the applied field amplitude can be found in Appendix B, together with a conversion table from the measured electrical power to the corresponding magnetic field strengths.

Two different sample materials were used in the current work, namely soft mag-

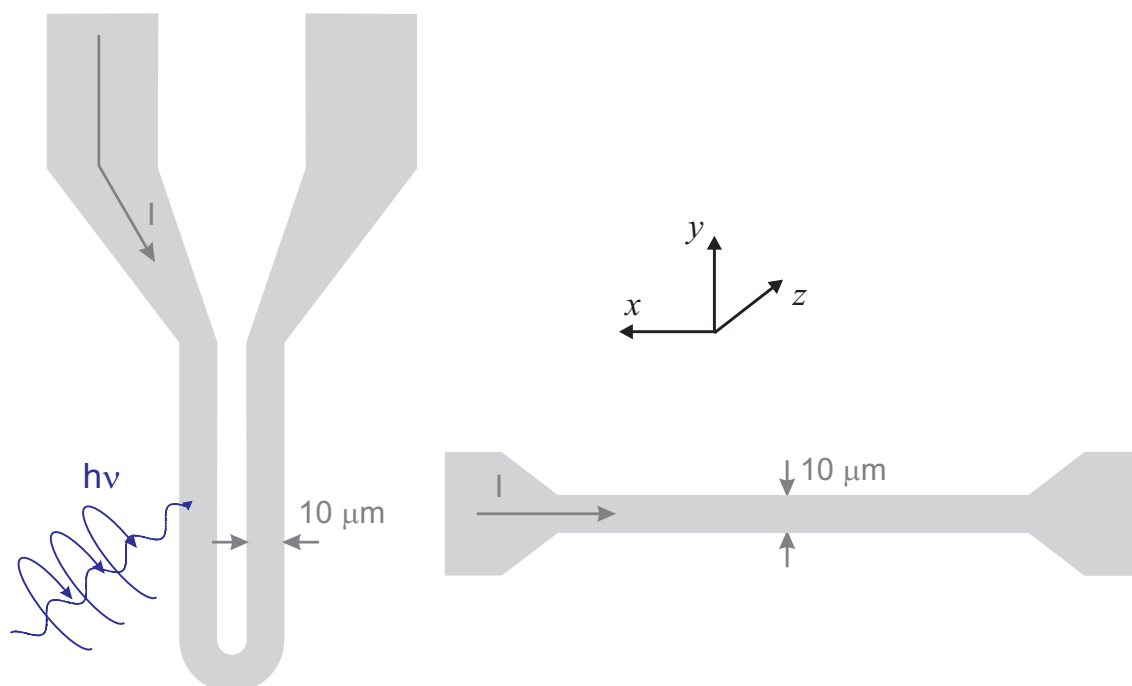


Figure 3.13: Two different types of striplines are sketched for the generation of an in-plane magnetic field. A hairneedle-shaped stripline is shown on the left-hand side. Structures are evaporated on the two straight, vertical sections. On the right-hand side, a straight stripline is sketched with the current flowing in the horizontal direction.

netic Permalloy ($\text{Ni}_{80}\text{Fe}_{20}$) and cobalt (Co). As described in Paragraph 3.2.1, the element specific x-ray magnetic circular dichroism (XMCD) was used as contrast mechanism for the imaging of the magnetic structures. The images were recorded at the L_3 absorption edges of Ni (852.7 eV) and Co (778.1 eV). In order to observe the in-plane magnetization in a magnetic structure, the sample has to be placed under a certain angle Θ with respect to the plane normal to the photon direction (Figure 3.14), as the XMCD is only sensitive to the projection of the magnetization on the photon propagation direction (cf. Paragraph 3.2.1). On the other hand, to measure the out-of-plane component of the magnetization, e.g. the vortex core in a magnetic vortex structure, it is necessary to place the sample perpendicular to the incoming photons to get the highest magnetic contrast. The imaging under both sample geometries will be extensively illustrated in Chapter 4 & 5.

3.5.2 Excitation types

Pulsed excitation

Ferromagnetic structures can be excited using fast current pulses provided by electronic pulse generators. The amplitude and especially the rise time of the pulses are important parameters for studying the magnetization dynamics. An

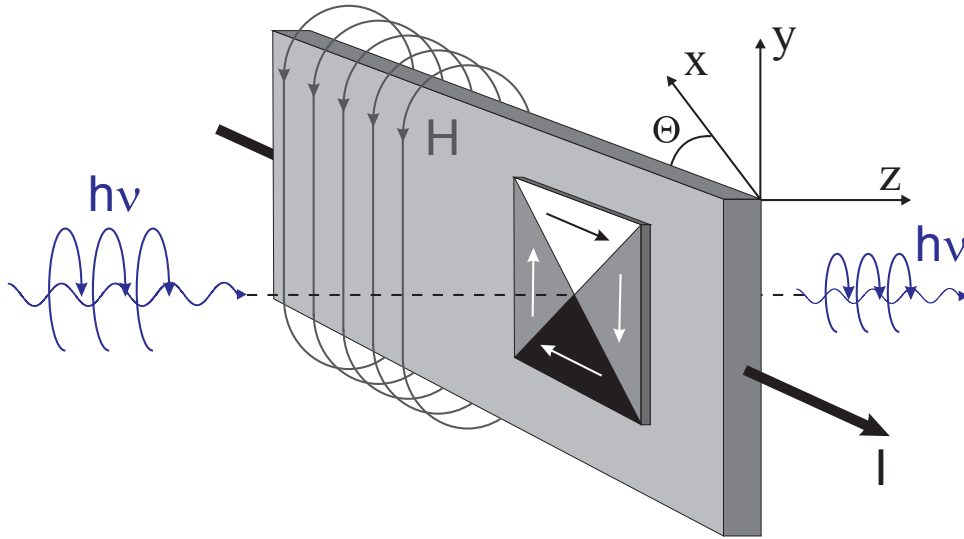


Figure 3.14: Illustration of the sample/stripline setup (for a straight stripline). The vortex structure is placed on a stripline. The arrows indicate the in-plane distribution of the magnetization forming a closed flux around the vortex core. The sample is placed under an angle Θ with respect to the plane normal to the photon propagation direction. A current I is sent through the stripline, generating a magnetic field H .

adequate repetition frequency of the pulse generator with respect to the time structure of the x-ray flashes is also needed. The characteristics of the employed Avtech pulse generators are given in Table 3.4 [75]. The pulse generators are triggered with ECL (emitter-coupled logic) pulses synchronized with the photon flashes of the synchrotron. The time jitter on the output pulses is only ± 15 ps. The pulsed excitation with the corresponding probing scheme is illustrated on the left-hand side of Figure 3.15. Fast magnetic field pulses are adequate to provide a broadband excitation of a ferromagnetic thin film structure. All the excited modes can then be probed by delaying the field pulses relative to the photon flashes.

Model	AVM-2-PS	AVM-3-PS	AVMR-2-PS
max. amplitude (50 Ω load)	15 V	15 V	20 V
pulse width	0.2–2.0 ns	0.2–2.0 ns	20–200 ns
repetition frequency	0–25 MHz	0–25 MHz	0–10 MHz or 0–5 MHz
rise time	≤ 100 ps	≤ 150 ps	300 ps
falling time	≤ 135 ps (typically 100 ps)	≤ 600 ps	300 ps

Table 3.4: Specifications of the Avtech pulse generators used for the STXM measurements at the Advanced Light Source (ALS) [75].

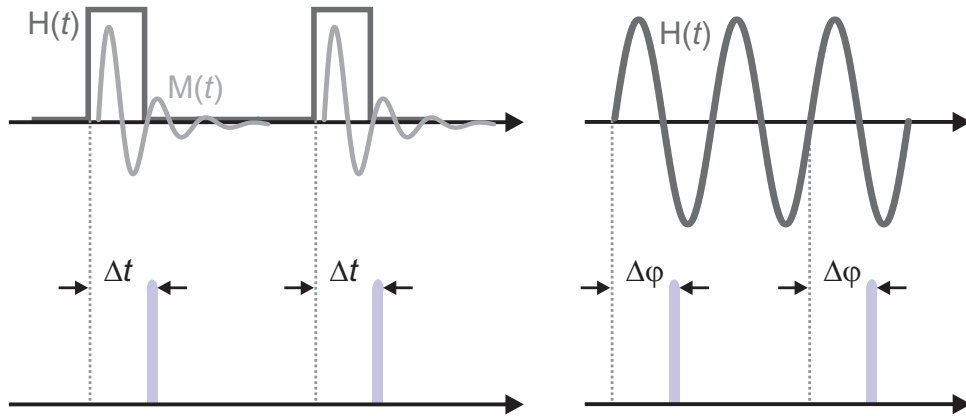


Figure 3.15: Illustration of the stroboscopic measuring technique with pulsed and sine excitation. The dynamic magnetic response of the vortex structure can be imaged by probing at specific time delays or phases with respect to the applied field, respectively.

Sine excitation

Instead of using pulsed excitation, magnetic layers can also be excited by an in-plane sinusoidal magnetic field $H_{sin} = H_0 \sin(2\pi ft)$ induced by applying an ac current I_{sin} through a stripline. The frequency f is chosen near the resonance frequency of the structure. The response of the sample is imaged in a stroboscopic way by delaying the excitation signal relative to the x-ray flashes, illustrated on the right-hand side of Figure 3.15. The alternating current is provided by a digital RF signal generator [76]. The generator can be synchronized by an external standard input signal at 1 or 10 MHz.

Burst excitation

The use of short pulses excites a broadband spectrum of modes in a ferromagnetic structure, while an alternating magnetic field, tuned at the correct eigenfrequency, excites specific modes of the system. By combining both excitation types, a ferromagnetic structure can be excited by one or several periods of an alternating magnetic field. Such burst excites the sample from its ground state. Additionally a small oscillating background field can be applied to the burst. Short bursts of an alternating magnetic field were realized using a double balanced frequency mixer [77]. The principle is shown in Figure 3.16. An alternating current from a digital RF signal generator (Aeroflex, type IFR 3416 [76]) is used as an AC coupled input. Pulses sent to the DC coupled input drive the mixer and open the port to the AC coupled output. An additional small DC offset to the pulse provides a small background to the output burst, as shown in Figure 3.16.

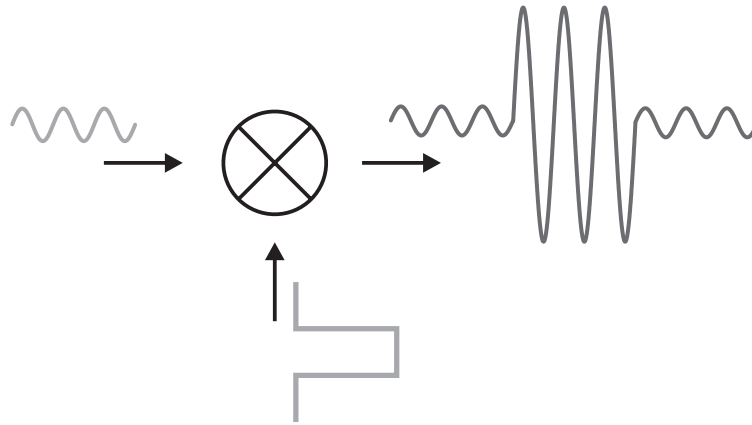


Figure 3.16: Illustration of the realization of a burst excitation with a frequency mixer, with an AC and DC coupled input, and an AC coupled output.

3.5.3 Experimental setup and data acquisition

Time-resolved imaging of the magnetization dynamics at a scanning transmission x-ray microscope follows a stroboscopic scheme with the excitation as pump and the x-ray flashes of the synchrotron as probe. The basic requirement is the synchronization between pump and probe. Several signals are provided from the storage ring collected in the ALS user timing system, serving as time reference for the photon flashes [78]. The excitation needs then to be synchronized with these reference markers. The detected photons are sent to a routing device together with all time markers. Using these markers as reference, the detected x-rays can then be routed to different counting channels, where each channel forms a separate image representing the response of the excited system at a certain time with respect to the excitation. The detailed experimental setup is outlined in the following paragraph for the different excitation types used in this work. Details of the routing device can be found in the work of Acremann et al. [79].

Pulsed excitation

The setup scheme for pulsed excitation is depicted in Figure 3.17. A differential ECL line provides signals with a frequency corresponding to the orbit clock ($RF/328 = 499.644\text{ MHz}/328 = 1.5233\text{ MHz}$) and are, together with the 499.644 MHz RF signal from the storage ring, directed to the routing device. Using these time markers, pulses are generated which are synchronized with the probing photon flashes. These pulses are reshaped to ECL level and can be used as a trigger for the fast pulser. The fast pulses are then sent to the sample while a small portion (-20 dB) is drawn off to the scope with a pickoff tee for reference

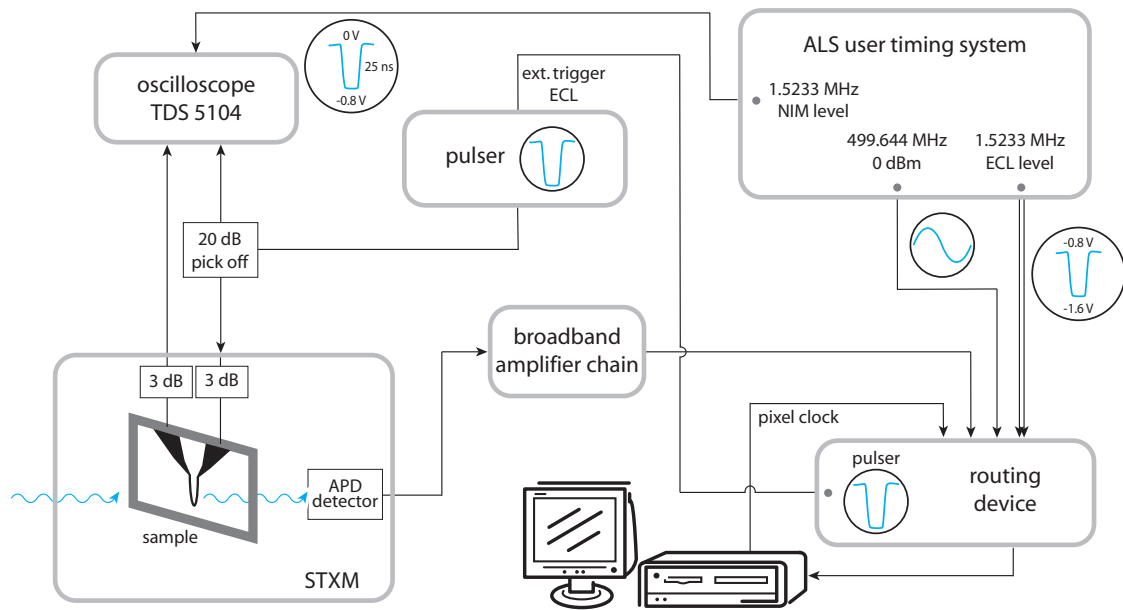


Figure 3.17: Experimental setup used for pulsed excitation at the Advanced Light Source.

purposes [80], so that an exact time relation is known between the excitation pulses and the counting channels. The outgoing pulses are also collected on the scope and a NIM (nuclear instrumentation module) signal from the user timing system is used as a trigger on the scope. 3 dB attenuators are added before and after the sample to provide a good matching so that no reflection pulses appear from the small impedance mismatch of the sample. The transmitted photons are detected by the APD detector and the amplified signals are sent to the routing device where all signals are routed in the correct counting channel using the fore mentioned reference markers and a pixel clock, indicating the duration of measurement for every pixel of an image. The transmitted intensity corresponding to a certain pixel of an image at a certain time delay with respect to the external field pulses, is then collected on a personal computer. Currently, fourteen counting channels were available so fourteen images could be recorded simultaneously with a minimum time step of 2 ns. Smaller time steps can be achieved by delaying the excitation field pulses. Hereby, consecutive measurements need to be performed for different delays. Such a measurement scheme is unfortunately prone to external factors like thermal drifts or mechanical vibrations, causing misalignments and distortions of the consecutively recorded images. Such distortions of the images are difficult to correct as the drifts and vibrations are occurring randomly. Nevertheless, an autocorrelation method can be applied to align the serie of images.

Sine excitation

The setup scheme for sine excitation is depicted in Figure 3.18. Again a differential ECL line is sent to the routing device. The RF signal from the storage ring is amplified and then divided using a 6 dB power splitter. One part is also directed to the routing device while the other part is reshaped with a frequency divider. The signal generator accepts only external standard inputs with a frequency of 1 MHz or 10 MHz and at a level of 300 mV rms to 1.8 V rms into 1 k Ω . Therefore the frequency of the RF signal is divided by 50 (= 9.9929 MHz) and a 10 MHz filter is used to reduce the noise on the signal. This signal is then used as an external input for the source generator, which produces an alternating signal synchronized with the x-ray flashes. Additional amplifiers can be added to enhance the power of the signal, which is then sent to the sample. Again a power splitter can be used to extract part of the signal as a reference. The phases mentioned in the following chapters are with respect to this reference marker. The exact phase of the field on the sample is thus not known. The detection scheme remains the same and images are eventually recorded at certain phases with respect to the alternating magnetic field.

In principle the ferromagnetic structure responds in accordance with the external alternating field. Due to the time structure of the synchrotron source, one needs to meticulously choose the frequency of the external field in order to perform a stroboscopic measurement. Assuming that the probing photon flashes in multi

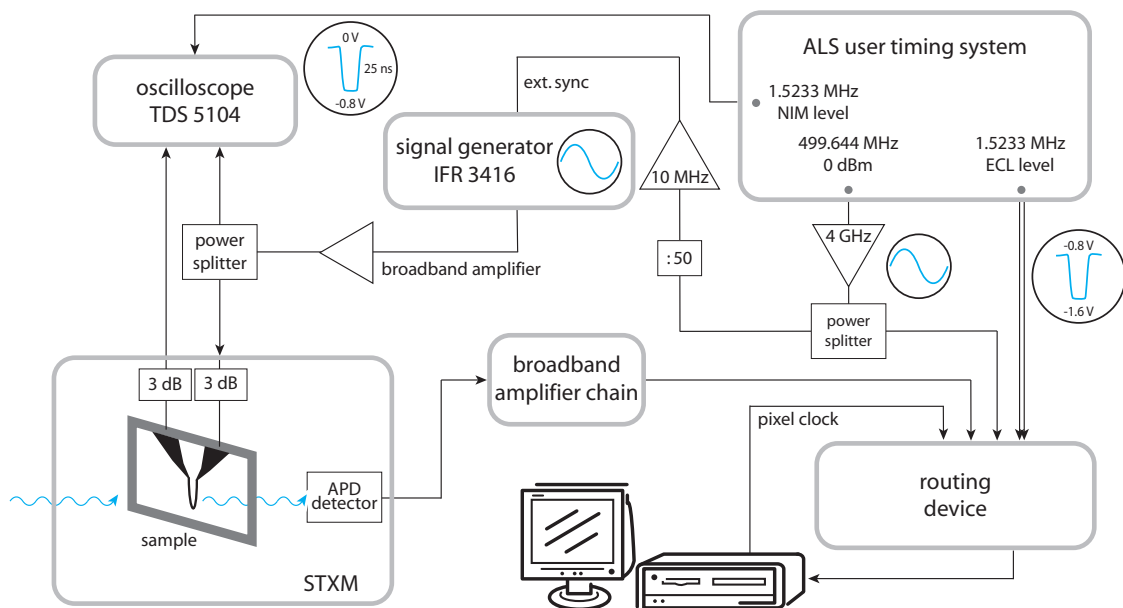


Figure 3.18: Experimental setup used for sine excitation at the Advanced Light Source.

bunch mode (500 MHz) are routed to n different counting channels, n different equidistant phases can be probed for an external field with a frequency of $f_{ini} = 500 \text{ MHz}/n$. This f_{ini} also corresponds to the frequency grid f_{Δ} by which the frequency of the external field f can be varied. The excitation frequency f should obey the following relation:

$$f = f_{ini} + 2n \times f_{\Delta}, \quad (3.20)$$

so n different phases with respect to the alternating magnetic field can be probed simultaneously. Thus one can add an even multiple of f_{Δ} to f_{ini} . The odd multiples of f_{Δ} will reduce the amount of different phases which can be probed as it corresponds to another frequency grid. If $n = 8$ for example, 8 different equidistant phases can be probed at $f_{ini} = 500 \text{ MHz}/8 = 62.5 \text{ MHz}$. An excitation frequency f of $f_{ini} + 2f_{\Delta} = 62.5 \text{ MHz} + 125 \text{ MHz} = 187.5 \text{ MHz}$, will still result in 8 different phases, but a frequency f of $f_{ini} + 1f_{\Delta} = 62.5 \text{ MHz} + 62.5 \text{ MHz} = 125 \text{ MHz}$ (corresponding to $f_{ini} = 500 \text{ MHz}/4$), will resume to a probing scheme with only 4 different phases. Such a probing scheme has the inherent advantage of recording images simultaneously.

Burst excitation

The setup scheme for burst excitation is depicted in Figure 3.19. The same reference markers are used for the routing device as in the previous two setups (a differential ECL line and the RF signal). Fast pulses are generated, synchronized

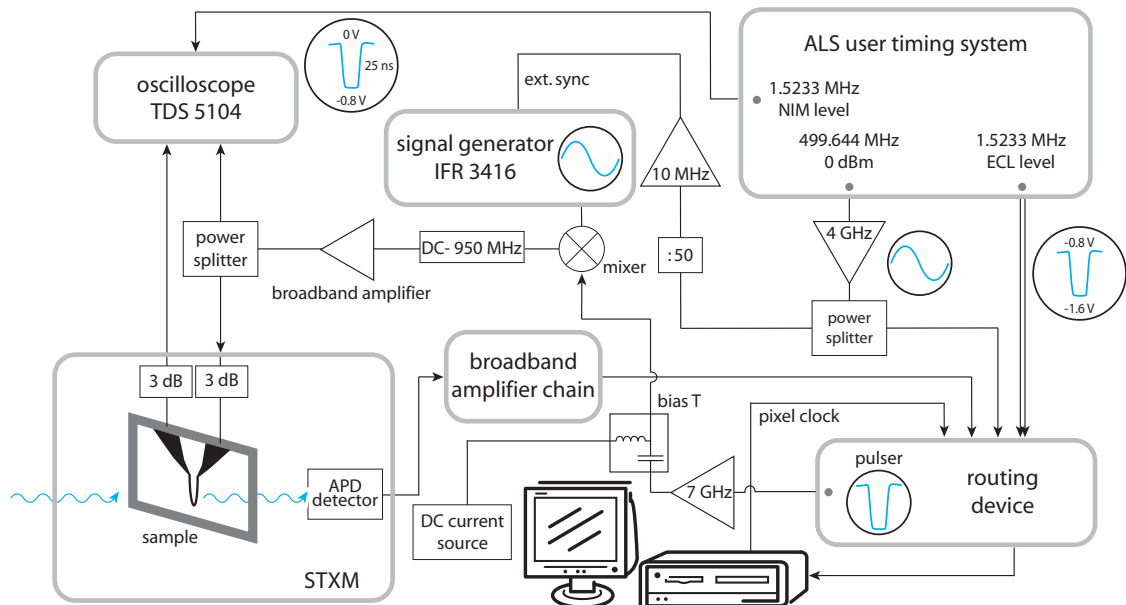


Figure 3.19: Experimental setup used for burst excitation at the Advanced Light Source.

to the photon flashes, and are amplified with a 7 GHz amplifier. A background current can be added to the pulses using a bias tee [81]. The amplified signal is then sent to a double balanced frequency mixer together with a sine wave created by the source generator [76]. The mixer generates bursts of the alternating current and the high frequency components are subsequently filtered out with a low pass filter [82], before it is amplified. The signal is then sent through the stripline so that bursts of the alternating field can be created. The length of the burst is varied by the pulse width of the pulses, while the amplitude of the background alternating field can be adjusted by the current source before the bias tee. The acquisition of the data remains fairly the same.

CHAPTER 4

CHARACTERIZATION OF FERROMAGNETIC VORTEX STRUCTURES

“Anomalies bug me.”

— DR. GREGORY HOUSE

Different methods are available to observe the magnetic microstructure, as noted in Section 1.3, and a large variety of techniques was examined in the work of Alex Hubert & Rudolf Schäfer [1]. In the previous chapter, the general characteristics of a scanning transmission x-ray microscope were outlined, together with its ability to study the magnetization distribution in thin film micron-sized patterns. Therefore the element specific XMCD effect is used as contrast mechanism. Magnetic vortex structures were introduced and extensively described in Chapter 2, while this chapter mainly focusses on the magnetic characterization of structures containing a single vortex, in remanence. Magnetic structures with a single vortex have an in-plane curling of the magnetization and an out-of-plane vortex core (cf. Paragraph 2.2.2). The spatial distribution of the magnetization $\mathbf{M}(\mathbf{r})$ of such vortex structures was imaged using the scanning transmission x-ray microscope (STXM) at the Advanced Light Source (ALS, BL 11.0.2). Beside the imaging of the magnetization distribution, the magnetic information that can be derived from it will be treated as well.

4.1 IN-PLANE MAGNETIZATION OF A VORTEX STRUCTURE

4.1.1 Setup considerations

In order to visualize the in-plane distribution of the magnetization in a vortex structure, the sample has to be placed under an oblique angle so there's a contribution of the magnetization along the direction of the x-rays (see also Paragraph 3.2.1). For the measurements performed in this work, the angle Θ between the

sample surface and the plane normal to the photon propagation direction is set to 30° (cf. Figure 3.14).

4.1.2 Magnetic contrast at one specific polarization

Images are shown for a series of soft magnetic Permalloy ($\text{Ni}_{80}\text{Fe}_{20}$) structures in the first two panels of Figure 4.1, recorded by using left and right circularly polarized light, respectively. The vortex patterns were imaged at the L_3 absorption edge of Ni (852.7 eV). The images in the left panel were made with negative polarization (left circularly polarized light), indicated with Γ^- ; while the middle panel illustrates images recorded with positive polarization (right circularly polarized light), indicated with Γ^+ . The transmitted intensity is depicted: a darker contrast reflects a lower transmission while a brighter contrast represents a higher transmission. All individual patterns show regions with bright and dark contrast, and in addition regions with gray contrast in between. Considering the XMCD effect, where the absorption of circularly polarized light depends on the magnetization direction of the structure, all images (except in the lowest row) show patterns with a single vortex where the magnetization circulates in-plane around the core. Images at both polarization of light show an opposite magnetic contrast. All ground states agree with the models developed by van den Berg [27, 28, 29], but as illustrated for the $1\ \mu\text{m} \times 2\ \mu\text{m}$, 40 nm thick Permalloy elements (structures in the lowest row), more complicated domain structures can occur. Different magnetic configurations are observed for the same sample geometry containing two

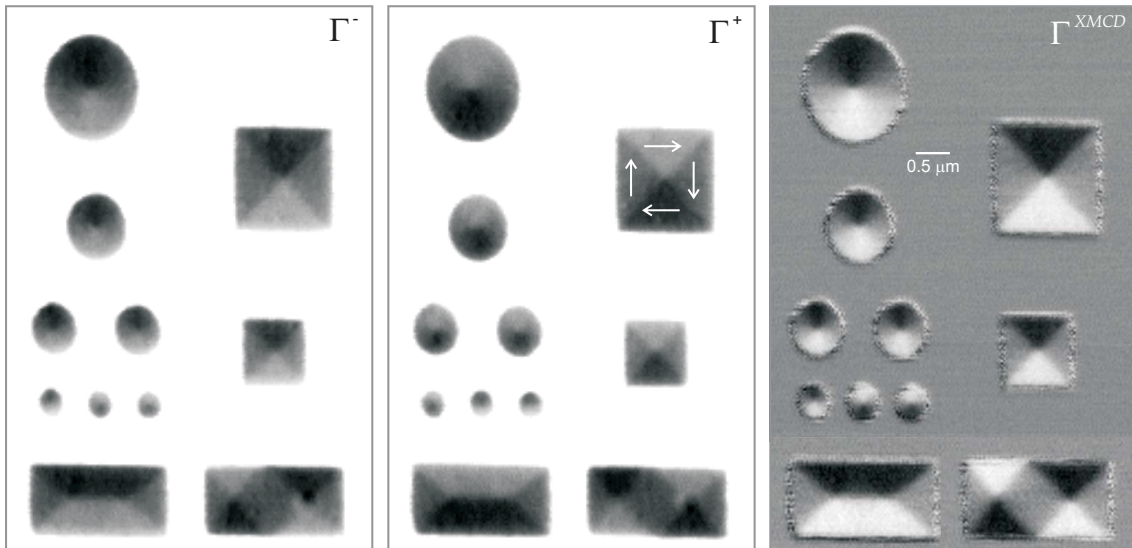


Figure 4.1: STXM images taken for zero external field at two different polarization, Γ^- and Γ^+ respectively, of the photons. The contrast shown in panel Γ^{XMCD} is deduced from Γ^- and Γ^+ according to equation (4.1).

vortices and one antivortex (cf. Figure 2.4 (c)) at minimum. The primary source of ambiguity seems to be caused by the interaction of domain wall clusters with the sample edge [83, 84, 85].

4.1.3 Magnetic contrast - dichroism

The image sequences recorded at opposite polarization can be exploited to extract “dichroic images” (right panel in Figure 4.1), using the following expression (pixel by pixel):

$$\Gamma^{XMCD} = \frac{\Gamma^- - \Gamma^+}{\Gamma^- + \Gamma^+}. \quad (4.1)$$

This method improves drastically the signal-to-noise-ratio, compared to the contrast in the separate images, and removes the non-magnetic contributions. The black contrast reflects an antiparallel alignment between the magnetization direction and the photon polarization, while a white contrast represents a parallel alignment (see below).

The magnetization direction can be derived from the magnetic contrast considering the absorption spectra at the specific absorption edges. The images in Figure 4.1 were recorded at the L_3 absorption edge of Ni (852.7 eV), which has similar absorption spectra as Fe at the corresponding edge for the magnetization aligned parallel and antiparallel to the photon polarization (Figure 3.2) [58]. The absorption is thus higher for the magnetic moment and photon polarization aligned parallel at the L_3 absorption edge. Right circularly polarized light has a polarization downstream, directed from the x-ray source to the sample, and considering the 30° tilted sample mounting, the corresponding directions of the magnetization can be deduced from the contrast in the magnetic structures of Figure 4.1. The arrows, representing the magnetization direction of the magnetic contrast, were added for a $1.5 \mu\text{m} \times 1.5 \mu\text{m}$, 40 nm thick Permalloy element for right circularly polarized light. The magnetization distribution can be evaluated in the same way for the other structures using the corresponding magnetic contrast.

4.1.4 Element specificity

Spin valve systems (SVS) have attracted considerable interest because of their potential in applications such as non-volatile magnetic random access memories (MRAMs) and read heads in magnetic hard disk drives [86]. In its simplest form, the SVS consists of two magnetic layers with different coercivity, respectively called soft and hard magnetic, separated by a non-magnetic spacer layer. The magnetization of one ferromagnetic hard layer can be fixed by an adjacent

antiferromagnetic layer (the pinning layer) through exchange bias coupling. The performance of the SVS depends critically on the way the magnetization distribution evolves under the application of an external magnetic field. Up to now, much attention has been paid to the study of the transport properties and its dependence on the roughness or chemical homogeneity of the interface [87]. However, many other effects such as magnetization reversal processes, domain formation and the implication of the domain structure of each magnetic layer, have only recently been considered [88].

Micromagnetic mechanisms can lead to a coupling between magnetic layers across non-magnetic spacer layers in thin film, multilayered structures [1]. These mechanisms are closely related to the microscopic properties of the films such as structure or morphology, but also to the purely magnetic microstructure, i.e. the magnetic domain structure. In the latter case, a coupling is mediated by magnetostatic stray fields like from domain walls. Up to now, relatively little work was focused on the micromagnetic interactions in the magnetic interlayer coupling. This may be due to the lack of adequate techniques, which must not only provide microscopic lateral resolution but also allow layer selective probing of the magnetic domain structure.

An elegant solution is provided by high resolution soft x-ray microscopy. It was already noted that the XMCD effect has element specific properties. Stacks of different ferromagnetic layers can thus be studied by tuning the photon energy to the corresponding absorption edges of the different layers. Figure 4.2 shows an overview of trilayer stacks composed of Permalloy(20 nm)/Cu(10 nm)/Co(20 nm). The magnetic contrast of the two ferromagnetic layers was recorded at the L_3 absorption edges of Ni (852.7 eV) and Co (778.1 eV) in the right and left panels of Figure 4.2, respectively. The lateral dimension of the squares is about $1.5 \mu\text{m}$ and the diameter of the disks is $2 \mu\text{m}$. The magnetic configuration for individual layers should, based on the thickness and lateral dimension of the patterns, exhibit a vortex structure. Nevertheless, as illustrated in the figure, different kinds of magnetostatic coupling phenomena appear in such stacks of magnetic layers [1]. The coupling can alter the magnetic configuration drastically, and the simple principles introduced by van den Berg [27, 28, 29] to predict the domain configuration, are no longer applicable here. This can be observed for several patterns in Figure 4.2. In remanence, a vortex structure appears in only about half the cases in the Co layer, but in general the coupling between both layers alters completely the domain configuration and a simple vortex structure cannot be observed. In the last row, a clear vortex structure can be visualized in both layers. The circu-

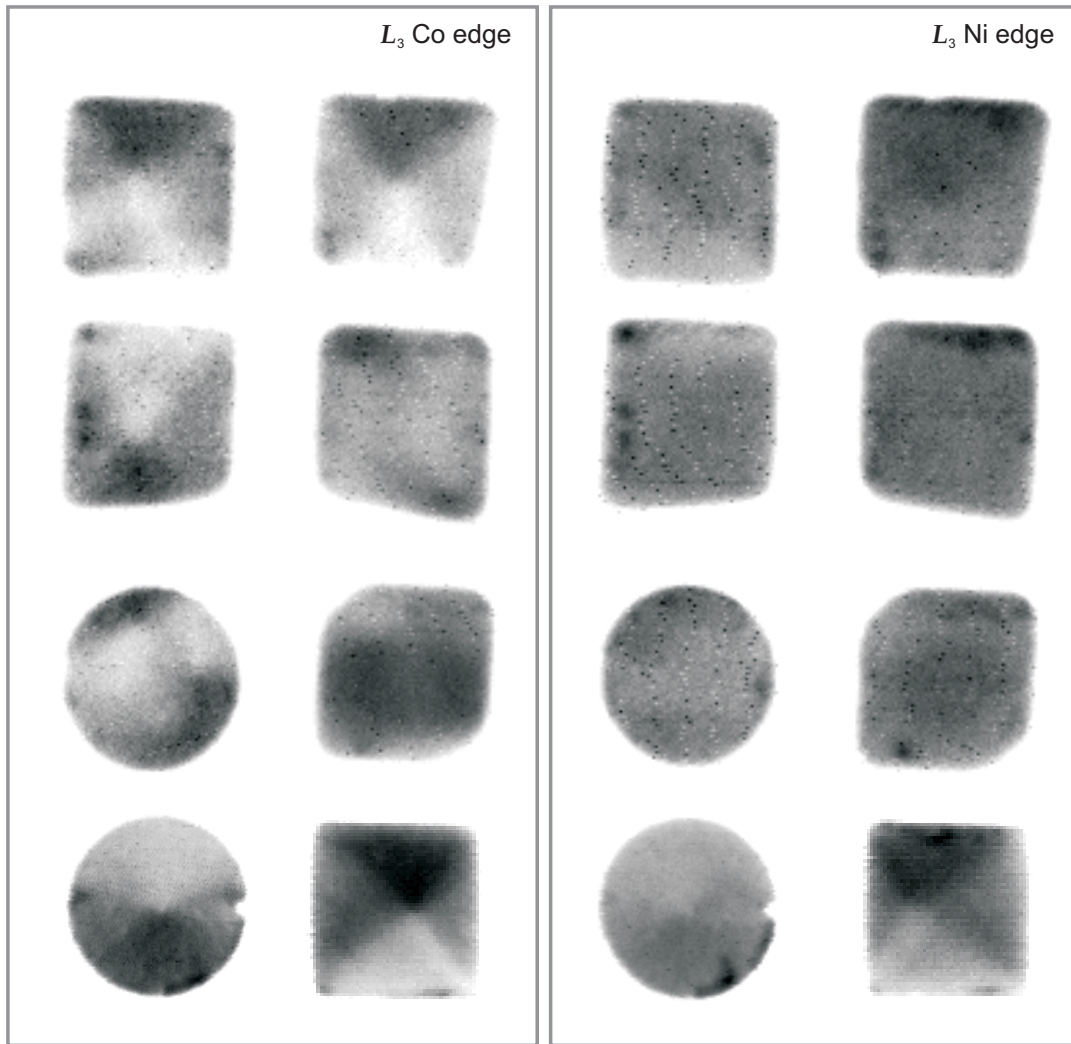


Figure 4.2: STXM images taken for zero external field at the L_3 absorption edges of Ni (852.7 eV) and Co (778.1 eV).

lation sense of the magnetization is the same in both layers for these stacks. This indicates a ferromagnetic coupling between both layers. Nevertheless, the vortex cores in both layers are seemingly displaced from one another. The stray fields generated by the vortex cores in the two magnetic layers could be repulsing each other and cause this displacement, but crossing domain walls might also result in this effect by creating quasi-Néel walls [89]. The dynamic properties become, due to these additional couplings, extremely more intricate (cf. Section 5.3).

4.2 OUT-OF-PLANE MAGNETIZATION OF A VORTEX STRUCTURE

4.2.1 Setup considerations

To study the out-of-plane distribution of the magnetization in a ferromagnetic thin film structure, the sample is mounted under a 90° angle with respect to the photon direction ($\Theta = 0^\circ$ in Figure 3.14). The magnetic contrast can also be probed with opposite circularly polarized light as presented in Paragraph 4.1.2, and “dichroic images” can be deduced using relation (4.1).

4.2.2 Magnetic contrast of the vortex core

The size and the shape of the magnetic vortex core were already determined on Fe islands by means of SP-STM [31] (cd. Paragraph 2.2.2). Although the lateral resolution of a STXM is not sufficient to resolve the vortex core, the XMCD effect provides a high enough signal to detect the out-of-plane magnetic contrast of the core.

The static magnetic configuration of a $500 \text{ nm} \times 500 \text{ nm}$, 40 nm thick Permalloy square was studied by recording two images with opposite polarization of the photons. The corresponding images are shown in the first row of Figure 4.3. An image Γ^- was taken with left circularly polarized light (upper left picture), and a second image Γ^+ was recorded by reversing the polarization of the x-rays (upper middle picture). The contrast reflects again the transmitted intensity. The darker shades in the contrast can be due to a thickness variation over the structure causing differences in the transmitted intensity. A “dichroic” image Γ^{XMCD} , shown in the upper right part of Figure 4.3, was deduced from both images, using relation (4.1). The adopted method is hereby only sensitive to the out-of-plane component of the magnetization. Hence, the image doesn’t reveal much contrast, but a bright spot can clearly be observed in the “dichroic” image Γ^{XMCD} , representing a vortex core pointing up (defined as opposite to the photon propagation direction). Mechanical vibrations of the sample stage and small drifts of the sample explain the appearance of jitter along the rough edges. Thereafter the direction of the magnetization in the vortex core was reversed by applying short bursts of an alternating magnetic field (cf. Paragraph 5.4.3) and is indeed observed in the change of a white to a black dot in the middle (second row in Figure 4.3). This reversal scheme is very efficient since all ambient conditions are left unchanged as well as the in-plane magnetic configuration of the structure under investigation.

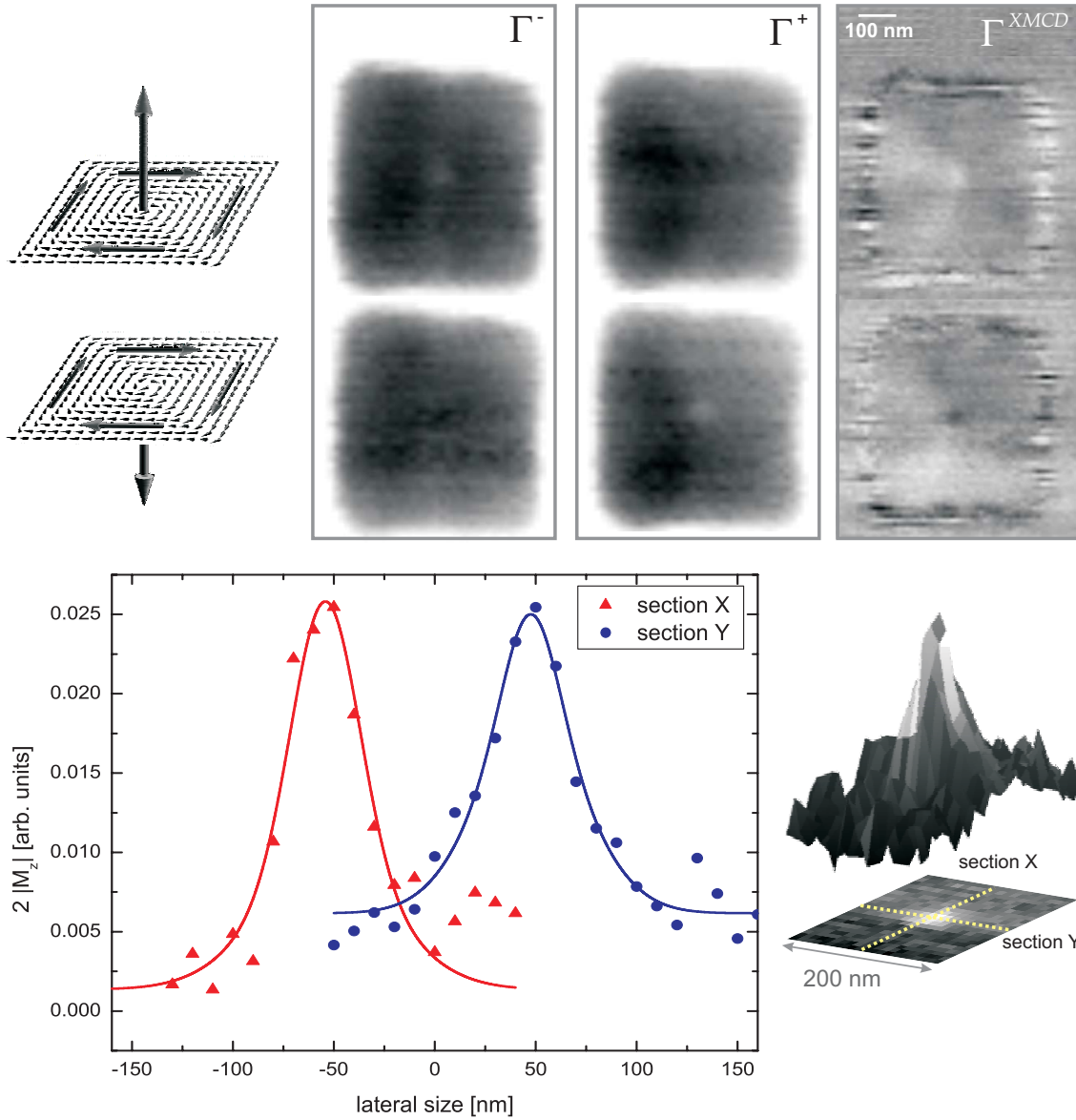


Figure 4.3: Images of the static configuration of a $500 \text{ nm} \times 500 \text{ nm}$, 40 nm thick vortex structure with a vortex core pointing up (against the photon propagation direction – upper row) and down (along the photon propagation direction – lower row). In the first column, images were taken for negative polarization of the photons (Γ^-) while images with opposite polarization (Γ^+) are shown in the second column. The “dichroic” images are depicted in the third column (Γ^{XMCD}). A white or black spot can be observed, corresponding to a vortex core pointing up or down, respectively. Both “dichroic” images were subtracted with one another and a surface plot of the latter is depicted below ($200 \text{ nm} \times 200 \text{ nm}$ cut). The distributions along section X and Y are plotted in the lower left panel with the corresponding fitted profiles in order to estimate the size of the vortex core.

The two “dichroic” images, corresponding to a vortex core pointing up and down, respectively, were thereafter subtracted from one another. A surface plot of this “differential representation” of the out-of-plane magnetic contrast is shown in the lower right part of Figure 4.3. The size of the out-of-plane contrast was

estimated using the out-of-plane profile $\alpha_z(r)$ proposed by Höllinger et al.¹ [26]. A full width at half maximum can be found of about 46 nm through the sections X and Y (lower left panel of Figure 4.3). Considering the instrumental resolution, using Eq. (3.18) ($1.22 \times 25 \text{ nm} = 30.5 \text{ nm}$), a width of 34.4 nm ($= \sqrt{46^2 - 30.5^2}$) can be estimated. On the other hand, micromagnetic simulations, using the OOMMF programme (cf. Paragraph 2.3.2), were performed to estimate the vortex core width. The relaxation was hereby studied for a $500 \text{ nm} \times 500 \text{ nm} \times 40 \text{ nm}$ square. In these calculations, the structure was subdivided in small cells of the size of $1 \text{ nm} \times 1 \text{ nm} \times 40 \text{ nm}$. Standard material parameters were used for Permalloy with $M_s = 8.6 \times 10^5 \text{ A/m}$ for the saturation magnetization, and $A = 1.3 \times 10^{-11} \text{ J/m}$ for the exchange constant. The magnetocrystalline anisotropy was neglected. A full width at half maximum of 21 nm was found eventually, using the profile function given by Eq. (4.2). The width obtained in the measurements is clearly an overestimate of the real vortex core width. A possible explanation is that in the current analysis only the resolution of the zoneplate was taken into account but other broadening effects were not considered like mechanical vibrations, aberration effects, sample drifts etc. Assuming the simulated vortex core width is a correct value, a maximum experimental resolution could then be estimated of about 41 nm.

The maximum magnetic contrast for the out-of-plane signal of the vortex core should correspond to the dichroic signal of Ni in Permalloy, which is about 25% [58, 91]. On the other hand, the width of the vortex core can be estimated using micromagnetic simulations, and a value of 21 nm can be found (see above). A simplified profile of the vortex core can be adopted by taking a Gaussian distribution. The measured magnetic contrast can then be evaluated after a broadening of the contrast with the maximum experimental resolution (41 nm), by assuming a constant area of the Gaussian profile. A maximum magnetic contrast of about 12% can then be found, which is more than a factor of 10 larger than the contrast which is observed experimentally. A deviation of less than 1 eV from the absorption edge can already cause such a large loss in magnetic contrast.

¹The adopted out-of-plane profile is an expansion of the approximation used by Feldtkeller and Thomas [90]:

$$\alpha_z(r) \equiv n_1 + n_2 \left(ce^{-\frac{r^2}{\ell_s^2}} + (1-c)e^{-\frac{r^2}{4\ell_s^2}} \right), \quad (4.2)$$

with ℓ_s the exchange length (see Eq. (2.14)), n_1 and n_2 two normalization factors, and c a term that depends on the thickness of the sample.

CHAPTER 5

MAGNETIZATION DYNAMICS IN FERROMAGNETIC VORTEX STRUCTURES

*“Bizarre is good!
Common has hundreds of explanations. Bizarre has hardly any.”*
— DR. GREGORY HOUSE

Three main ingredients are needed for the imaging of magnetization dynamics: a pulsed light source, a synchronized fast magnetic field pulse (or alternating magnetic field), and a variable time delay (cf. Chapter 3). Only a few time-resolved imaging techniques could implement successfully the fore mentioned ingredients. The excitation and relaxation processes in ferromagnetic structures can be imaged by means of time-resolved magneto-optical Kerr microscopy [92]. Hereby short polarized light pulses are generated by lasers. The lateral resolution is limited by optical diffraction effects and may reach values of about 300 nm. The time resolution is given by the width of the laser pulses. Solid state lasers and fast laser diodes deliver pulses in the 10 ps range. Shorter pulses in the order of 50–100 fs are obtained, if these picosecond pulses are used to pump a mode-locked Ti:sapphire oscillator. On the other hand, a better lateral resolution of about 20–40 nm is achieved using x-ray based imaging techniques. The time resolution is, as formerly described, given by the width of the photon flashes and is about 70–100 ps.

The presence of specific excitation modes in thin film magnetic structures was mentioned in Paragraph 2.3.1. One of the modes appearing in magnetic vortex structures corresponds to the gyrotropic motion of the vortex core around the structure-centre and can be observed by exciting the structure with an in-plane magnetic field. The stroboscopic technique described in Section 3.5, is used to image this gyration. Results on the imaging of the gyrotropic mode are presented in this chapter. Primarily a differential imaging technique is introduced to study the movement of magnetic vortex structures. A more thorough description follows

of the magnetization dynamics observed in such thin ferromagnetic structures. The time dependent spatial distribution of the magnetization $\mathbf{M}(\mathbf{r}, t)$ was imaged using the scanning transmission x-ray microscope (STXM) at the Advanced Light Source. The non-linear response of magnetic vortex structures will be illustrated in detail from the in-plane as well as the out-of-plane magnetic contrast.

5.1 DIFFERENTIAL IMAGING OF MAGNETIC VORTEX STRUCTURES

The application of an alternating in-plane magnetic field on a magnetic structure with a single vortex, at a frequency near the resonance frequency of the vortex structure, leads to a forced gyrotropic motion. The gyration frequency is then equal to the excitation frequency. To image the in-plane magnetization, the sample is tilted over 30° with respect to the plane perpendicular to the incoming photon beam. During the measurements, the phase of the excitation can be changed electronically by 180° at a ± 10 kHz rate and the amount of transmitted photons is then recorded in two separate counting channels with a phase difference of 180° with respect to the external field. On the other hand, this “lock-in” method is not necessary when the frequency is chosen more carefully using an appropriate frequency grid (cf. Paragraph 3.5.3). Eventually a differential image can be derived by subtracting two counting channels with a phase difference of 180° , as shown in Figure 5.1. [16]. The employed imaging technique records only those effects which are synchronized with the probing x-ray flashes. In addition the differential technique removes all non-magnetic contributions, hereby improving the signal-to-noise-ratio. This differential imaging technique demonstrates a very high sensitivity to the magnetization dynamics in confined structures.

The pictures in column I and column II illustrate the consecutive states of the vortex structure during the gyrotropic motion, and differ by a 180° phase change in the motion due to a 180° phase difference of the sine excitation. The pictures show again the transmitted intensity, where the black colour reflects a lower transmission while the white colour represents a higher transmission. The gray side domains correspond to a transmitted intensity in between the former two ones. The subtraction of the contrast from the corresponding pictures (column I minus column II) results in black (low, negative signal) or white (high, positive signal) dots and crosses. It can easily be understood that a displacement up (or down) creates a full black (or white) dot and a displacement left (or right) creates a white/black (or black/white) cross, respectively. In the last column, measured data were added as an illustration for the differential imaging. The

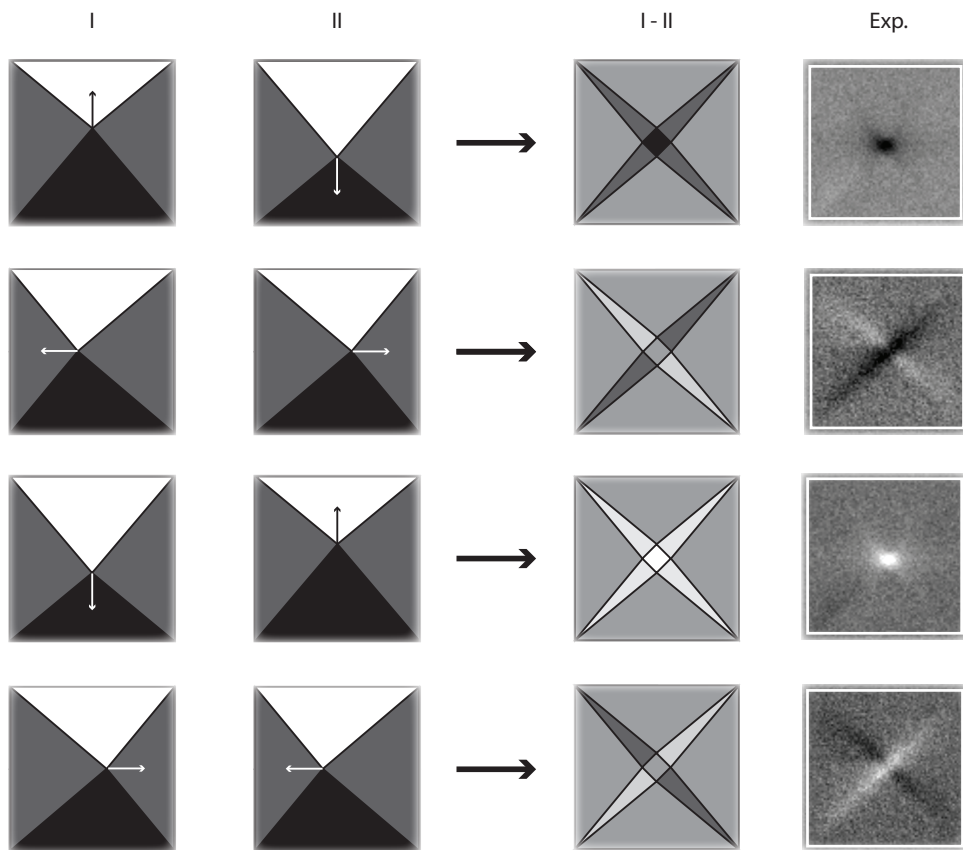


Figure 5.1: Differential imaging – look-up table I.

sense of gyration is simply deduced from the sequence of differential images. A counterclockwise motion can be deduced from the pictures in Figure 5.1 (column I). A change in sense of gyration of the vortex structure will result in a different sequence of differential images.

This technique is not restricted to the use of images with a 180° phase change. The same principle also applies with respect to, e.g. an equilibrium state of the vortex structure. The interpretation of the differential images needs to be adjusted accordingly. In case the dynamic response of a ferromagnetic vortex structure needs to be compared to its equilibrium state, an image of the structure in its relaxed state can be recorded without externally applied fields. This image can then be used as reference and would for example form column II in Figure 5.1. Subtraction from column I by column II will result in different differential images as the one shown in Figure 5.1 (cf. Paragraph 5.2.1).

The same differential technique can also be used for images recorded under a 90° angle with respect to the incoming photon direction. For structures with a sin-

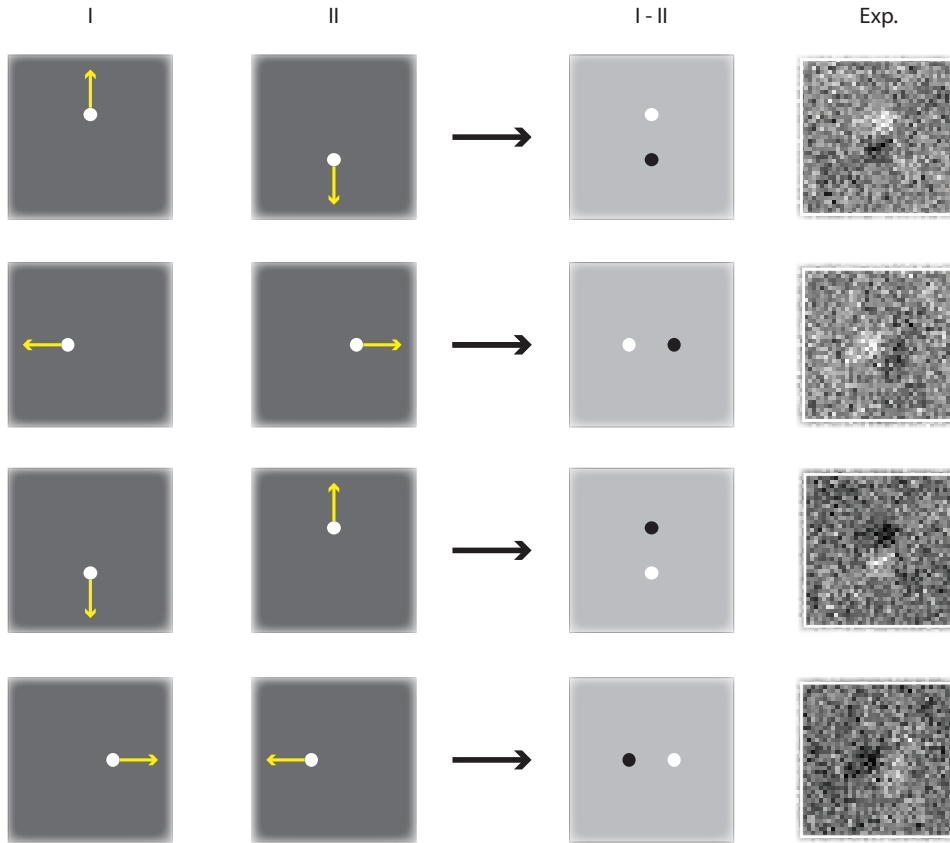


Figure 5.2: Differential imaging – look-up table II.

gle vortex, two dots – a bright and a dark dot – are observed representing the out-of-plane component of the magnetization at the core. The vortex gyration is then again imaged at different phases with respect to the external field. Figure 5.2 shows a full counterclockwise turn of the vortex core, together with the corresponding differential images, showing a bright and a dark dot. Measured data were again added in the last column as an example. Remark that, although the lateral resolution of the STXM is not capable to resolve the vortex core structure, the XMCD effect, together with the high intensity circularly polarized x-rays from an undulator source, is sensitive enough so that an out-of-plane magnetic contrast can be detected. The observed signal however is broadened by the lateral resolution of the imaging technique.

5.2 GYROTROPIC MODE

The gyrotropic mode was already observed by several different techniques. In the early work of Argyle et al. the gyrotropic motion was inferred from the analysis of the domain wall resonance using the optical Cotton-Mouton effect [40]. The

structures were excited with an in-plane alternating magnetic field and the frequency was swept in order to find the resonance frequency. The gyrotropic mode could also be detected by pulsed excitation, using time-resolved Kerr microscopy [41, 42] and photo-emission electron microscopy [93, 43]. Domain wall excitations were also observed with these two techniques [41, 43]. Time-resolved Kerr microscopy provides in addition a large variety of spin wave modes [41, 42, 36, 37]. Although the time resolution is amply sufficient to resolve the gyrotropic mode in structures with micron and sub-micron size, the lateral resolution of the latter techniques reveals to be insufficient to study the details of the gyrotropic motion. The dynamic properties of magnetic vortices can also be probed using a vector network analyzer in the microwave reflection mode, giving quantitative information on different resonant modes but no spatial information [94]. Time-resolved x-ray microscopy, on the other hand, is capable of combining a good time resolution with the necessary lateral resolution [16]. This will be illustrated in the following paragraphs.

5.2.1 Resonant behaviour under pulsed excitation

After excitation of a vortex structure with an in-plane magnetic field pulse, the vortex core gyrates back to its equilibrium state over many turns. The following pump and probe measurements were performed in multi bunch mode. A $1\ \mu\text{m} \times 1\ \mu\text{m} \times 40\ \text{nm}$, respectively $1.5\ \mu\text{m} \times 1.5\ \mu\text{m} \times 40\ \text{nm}$, Permalloy structure was excited every 82 ns with a magnetic field pulse (pulse height $\approx 3\ \text{kA/m}$; pulse width $\approx 500\ \text{ps}$; rise time $\approx 200\ \text{ps}$). The images were recorded in steps of 250 ps before and after the pump pulse, and the sample was tilted by 30° with respect to the plane perpendicular to the incoming photon beam. The in-plane magnetic contrast of the structures are shown in the graphs of Figures 5.3 & 5.4. Differential images were made with respect to the equilibrium state of the vortex structure and a part of the sequence of the gyrotropic motion is shown for both patterns in the first row of Figures 5.3 & 5.4 (cf. Section 5.1). It was unusual to still observe a gyrotropic motion for the $1.5\ \mu\text{m} \times 1.5\ \mu\text{m}$, 40 nm thick element after 82 ns (not shown). This means that the Landau pattern was repeatedly excited while it was not yet fully relaxed. Such long relaxation times do not correspond to earlier experimental results where the structure is already fully relaxed after 16 ns [16, 42]. Micromagnetic simulations even suggest the structure to be relaxed after 16 ns [95]. A change in damping behaviour can usually be induced by sample imperfections. The same batch of samples was being investigated in the current paragraph, so no large discrepancies are expected.

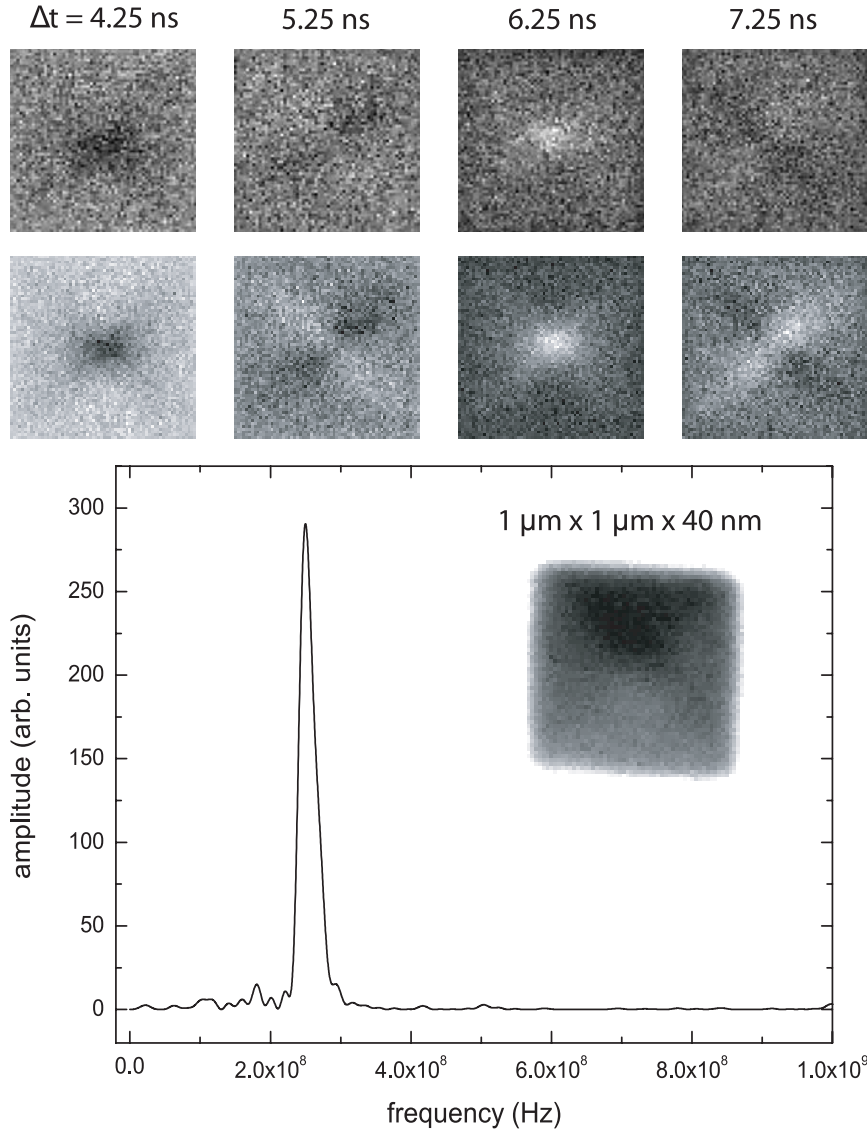


Figure 5.3: Dynamic response for a $1 \mu\text{m} \times 1 \mu\text{m}$, 40 nm thick element, observed by pulsed excitation in multi bunch mode. In the upper row, raw differential images are shown with respect to the equilibrium state of the vortex structure, at four different time steps after the pump pulse. The lower row gives the filtered differential images. The graph shows the fast fourier transform taken from the time dependent differential response. The in-plane magnetic contrast of the structure is added as an inset in the graph.

In order to deduce the resonance frequency of the gyrotropic motion, the root-mean-square intensity¹ was calculated from the differential contrast. For this, a small area ($300 \text{ nm} \times 300 \text{ nm}$) around the vortex centre was cut out. As the

¹Considering an image Γ with $m \times n$ pixels, the root-mean-square intensity Γ_{rms} can be deduced, for Γ_{ij} the intensity at pixel (i, j) , using the relation:

$$\Gamma_{rms} = \sqrt{\frac{1}{m} \frac{1}{n} \sum_{i=1}^m \sum_{j=1}^n \Gamma_{ij}^2}.$$

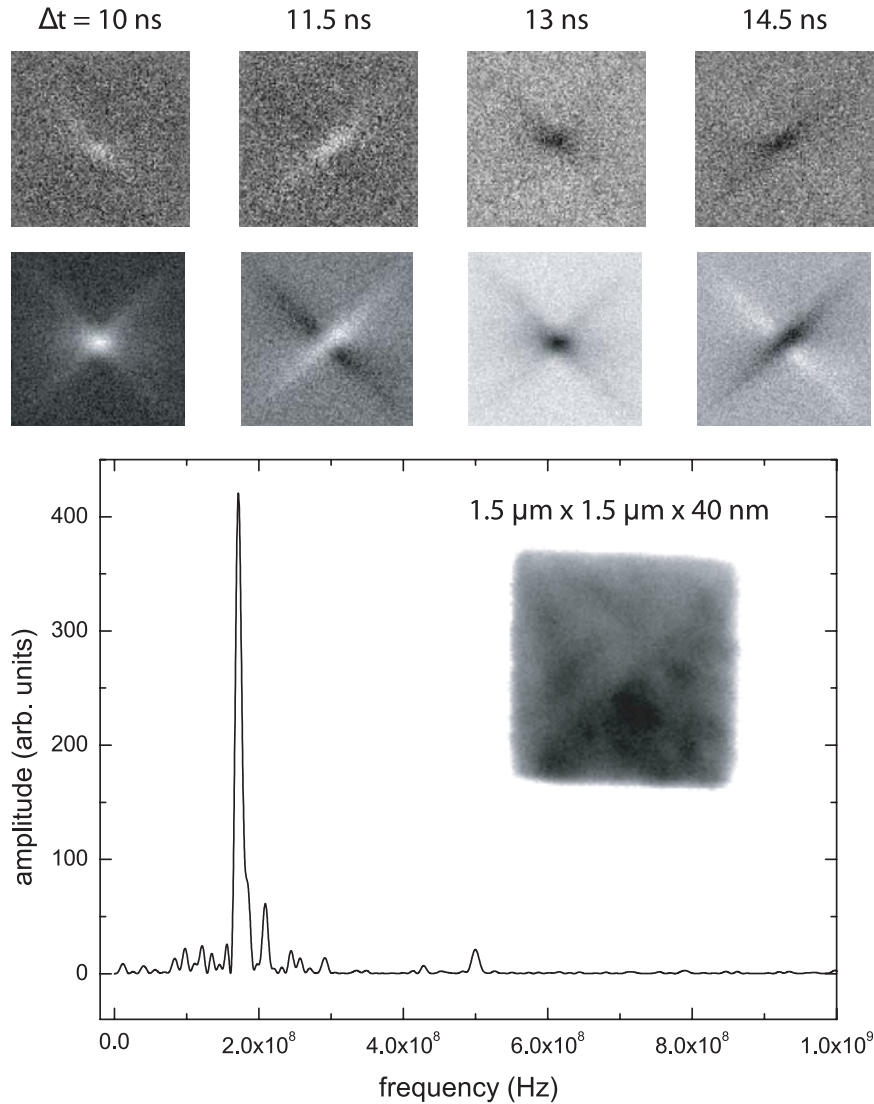


Figure 5.4: Dynamic response for a $1.5 \mu\text{m} \times 1.5 \mu\text{m}$, 40 nm thick element, observed by pulsed excitation in multi bunch mode. In the upper row, raw differential images are shown with respect to the equilibrium state of the vortex structure, at four different time steps after the pump pulse. The lower row gives the filtered differential images. The graph shows the fast fourier transform taken from the time dependent differential response. The in-plane magnetic contrast of the structure is added as an inset in the graph.

differential contrast evolves over several periods from dark dots (minimum contrast) to bright dots (maximum contrast) with in between images with black and white crosses (opposite contrast cancel one another out), the root-mean-square intensity around the vortex centre will show an oscillatory behaviour with a frequency corresponding to the resonance frequency of the excited mode. This intensity is actually proportional to the displacement of the vortex structure in the vertical direction. A fast fourier transform of the oscillatory curve with zero padding, reveals a pronounced peak at the resonance frequency of the gyrotropic motion of about 254 MHz for the $1 \mu\text{m} \times 1 \mu\text{m}$, 40 nm thick element (graph

in Figure 5.3), and a value of 172 MHz can be found for the $1.5 \mu\text{m} \times 1.5 \mu\text{m}$, 40 nm thick element (graph in Figure 5.4). A small peak at 500 MHz (and its harmonics) reflects the 2 ns spacing of the probing x-ray flashes used for the imaging, which can be considerably reduced using an appropriate normalization of the data. Beside the occurrence of these peaks, small satellite peaks can be observed around the “gyrotropic” peak, at the right side, indicating different resonance frequencies in the vortex structure. Additional results supporting this observation will be treated in Paragraph 5.4.6. A more detailed analysis using point-by-point fast fourier transformation and an additional back transformation for the corresponding mode at its specific resonance frequency results in clear differential images of the gyrotropic motion, in the form of clear dots and crosses. This is shown in the second row of the Figures 5.3 & 5.4, respectively.

The resonance frequency of the gyrotropic motion was also deduced using the previously described method for a series of square- and circular-shaped ferromagnetic structures with lateral size L ($= 500 \text{ nm}, 1000 \text{ nm}, 1500 \text{ nm}$) and thickness d ($= 30 \text{ nm}, 40 \text{ nm}, 50 \text{ nm}$), and is plotted as a function of the aspect ratio $\delta = d/L$ in Figure 5.5. The resonance frequency is in first order linear as a func-

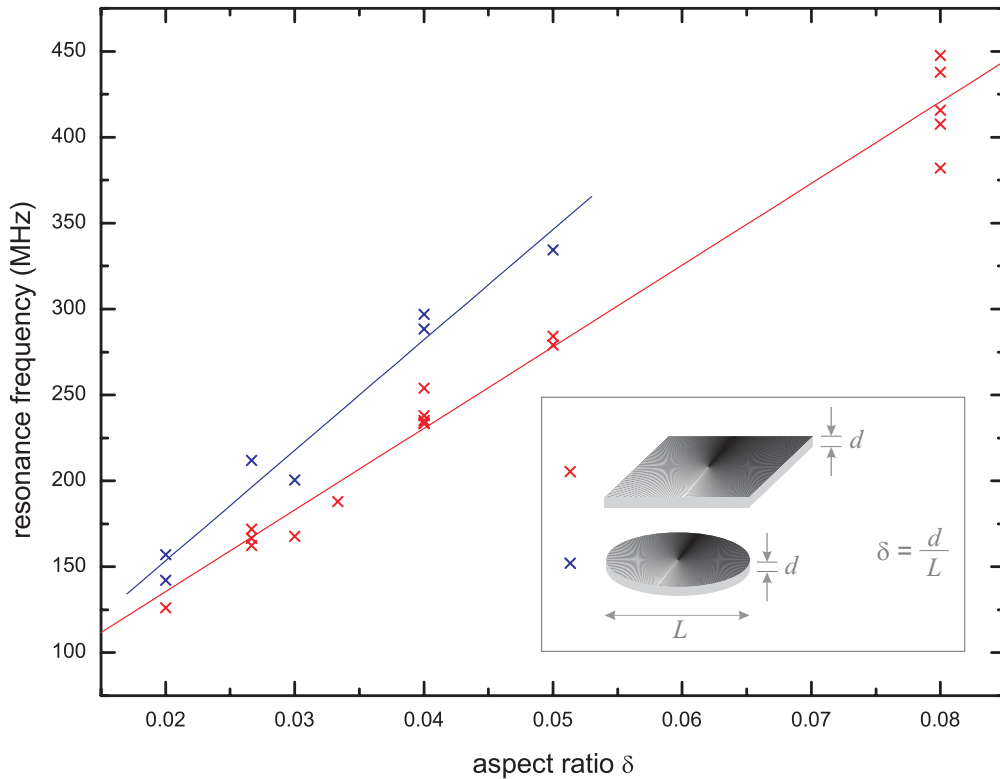


Figure 5.5: Resonance frequency as a function of the aspect ratio δ for a series of square- (red) and circular-shaped (blue) Permalloy structures, observed by pulsed excitation in multi bunch mode.

tion of the aspect ratio [95, 42, 96]. Smaller lateral sizes and/or thicker structures will result in a higher resonance frequency. Nevertheless, caution is needed in extrapolating these results. A limit will be reached for too low and too high aspect ratios where a single vortex structure no longer exists (cf. the results described in Figure 5.11).

5.2.2 Resonant sine excitation

In-plane magnetization configuration

- The gyrotropic motion in magnetic vortex structures can also directly be observed when it is excited with a continuous alternating magnetic field. As mentioned in previous paragraph, the vortex structure will be driven by the exciting field and respond with the same frequency as the former one. Tuning the excitation frequency f near the resonance frequency of the gyrotropic mode will thus induce more effectively the gyrotropic motion in the vortex structure. This motion is depicted in Figure 5.6 for a $1.5 \mu\text{m} \times 1.5 \mu\text{m}$, 50 nm thick Permalloy square. The images were recorded with the sample tilted over 30° with respect to the plane perpendicular to the incoming photon beam. The frequency f was set to 250 MHz and the amplitude H_0 of the alternating field was about 1095 A/m.

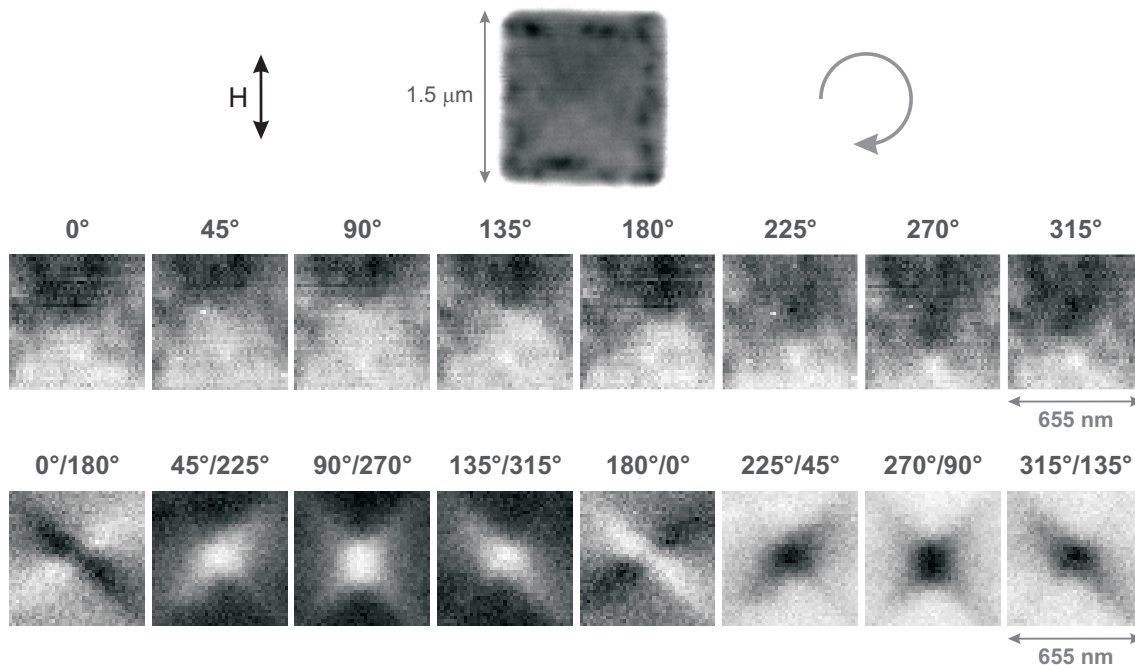


Figure 5.6: Dynamic response for a $1.5 \mu\text{m} \times 1.5 \mu\text{m}$, 50 nm thick vortex structure, excited by a continuous alternating magnetic field ($H_0 = 1095 \text{ A/m}$, $f = 250 \text{ MHz}$). The static in-plane configuration of the Landau pattern is depicted on top of the figure. The upper row shows the in-plane contrast of the vortex structure at eight different phases with respect to the external field. The lower row shows the corresponding differential images.

The static in-plane configuration of the Landau pattern is depicted on top of the figure. The vortex structure was on top of a straight horizontal stripline, so the in-plane alternating field varies in the vertical direction. A displacement in the vertical direction is clearly visible from the image-cuts of the in-plane contrast (upper row). The clockwise gyrotropic motion is on the other hand clearly observed in the sequence of differential images (lower row), using the look-up table from Figure 5.1, but less clearly from the in-plane contrast. Although, the resonance frequency of the gyrotropic mode was not determined and is not known, the appearance of the motion indicates that the used excitation frequency is near the resonance frequency.

It is at this point also appropriate to remark that the differential images need to be interpreted with some vigilance when the sample is tilted over 30 degrees. All components of the magnetization which have a projection along the photon direction will, due to the XMCD effect, contribute to the magnetic contrast. For a vortex structure tilted over 30 degrees, not only the in-plane magnetization in the domains will contribute but also the out-of-plane component at the core-centre. This contribution, although small, will appear as well in the differential images and a straightforward separation is fairly impossible.

- The extent of the vortex core displacement during the gyrotropic motion was also investigated as a function of the amplitude of the alternating magnetic field H_0 , and is shown in Figure 5.7. The images were recorded for a $1.5 \mu\text{m} \times 1.5 \mu\text{m}$, 40 nm thick Permalloy square, at eight different phases with respect to the exciting field. The frequency f of the alternating field was set to 187.5 MHz. The static in-plane configuration of the Landau pattern is depicted in the figure. The displacement (diameter) of the gyrotropic motion was deduced from the differential contrast, which was evaluated at every phase step. The contrast is larger for increasing displacement of the vortex core. A motion could be observed even below 80 A/m. The displacement is practically constant for field amplitudes up to about 100 A/m. The vortex structure responds linearly above 110 A/m. At slightly higher field amplitudes, around 300 A/m, non-linear processes occur, which will be discussed in Section 5.4.

The displacement of the vortex core during the gyrotropic motion is proportional to the speed of the core. Assuming a circular trajectory in first approximation, the diameter D ranges from 150–240 nm ($D = 2r$, with r the radius of the trajectory), and taking into account a driving frequency of 187.5 MHz, the speed can be

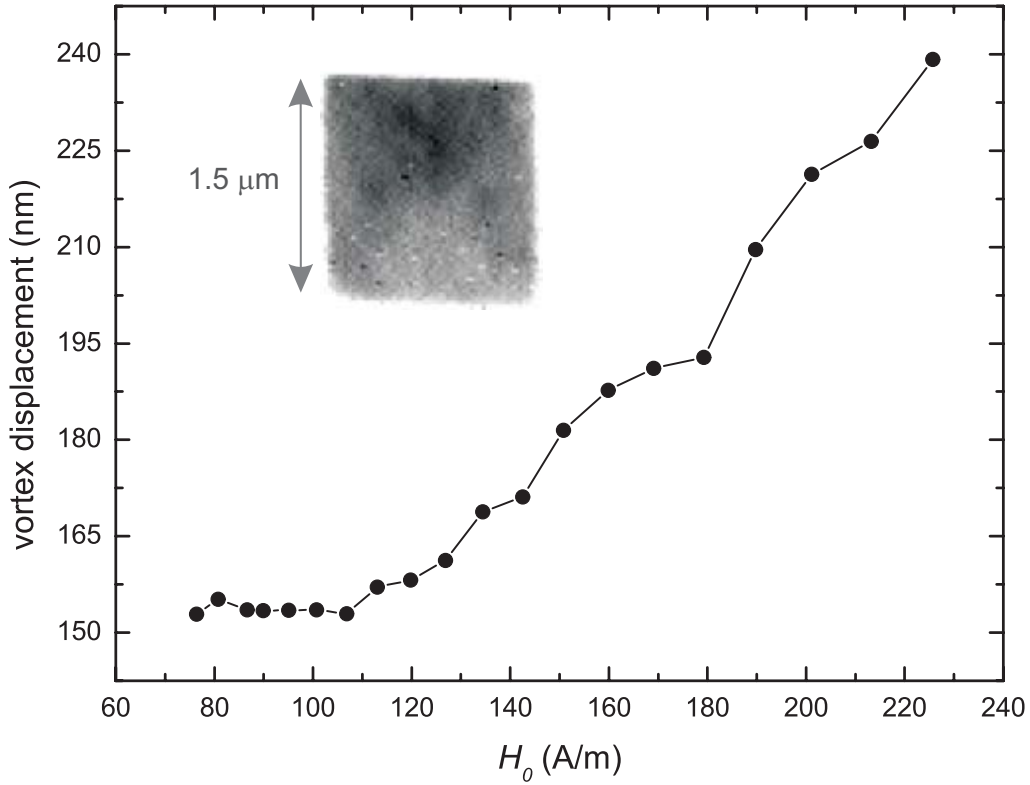


Figure 5.7: Vortex core displacement during the gyrotropic motion, as a function of the amplitude of the alternating magnetic field ($f = 187.5$ MHz), for a $1.5 \mu\text{m} \times 1.5 \mu\text{m}$, 40 nm thick Permalloy element.

expressed as:

$$v_{core} = 2\pi r f, \quad (5.1)$$

resulting in velocities v_{core} ranging from 88–141 m/s (for $D = 150$ –240 nm).

- The gyrotropic motion was also observed for other shapes containing a single vortex, e.g., triangles, circles, etc. Figure 5.8 shows the gyrotropic motion for an ellipse with diameters along the long and short axis of 960 nm and 640 nm, respectively. The motion of the vortex structure was imaged at different excitation frequencies. The images were recorded with the sample tilted by 30° with respect to the plane perpendicular to the incoming photon beam. The amplitude of the applied field was about 1120 A/m. The in-plane dichroic contrast of the vortex structure is depicted on top of Figure 5.8. The gyrotropic motion of the single vortex is nicely observed in the differential images, evolving from crosses to dots, when it is excited with an alternating field with a frequency f set to 437.5 MHz. This indicates that the chosen excitation frequency was close to the eigenfrequency of the gyrotropic mode. At a lower value of the frequency (312.5 MHz) the differential contrast shows a continuously changing black/white

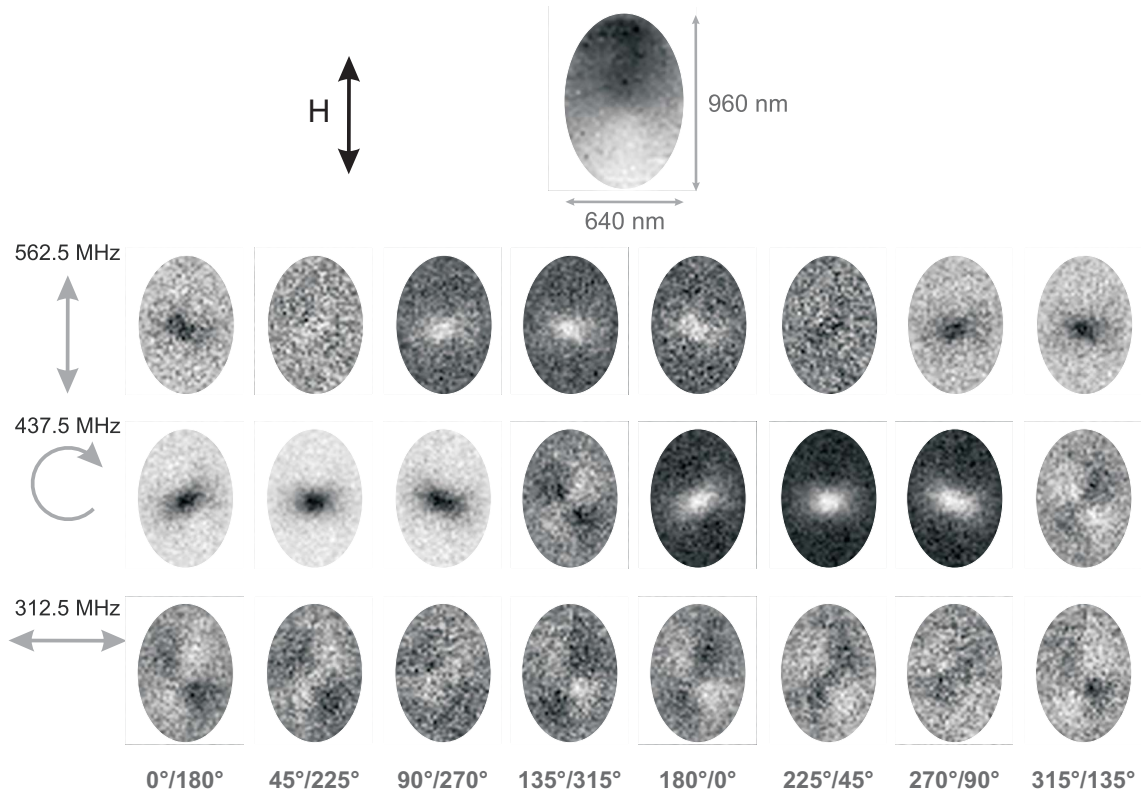


Figure 5.8: Dynamic response for a $640 \text{ nm} \times 960 \text{ nm}$, 40 nm thick ellipse, excited with an alternating magnetic field, near the resonance frequency (middle row), below the resonance frequency (lower row), and above the resonance frequency (upper row). The in-plane dichroic contrast of the vortex structure is depicted on top of the figure and the external magnetic field varies in the vertical direction, considering a horizontal stripline ($H_0 = 1120 \text{ A/m}$).

cross, indicating a pronounced left/right motion; while at a higher frequency (562.5 MHz), the core clearly starts moving up and down, which can be distinguished by the black and white dots.

The sample was excited using a horizontal stripline (Figure 3.13), and so an alternating field \mathbf{H} is induced vertically. Although no domain walls are present in an elliptical (or circular) structure and the flux closure pattern is formed by a continuously varying, in-plane magnetization, the vortex structure can be approximated by a structure with four in-plane “domains” similar to a Landau configuration. A clear gyrotropic motion can be observed in a vortex structure with a frequency of the excitation close to the resonance frequency, but at excitation frequencies lower than the resonance frequency, the “domains” will mainly evolve with the external field. In this case, the “side domains” with opposite vertical magnetization enlarge and shrink with the external field, respectively. This causes a left/right motion, which is mainly governed by the damping behaviour of the system (cf. also the LLG equation (2.19)). For a frequency higher than the

resonance frequency, the precessional term gains in importance. The influence on the “side domains” becomes less important but the torque, experienced at the core and the upper and lower “domains”, becomes primordial. This eventually results in a movement up and down of the vortex structure.

Out-of-plane magnetization configuration

- The gyrotropic motion can also be imaged for a sample placed under 90 degrees with respect to the incoming photon beam. Figure 5.9 shows the results for a $1\ \mu\text{m} \times 1\ \mu\text{m}$, 50 nm thick Permalloy square. The sample was excited with an in-plane magnetic field with a frequency f of 312.5 MHz, and an amplitude of 800 A/m. The out-of-plane contrast of the vortex structure is depicted on top of the figure. Except for the appearance of two darker spots in the structure, no further magnetic contrast can be distinguished.

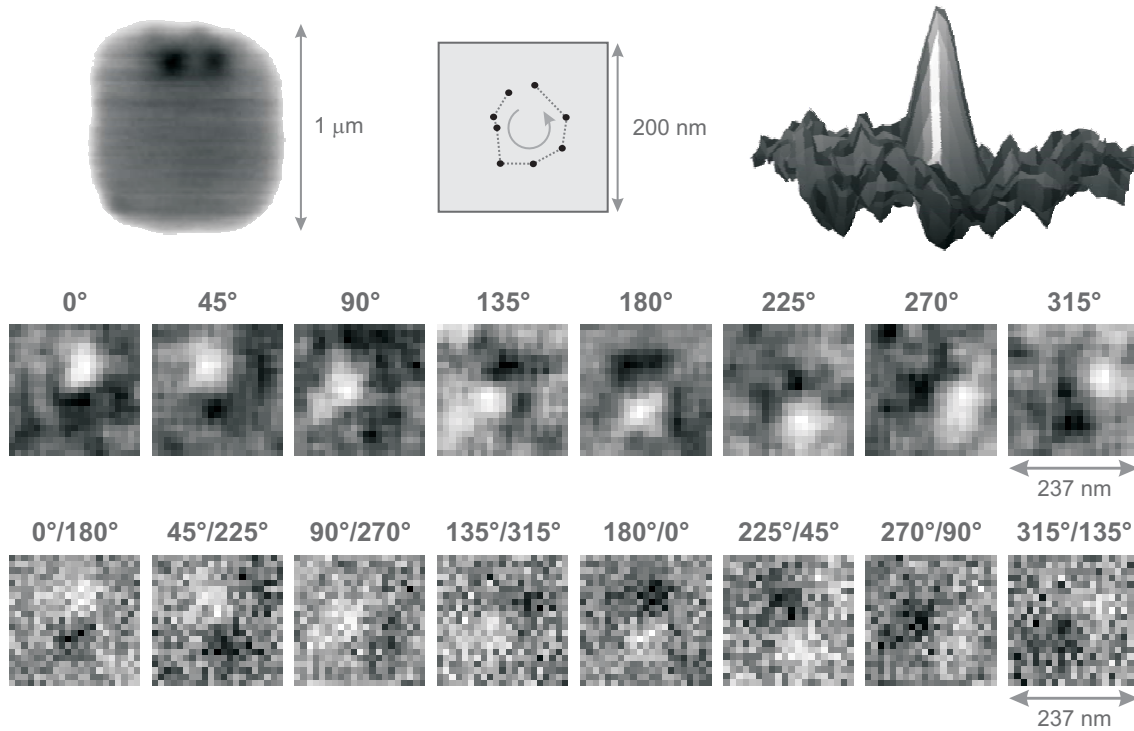


Figure 5.9: Gyrotropic motion of a $1\ \mu\text{m} \times 1\ \mu\text{m}$, 50 nm thick vortex structure, excited with an in-plane alternating magnetic field ($H_0 = 800\ \text{A/m}$, $f = 312.5\ \text{MHz}$). The upper row shows the “averaged” out-of-plane magnetic contrast Γ_i^{direct} of the Landau structure at different phases with respect to the external field. The corresponding differential images are given in the lower row. The position of the vortex core at the different phases is depicted in the inset, together with a surface plot of the “average” out-of-plane contrast at phase 0° .

The following procedure was therefore used to improve the signal-to-noise-ratio leading to direct “averaged” images, although introducing artefacts (see below).

An average image Γ_{mean} was deduced, pixel by pixel, from the images Γ_i recorded at eight different phases, with $i = 1, \dots, 8$:

$$\Gamma_{mean} = \frac{1}{8} \sum_{i=1}^8 \Gamma_i. \quad (5.2)$$

All separate images Γ_i were subsequently divided by the average image Γ_{mean} :

$$\Gamma_i^{direct} = \frac{\Gamma_i}{\Gamma_{mean}}. \quad (5.3)$$

The upper row of Figure 5.9 shows the images Γ_i^{direct} at the eight different phases, and reveals the out-of-plane vortex core magnetization. The position of the vortex core at the different phases was extracted, showing a counterclockwise motion of the vortex structure. The same motion can also be observed from the differential images, in the lower row of Figure 5.9, deduced from the corresponding raw images with a phase difference of 180 degrees. The ‘‘average’’ out-of-plane contrast of the vortex core structure is also depicted as a surface plot at phase 0° .

- Although the vortex core itself is well observed in this way, the adopted procedure introduces artefacts in the form of a halo of opposite contrast (dark ‘‘half-rings’’ here) compared to the one of the out-of-plane vortex core itself (white dots here). The halo is more pronounced at certain phases and less at others, which indicates different intensities at different phases. This is illustrated in Figure 5.10 for a $500 \text{ nm} \times 500 \text{ nm}$, 40 nm thick Permalloy sample. The sample was excited with an in-plane magnetic field with a frequency f of 437.5 MHz, and an amplitude of 590 A/m. Instead of recording images at one fixed polarization of the

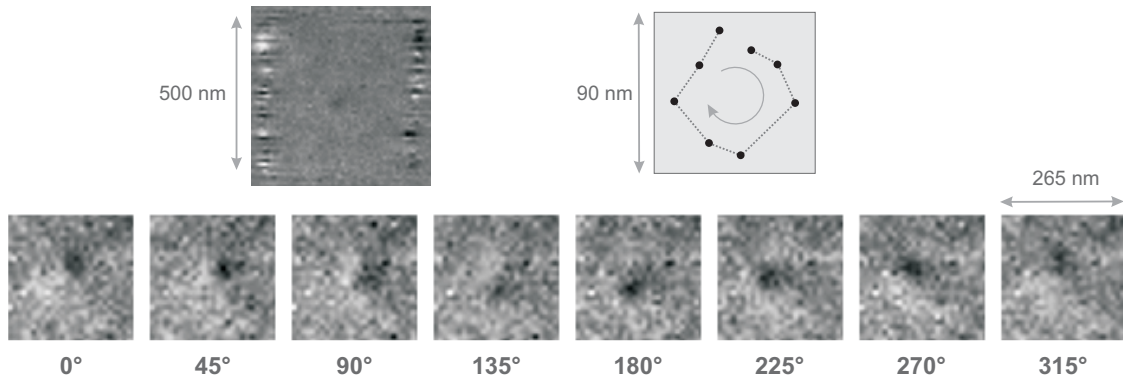


Figure 5.10: Gyrotropic motion of a $500 \text{ nm} \times 500 \text{ nm}$, 40 nm thick vortex structure, excited with an in-plane alternating magnetic field ($H_0 = 590 \text{ A/m}$, $f = 437.5 \text{ MHz}$). The out-of-plane magnetic contrasts $\Gamma_i^{-/+}$ of the Landau structure are shown at the different phases with respect to the external field. The position of the vortex core at the different phases is depicted in the inset.

x-rays, two sequences of images (Γ_i^- & Γ_i^+) were recorded with opposite polarization of the x-rays, respectively. A sequence of “differential” images $\Gamma_i^{-/+}$ was then deduced from both sequences using the relation:

$$\Gamma_i^{-/+} = \frac{\Gamma_i^-}{\Gamma_i^+}, \quad (5.4)$$

and is shown in Figure 5.10. A dark spot can be distinguished representing the out-of-plane magnetization contrast at different phases of the applied in-plane magnetic field. The contrast fades at certain phases (most noticeable at 135°). These intensity changes might indicate a change in the magnetization distribution of the vortex core during the vortex motion. Such distortions in the spin distribution of the moving vortex core were also noticed in micromagnetic calculations [94]. Internal structures of vortices and internal core modes are expected to play an important role in the dynamics of vortices [97].

- The resonance frequency for the gyrotropic motion was already measured as a function of the aspect ratio δ of the vortex structure, and turned out to be proportional to the thickness of the structure but to increase with decreasing lateral size (Figure 5.5). The gyrotropic motion of vortex structures with smaller lateral sizes can thus only be observed when these structures are excited with higher frequencies. Figure 5.11 shows the gyrotropic motion for a relatively small $200 \text{ nm} \times 200 \text{ nm}$, 40 nm thick Permalloy sample. A value of $H_0 = 700 \text{ A/m}$

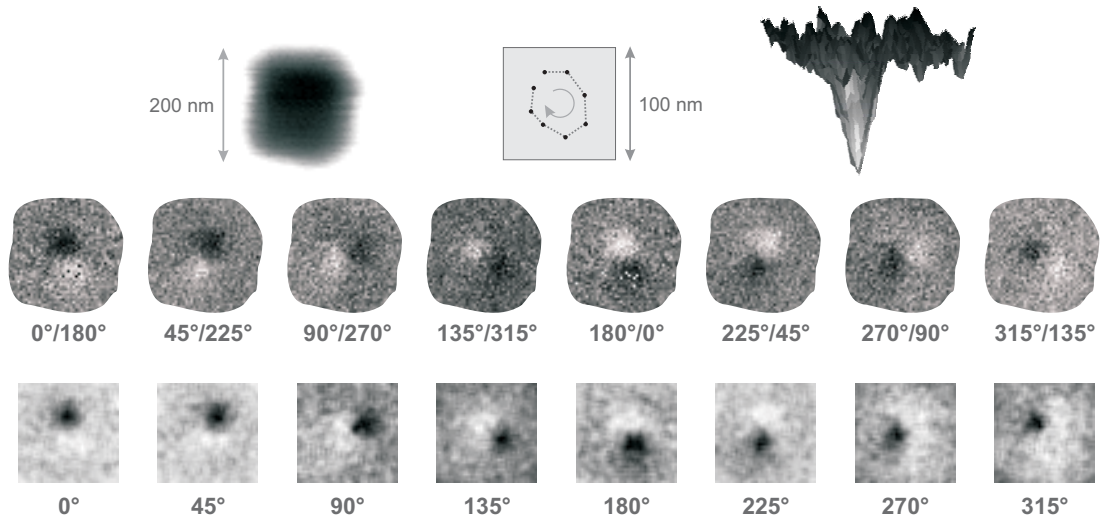


Figure 5.11: Gyrotropic motion of a $200 \text{ nm} \times 200 \text{ nm}$, 40 nm thick vortex structure, excited with an in-plane alternating magnetic field ($H_0 = 700 \text{ A/m}$, $f = 812.5 \text{ MHz}$). The lower row shows the “averaged” out-of-plane magnetic contrast Γ_i^{direct} of the Landau structure at different phases with respect to the external field. The corresponding differential images are given in the upper row. The position of the vortex core at the different phases is depicted in the inset, together with a surface plot of the “average” out-of-plane contrast at phase 0° .

was chosen for the amplitude of the exciting field, and the frequency f was set to 812.5 MHz. The out-of-plane component of the magnetization was recorded and Eqs. (5.2) & (5.3) were used to derive the images. A clockwise motion can clearly be distinguished in the direct “averaged” images (lower row), as well as in the differential images (upper row).

The aspect ratio δ of the current structure is 0.2 and by extrapolating the results of Figure 5.5, a resonance frequency of about 950 MHz can be deduced. The sample in Figure 5.11 had nevertheless the best response when it was excited with an alternating field with a frequency f set to 812.5 MHz. The resonance frequency lies thus lower than expected. This indicates a non-linear relation between the resonance frequency and the aspect ratio, for structures with high aspect ratio. This is most probably related to the larger contribution of the out-of-plane core magnetization in small structures with a single vortex, relative to the in-plane magnetization of its surrounding when compared to larger structures. The out-of-plane magnetization has a much higher relative contribution here compared to structures with a larger lateral dimension, influencing directly its dynamic behaviour.

5.2.3 Driven oscillatory behaviour under burst excitation

The excitation of the gyrotropic mode of a ferromagnetic structure with a single vortex by means of an in-plane alternating magnetic field can be viewed as a classical forced damped harmonic oscillator (cf. Paragraph 5.2.2). The driving force used in the following results is a burst of the alternating in-plane field. The measurements were performed in two bunch mode and the images were recorded with the sample tilted over 30° with respect to the plane perpendicular to the incoming photon beam. Every 328 ns, an in-plane burst excites a $1.5 \mu\text{m} \times 1.5 \mu\text{m}$, 50 nm thick Permalloy sample. The exciting field burst is depicted in the upper part of Figure 5.12. The total length of the burst was about 26 ns with a rising edge and a falling edge of 3 ns and 12 ns, respectively (rising and falling edges from the envelope of the burst). Higher frequency components of the pulser are leaking and can be observed near the end of the falling edge. The maximum amplitude of the burst was about 710 A/m and the frequency f was set to 250 MHz. The static configuration of the Landau pattern is also depicted. The sense of gyration of the vortex structure was deduced in separate measurements using an in-plane alternating magnetic field and a counterclockwise gyration sense could be observed. The phase of the applied field was changed electronically by 180° at a ± 10 kHz rate, thus two phases are recorded in two counting channels with

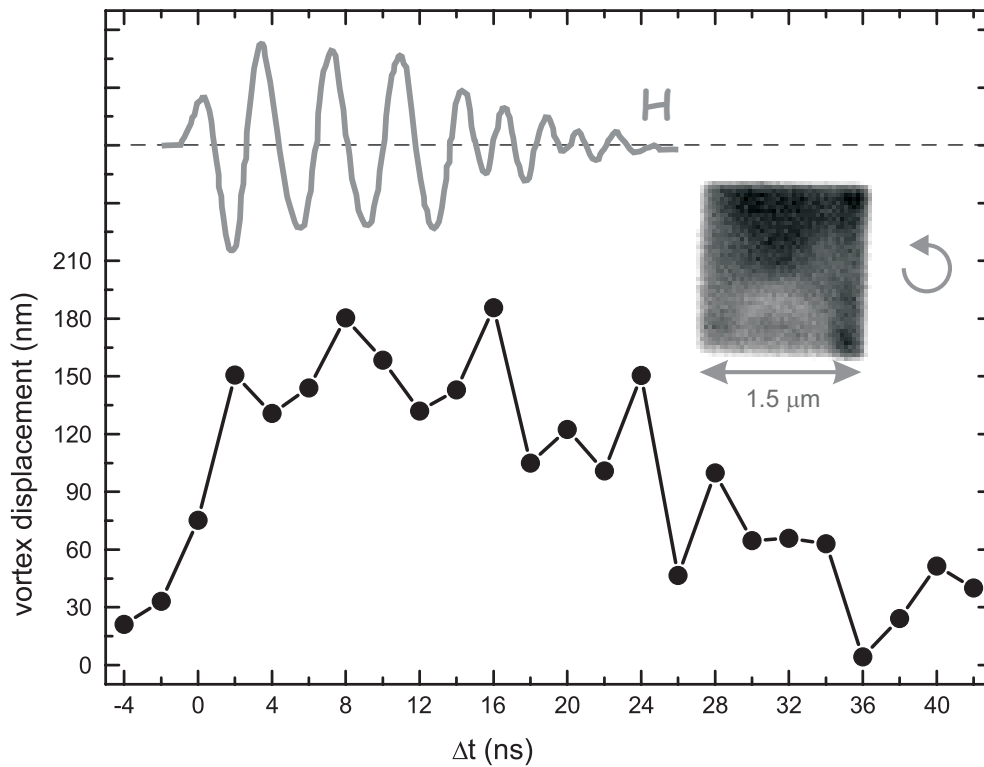


Figure 5.12: In-plane burst excitation of a $1.5 \mu\text{m} \times 1.5 \mu\text{m}$, 50 nm thick Permalloy sample. The shape of the field burst is depicted in the upper part ($f = 250$ MHz). The displacement of the vortex core as a function of time is shown in the lower part. The static configuration of the Landau pattern is depicted with the gyration sense (counterclockwise).

respect to the alternating field. Differential images are deduced using these two counting channels and are shown in Figure 5.13. The dynamic response was probed by delaying the pulses with 2 ns time steps, thus the envelope of the burst is shifted but the phase of the sine field stays fixed.

The vortex core starts gyrating (counterclockwise) when the burst is applied. At the onset of the burst, the differential images in Figure 5.13 show a black/white cross indicating that the vortex core is displaced to the left (see also look-up table I in Figure 5.1). At the full amplitude of the burst ($\Delta t = 4\text{--}14$ ns), the differential contrast varies from a black/white cross to a dark dot, which can be interpreted by a vortex core displaced downwards. At the falling edge of the excitation, the contrast becomes a white/black cross corresponding to a vortex core displaced to the right. A phase shift is thus present in the vortex core motion which increases during the motion. Considering the counterclockwise motion of the vortex structure, the core is then moving in front with respect to the excitation field. The differential contrast continues changing after the burst excitation, until a white dot is reached. This indicates that the vortex structure is then moving

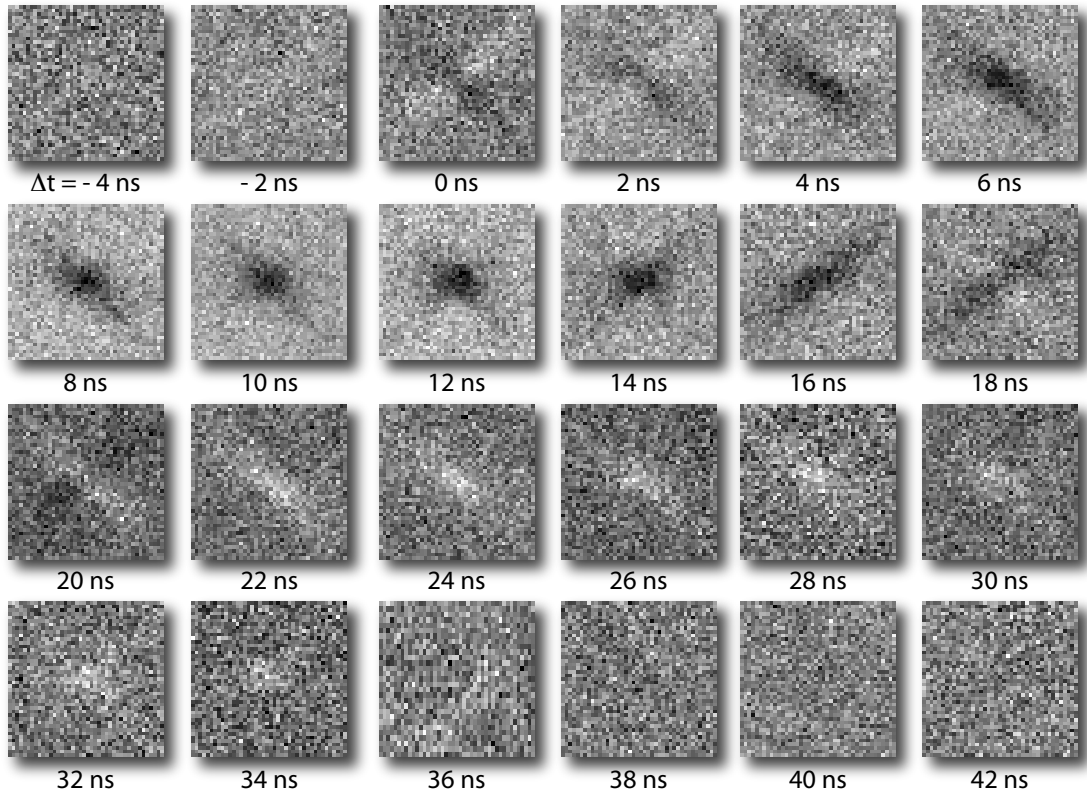


Figure 5.13: Differential images for a $1.5 \mu\text{m} \times 1.5 \mu\text{m}$, 50 nm thick vortex structure excited by an in-plane field burst (upper part of Figure 5.12). The differential images were deduced from the ratio of two images with a 180° phase difference with respect to the alternating field. The time steps Δt correspond to the steps given in Figure 5.12.

at its own resonance frequency, which is higher than the excitation frequency of 250 MHz. After the burst, the contrast also diminishes which illustrates the damping behaviour.

These results show the oscillatory behaviour of the vortex core motion under excitation of an in-plane magnetic field burst. The dynamic response shows also a phase shift in the gyrotropic motion, which increases in function of time. This sample was originating from a different batch as the one studied in Paragraph 5.2.1. The resonance frequency (clearly above 250 MHz) is not corresponding to the results found in Figure 5.5. Considering the aspect ratio of the investigated structure ($\delta = 0.333$), a resonance frequency of about 180 MHz would be expected. This result indicates that large discrepancies can occur for elements of the same geometry, which can never be observed in, e.g., conventional FMR experiments where a large array of the same structures is needed and a deviation of the resonance frequency would be averaged out.

The extent of the displacement of the vortex core is depicted in the lower part of Figure 5.12. Therefore, the distance was evaluated of the different positions of the vortex core, at phases which differ by 180 degrees. Despite the large scatter, considering a spatial resolution of about 40 nm, the displacement of the vortex core follows nicely the envelope of the burst till after the end of the burst, where the relaxation of the gyrotropic motion can be observed.

5.3 DYNAMICS IN COUPLED FERROMAGNETIC LAYERS

By means of the element specific XMCD effect, time-resolved studies were also performed on trilayer systems composed of two different ferromagnetic layers (Permalloy & Co) separated by a non-magnetic Cu layer. An overview of the static configuration in the two ferromagnetic layers was already given in Paragraph 4.1.4. These results indicated that, due to a magnetic coupling, a vortex configuration was not necessarily appearing in the ground state. This eventually complicates considerably the dynamic response of such systems. The following section will be restricted to a trilayer stack where both ferromagnetic layers exhibit a vortex configuration.

The magnetic coupling was investigated for a $1.5 \mu\text{m} \times 1.5 \mu\text{m}$ trilayer stack with an asymmetric edge, composed of Permalloy(20 nm)/Cu(5 nm)/Co(20 nm). The sample was excited with an in-plane alternating magnetic field with an amplitude H_0 of 630 A/m and the frequency f was set to 187.5 MHz. The energy of the x-rays was tuned to the L_3 absorption edges of Ni (852.7 eV) and Co (778.1 eV), respectively, and a series of differential images was taken at different phases with respect to the exciting magnetic field. The dynamic response in both separate layers is depicted in Figure 5.14.

- The sequence of differential images clearly shows a gyrotropic motion in the Permalloy layer, and the sense of gyration can easily be deduced using look-up table I (Figure 5.1) with the core moving clockwise (row (a)).

- The dynamic response in the Co layer, on the other hand, is more intricate. Although the in-plane magnetic contrast is clearly revealing a structure with a single vortex in the middle, a small “domain” can also be observed in the upper left corner of the structure. The differential images show quite some dynamic contrast (row (b)) but a closer look at the centre itself (and at the domain walls) revealed no motion of the vortex core in the Co layer. This can most easily be seen by comparing, e.g., the differential images in the Permalloy and Co layer at

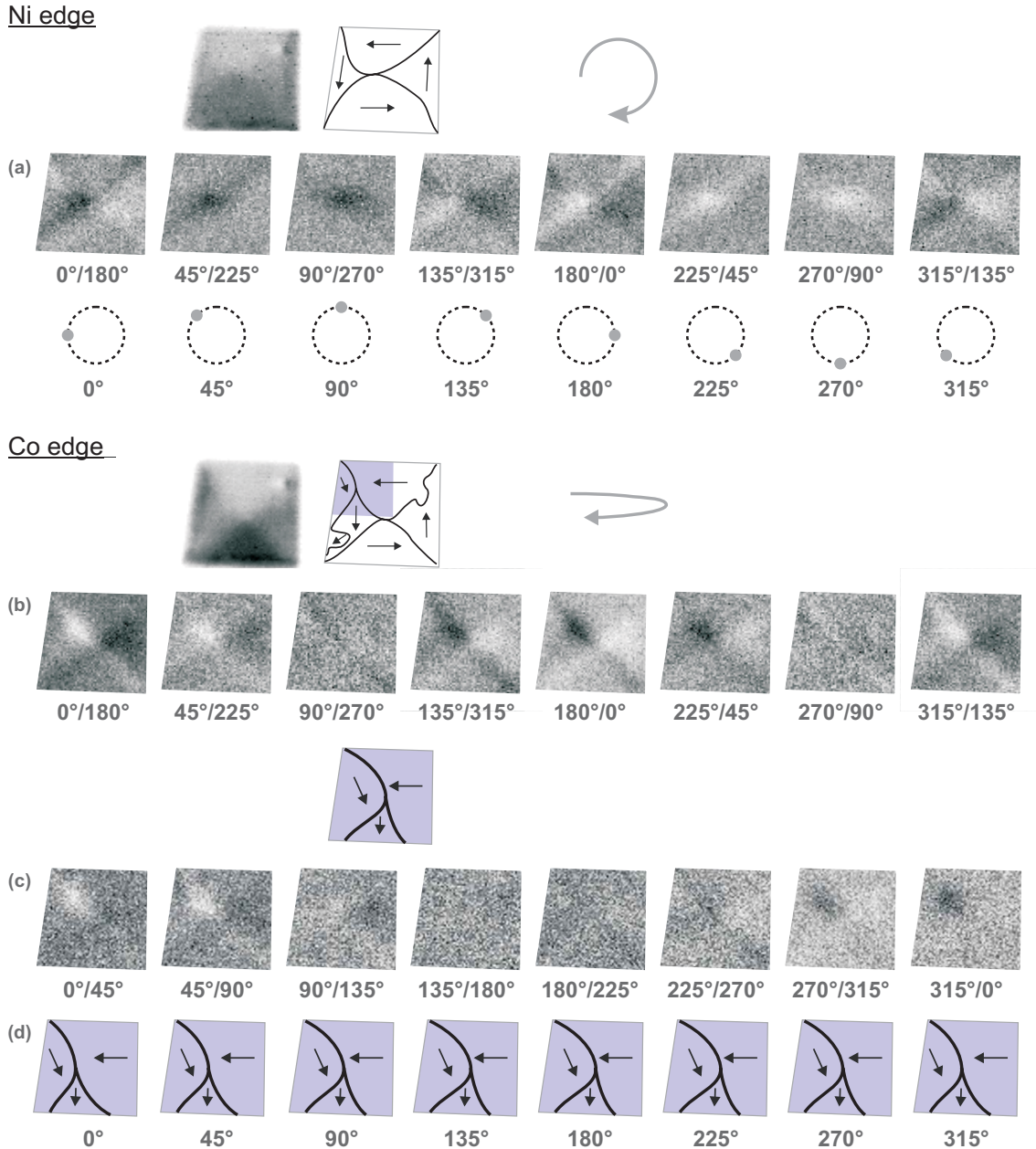


Figure 5.14: Dynamic response of a $1.5\ \mu\text{m} \times 1.5\ \mu\text{m}$ trilayer system, composed of Permalloy(20 nm)/Cu(5 nm)/Co(20 nm) ($H_0 = 630\ \text{A/m}$, $f = 187.5\ \text{MHz}$). The images were recorded at the L_3 absorption edges of Ni (852.7 eV) and Co (778.1 eV), and the differential images are shown at both edges (row (a) & (b)). The corresponding vortex core position is depicted for the Permalloy layer. The response in the upper left corner is enlarged for the Co layer and schematically shown in the lowest row (row (d)). The corresponding differential images composed by images of the upper left corner at consecutive phases, is shown as well for the Co layer (row (c)).

90°/270° (row (a) & (b)). The gyrotropic motion in the Permalloy layer is clearly observed in the dark dot representing the vortex structure moving upward, but no dynamic contrast can be detected around the core region in the Co layer.

The highest contrast appears around the upper left domain wall at the intersection with the additional domain. In an attempt to understand the differential contrast, a differential sequence was composed from images at consecutive phases with respect to the alternating field, around the upper left domain (row (c)). The highest contrast is again found at the upper left corner. The white contrast reflects a consecutive growth of the small domain to the right until it is at phase 135° , where there is no contrast anymore between phase 135° and 180° (row (d)). Starting from phase 225° , a dark contrast can be observed, indicating a shrinking of the domain to the left.

- The growing and shrinking of the small domain occurs in phase with the vortex core motion in the Permalloy layer, which is illustrated by the “circular” arrows on top of the series of differential images at the two edges, respectively. The position of the vortex core in both layers can also be compared by overlaying the Permalloy structure over the Co structure at every phase. The vortex core in the Permalloy structure is then found to be exactly situated at the upper left domain wall of the Co structure. In addition, the magnetization in the upper left domain (pointing right-bottom) has an antiparallel component, compared to the magnetization in the upper domain (pointing left). To avoid the excess in exchange energy, the magnetization will turn out of the plane at the domain wall. It is thus not improbable that the coupling between the stray field of this substructure and the stray field of the vortex core in the Permalloy structure, is causing the different in-phase motions in both layers.

It is important to note that these results were in general not reproducible in other samples, as the magnetic configuration in the different layers alters easily (cf. Paragraph 4.1.4). The dynamics response was more complicated for a great part of the investigated stacks.

5.4 NON-LINEAR RESPONSE OF MAGNETIC VORTEX STRUCTURES

The gyrotropic motion was imaged in Section 5.2 for magnetic thin film structures containing a single vortex. A fairly linear response was found between the extent of the gyrotropic motion, which is proportional to the vortex core velocity, and the amplitude of the externally applied alternating magnetic field. This is however only the case at very low field amplitudes ($< \pm 300$ A/m for the structure illustrated in Figure 5.7). The dynamic behaviour changes drastically at slightly higher field amplitudes, but still relatively low (maximum applied field amplitudes of about 1750 A/m $\hat{=} 2.2$ mT), where non-linear effects occur like the re-

versal of the out-of-plane vortex core magnetization. The reversal at such low field amplitudes is unexpected as large static fields in the order of 4 MA/m were needed and expected in the past [32, 26, 33]. In the following paragraphs, a multitude of such non-linear behaviour will be illustrated together with the appearance of hysteresis phenomena.

5.4.1 Vortex core reversal by sine excitation

In-plane magnetization configuration

Initially, the gyrotropic motion was imaged for a $1.5 \mu\text{m} \times 1.5 \mu\text{m}$, 50 nm thick Permalloy square (Figure 5.15). The structure was excited by an in-plane alternating magnetic field with a field amplitude H_0 of 1095 A/m. The frequency f of the externally applied field was set to 250 MHz and the sample was tilted over 30° with respect to the plane perpendicular to the incoming photon beam. In the first row of Figure 5.15, the direct in-plane contrast is shown, and the differential images are shown in the second row. A clockwise motion can be deduced for the moving vortex structure, using look-up table I (Figure 5.1).

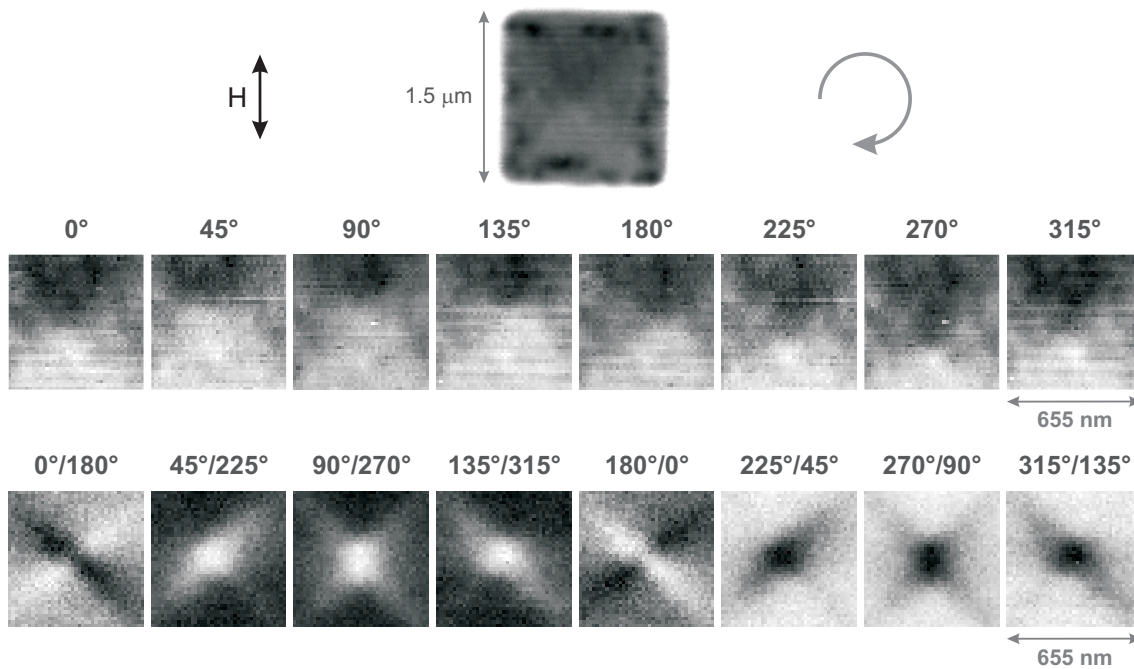


Figure 5.15: Dynamic response for a $1.5 \mu\text{m} \times 1.5 \mu\text{m}$, 50 nm thick vortex structure, excited by a continuous alternating magnetic field – low power state. The static in-plane configuration of the Landau pattern is depicted on top of the figure. The upper row shows the in-plane contrast of the vortex structure at eight different phases with respect to the external field ($H_0 = 1095 \text{ A/m}$, $f = 250 \text{ MHz}$). The corresponding differential images are depicted in the lower row.

Thereafter the field amplitude on the same sample was increased to 1225 A/m, keeping all other parameters fixed. The resulting gyrotropic motion was recorded and is depicted in Figure 5.16. The change in sense of gyration of the vortex structure can immediately be noticed in the sequence of differential images as well as in the direct in-plane magnetic contrast (but less clearly). As mentioned in Paragraph 2.3.1, the sense of gyration is only determined by the direction of the out-of-plane vortex core magnetization. Apparently, a change in field amplitude of the in-plane alternating magnetic field is thus capable of changing the direction of the out-of-plane core magnetization. Reducing the field amplitude H_0 back to 1095 A/m, again reverses the direction of the core magnetization.

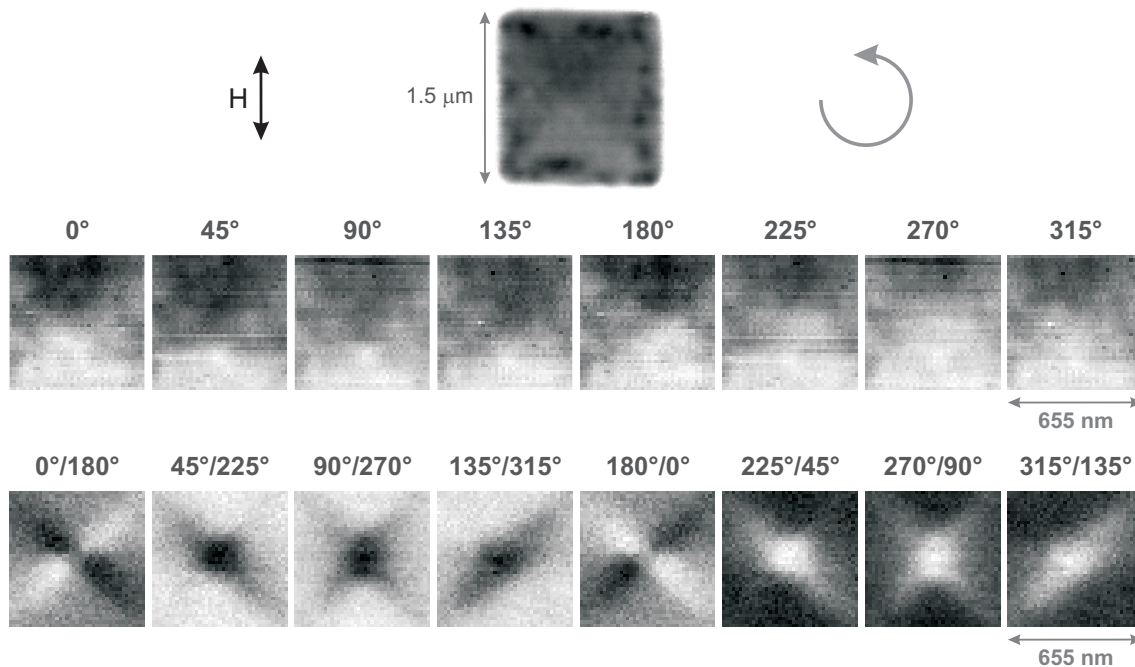


Figure 5.16: Dynamic response for a $1.5 \mu\text{m} \times 1.5 \mu\text{m}$, 50 nm thick vortex structure, excited by a continuous alternating magnetic field – high power state. The static in-plane configuration of the Landau pattern is depicted on top of the figure. The upper row shows the in-plane contrast of the vortex structure at eight different phases with respect to the external field ($H_0 = 1225 \text{ A/m}$, $f = 250 \text{ MHz}$). The corresponding differential images are depicted in the lower row.

The sequence of differential images at both field amplitudes can now be compared. Interestingly enough the differential contrasts for a left/right motion, at $0^\circ/180^\circ$ and $180^\circ/0^\circ$, are the same. If the trajectories for both cases would be overlaid over one another, this would result in an “intersection” when the core is situated left and right at a certain phase with respect to the exciting field, here at the phases 0° and 180° , respectively. This is illustrated in Figure 5.17 where the red circle represents the trajectory at low field amplitude (cf. the case in Figure 5.15), and the blue circle corresponds to the trajectory at high field amplitude

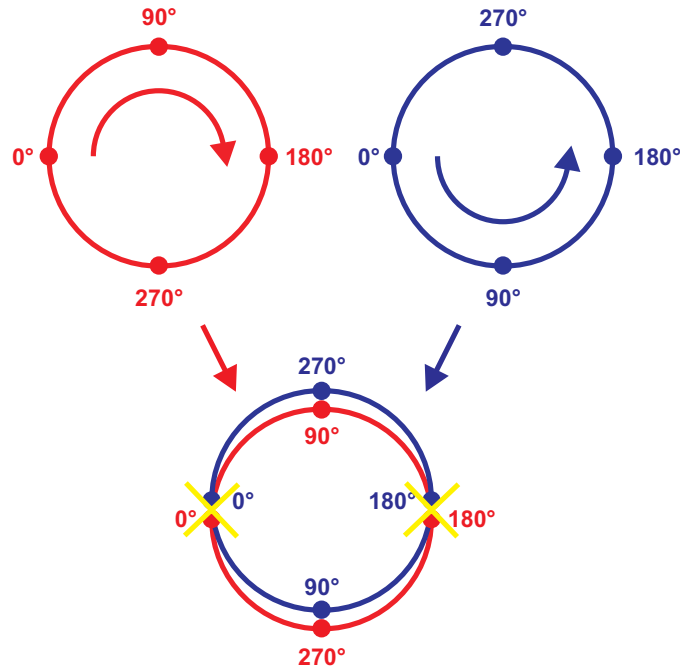


Figure 5.17: Illustration of the trajectories of a vortex structure, before (red) and after (blue) the reversal process. The dots indicate the position of the vortex core with respect to the phase of the external field. The lower panel shows how both trajectories intersect one another at the yellow crosses.

(cf. the case in Figure 5.16). The dots indicate the positions of the vortex core at the corresponding phases of the external field (0° , 90° , 180° and 270°). Both “trajectories” are overlaid over one another in the lower panel of Figure 5.17. The yellow crosses indicate the positions where the trajectories intersect one another. In this case, this occurs for the vortex structure moving left and right, corresponding to the phases 0° and 180° . As both trajectories are “coinciding”, no distinction can be observed in the corresponding differential images ($0^\circ/180^\circ$ and $180^\circ/0^\circ$). On the other hand, at phase 90° (and similar at phase 270°), the core positions at both field amplitudes are opposite (up for the red trajectory and down for the blue trajectory). The difference in positions of the vortex core for both field amplitudes is thus most pronounced for the pure up/down motion which, translated to differential images, corresponds to the cases $90^\circ/270^\circ$ and $270^\circ/90^\circ$, respectively. The vortex core reversal can therefore only be observed in the dots.

This conclusion is closely related to the exciting magnetic field, as the gyrotropic motion is following the applied alternating magnetic field. A straight horizontal stripline was used here, so the field is oscillating in the vertical direction (depicted by the double-arrow with the notation \mathbf{H} in Figures 5.15 & 5.16). The reversal will in case of a stripline directed vertically (hairneedle-shaped stripline), only be

observed in the crosses, as now the vortex core will “coincide” at the upper and lower position in the vortex gyration if the trajectories for both core directions would be overlaid. This can also be understood by rotating Figure 5.17 over 90 degrees.

This behaviour is illustrated in Figure 5.18 for a $1.5\ \mu\text{m} \times 1.5\ \mu\text{m}$, 40 nm thick Permalloy square. The element was excited with an alternating magnetic field. The frequency f of the exciting field was set to 187.5 MHz, and the switching was deduced from the change in sense of gyration when the field amplitude H_0 was changed from 315 A/m to 355 A/m. By comparing the sequence of differential images at both field amplitudes, only a change can be observed in the crosses at $0^\circ/180^\circ$ and $180^\circ/0^\circ$. The differential contrast for an up/down motion, at $90^\circ/270^\circ$ and $270^\circ/90^\circ$, is as expected the same.

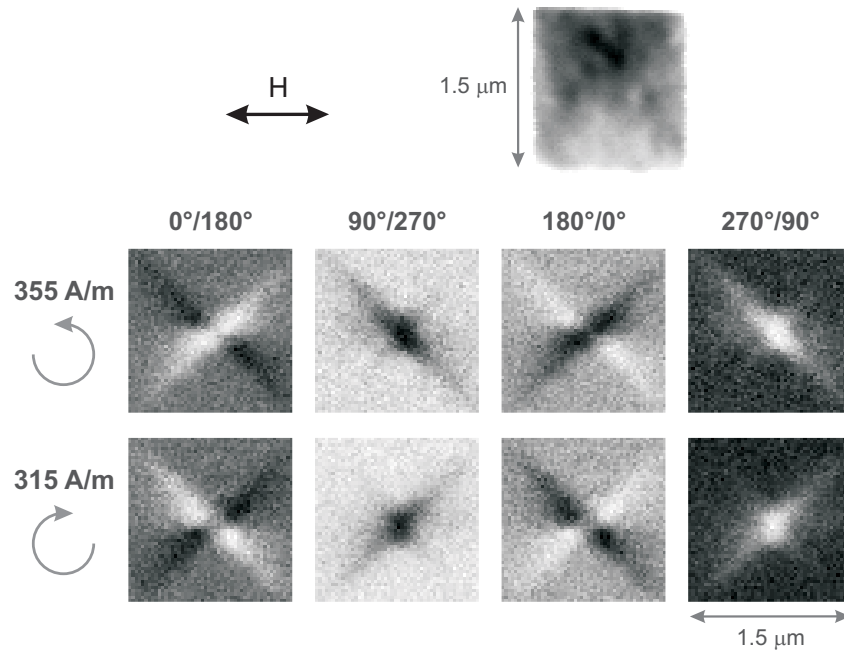


Figure 5.18: Dynamic response for a $1.5\ \mu\text{m} \times 1.5\ \mu\text{m}$, 40 nm thick vortex structure, excited by a continuous alternating magnetic field – hairneedle-shaped stripline. The static in-plane configuration of the Landau pattern is depicted on top of the figure. The lower row shows the differential contrast of the vortex structure at four different phases with respect to the external field for a lower field amplitude. The upper row shows the differential images at higher field amplitude ($f = 187.5\ \text{MHz}$).

Out-of-plane magnetization configuration

The vortex core reversal was also imaged for a $500\ \text{nm} \times 500\ \text{nm}$, 40 nm thick Permalloy square and is depicted in Figure 5.19. The sample was placed perpendicular with respect to the incoming photon beam so the out-of-plane component

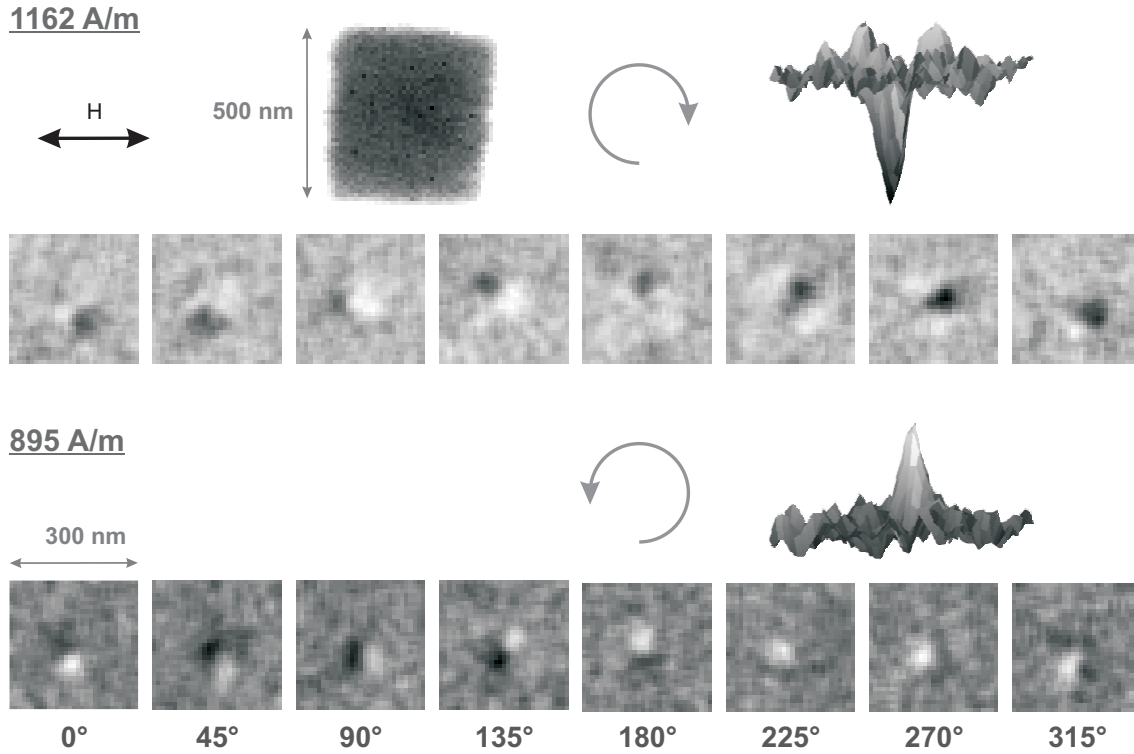


Figure 5.19: Dynamic response for a $500 \text{ nm} \times 500 \text{ nm}$, 40 nm thick vortex structure, excited by a continuous alternating magnetic field ($f = 437.5 \text{ MHz}$). The “averaged” out-of-plane magnetic contrast $\Gamma_i^{-/+}(\text{direct})$ is depicted at eight different phases with respect to the external field for a lower field amplitude (lower row) and higher field amplitude (upper row), respectively. A surface plot is added for the “average” contrast at phase 270° for both field amplitudes.

of the magnetization was imaged. The frequency f of the alternating magnetic field was set to 437.5 MHz . At a lower field amplitude of the exciting field of 895 A/m (lower row), a counterclockwise motion can be deduced for the vortex gyration by following the white dots in the direct “averaged” images $\Gamma_i^{-/+}(\text{direct})$ (with $i = 1, \dots, 8$ corresponding to the eight different phases with respect to the alternating magnetic field, see below). Increasing the field amplitude up to 1162 A/m does not only change the contrast of the out-of-plane component of the magnetization at the centre, but modifies also the sense of gyration to a clockwise motion (upper row).

This result confirms the dependence of the sense of gyration of the vortex structure on the direction of the out-of-plane core magnetization. The external field oscillates horizontally as a hairneedle-shaped stripline was used here. Following both core positions at the respective field amplitudes, at every phase, resumes to the conclusion that the vortex core coincides for the up and down position. The reversal is thus detected in the left/right position of the core, as was observed in Figure 5.18.

A slightly different approach was adopted here for the analyses of the direct “averaged” images. Two sequences of images were recorded for different circular polarization of the photons (Γ_i^- and Γ_i^+ , respectively). The corresponding differential images $\Gamma_i^{-/+}$ were deduced, using relation (5.4), improving by this the signal-to-noise-ratio and removing all non-magnetic contributions. An average image $\Gamma_{mean}^{-/+}$ was subsequently deduced from $\Gamma_i^{-/+}$ at the eight different phases:

$$\Gamma_{mean}^{-/+} = \frac{1}{8} \sum_{i=1}^8 \Gamma_i^{-/+}. \quad (5.5)$$

All separate images $\Gamma_i^{-/+}$ were thereafter divided by the average image $\Gamma_{mean}^{-/+}$:

$$\Gamma_i^{-/+(direct)} = \frac{\Gamma_i^{-/+}}{\Gamma_{mean}^{-/+}}. \quad (5.6)$$

This approach reveals the out-of-plane core magnetization so the vortex gyration can be followed adequately. The adopted method again introduces artefacts of opposite contrast with respect to the vortex core magnetization, similar to the procedure used in Figure 5.9. The use of $\Gamma_i^{-/+}$ also implies the consecutive recording of two sequences of images. Misalignments and drifts are most likely to appear, causing a smearing out of the vortex core region in the images $\Gamma_i^{-/+}$. Stable measurement conditions are thus a prerequisite for a successful analysis of the data, which is needed for example for the results presented in Paragraph 5.4.6.

5.4.2 Hysteresis behaviour I: multiple levels

In the previous paragraph, two stable levels could be tracked each time. At a certain amplitude of the alternating magnetic field, the vortex structure will move in a certain sense, but the change of the field amplitude will cause the vortex structure to move in the opposite sense. A more complicated reversal scheme is presented here.

- The gyrotropic motion was investigated for a $1.5 \mu\text{m} \times 1.5 \mu\text{m}$, 50 nm thick Permalloy square. An in-plane alternating magnetic field was applied. The frequency f remained fixed at 250 MHz and only the field amplitude H_0 was varied. A straight horizontal stripline was used so the reversal process is observed by looking at the dots in the differential contrast. The main results are depicted in Figure 5.20, and the arrows show which field amplitude jumps have to be performed to reach the different levels.

Initially, the amplitude was set to 1140 A/m. A dark dot could be observed and indicates a clockwise motion of the vortex structure (identical to the case in

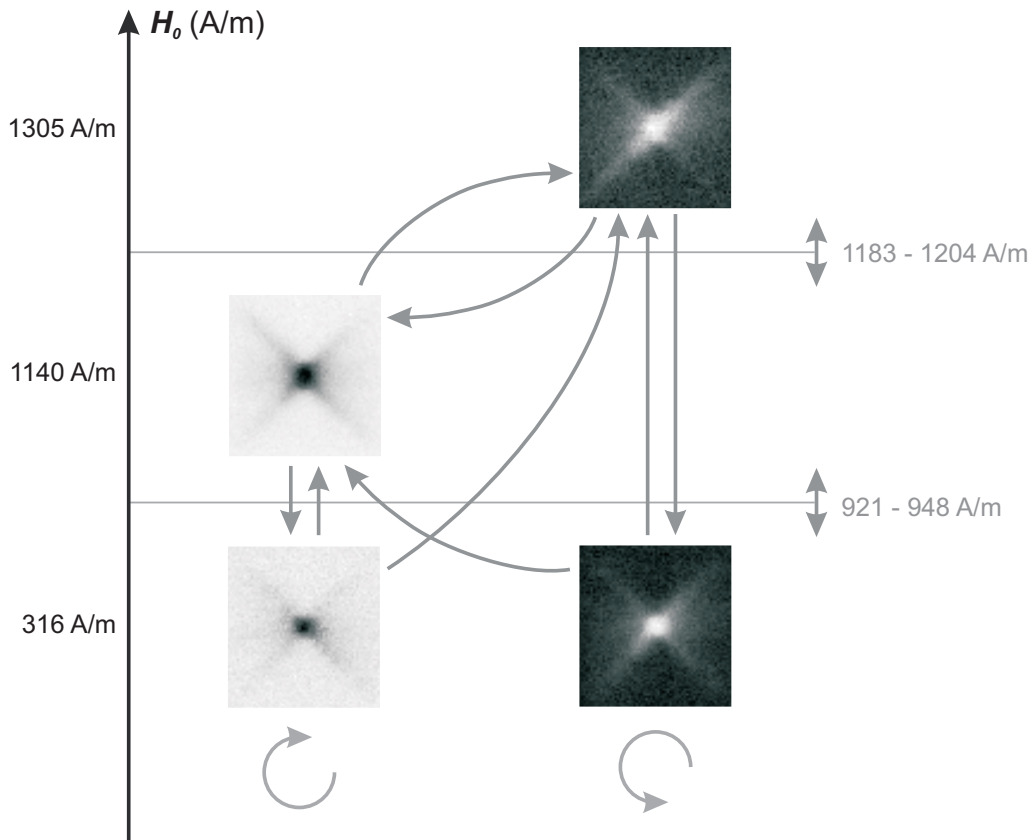


Figure 5.20: Hysteresis behaviour for a $1.5 \mu\text{m} \times 1.5 \mu\text{m}$, 50 nm thick Permalloy element. The images represent the differential contrast at a certain fixed phase with respect to the exciting field ($f = 250 \text{ MHz}$). The arrows constitute the scheme for the reversal of the direction of the out-of-plane core magnetization. The sense of gyration of the vortex structure is indicated by the circular arrows below.

Figure 5.15). The field amplitude was then increased in a single step to 1305 A/m, and a white dot could then be observed in the differential contrast. This indicates a change in sense of gyration of the vortex structure (identical to the case of Figure 5.16), and thus a change in the direction of the out-of-plane vortex core magnetization. Reverting the field amplitude to a value of 1140 A/m brought the gyration sense also back to the initial one. Two stable levels are thus present. Starting now from the initial level at a field amplitude of 1140 A/m and making a jump towards a lower field amplitude, here 316 A/m, resulted in a dark dot in the observed differential contrast, so the sense of gyration remained unchanged. The contrast changes again when the field amplitude is increased to 1305 A/m, so a reversal process has occurred. Jumping back now from the highest level to an amplitude of 316 A/m, resulted in a bright dot in the differential contrast. The direction of the out-of-plane core magnetization is thus kept from the higher level. This hysteresis behaviour was repeated numerous times and all levels behaved in a stable way following the scheme of Figure 5.20. The thresholds of

the different levels were also investigated. They lie around 921–948 A/m and 1183–1204 A/m, respectively.

- The same behaviour was also observed in other samples, as demonstrated in Figure 5.21 for a $1.5\ \mu\text{m} \times 1.5\ \mu\text{m}$, 50 nm thick Permalloy square with an asymmetric edge. The stripline was also orientated horizontally so the reversal process is again observed in the dots. The element was excited with an in-plane alternating field with a frequency f of 250 MHz. The different levels were recorded and the threshold values were also investigated, resulting in higher values than for the symmetric $1.5\ \mu\text{m} \times 1.5\ \mu\text{m} \times 50\ \text{nm}$ Permalloy square. Nevertheless the scheme, indicated by the arrows, could be meticulously reproduced.

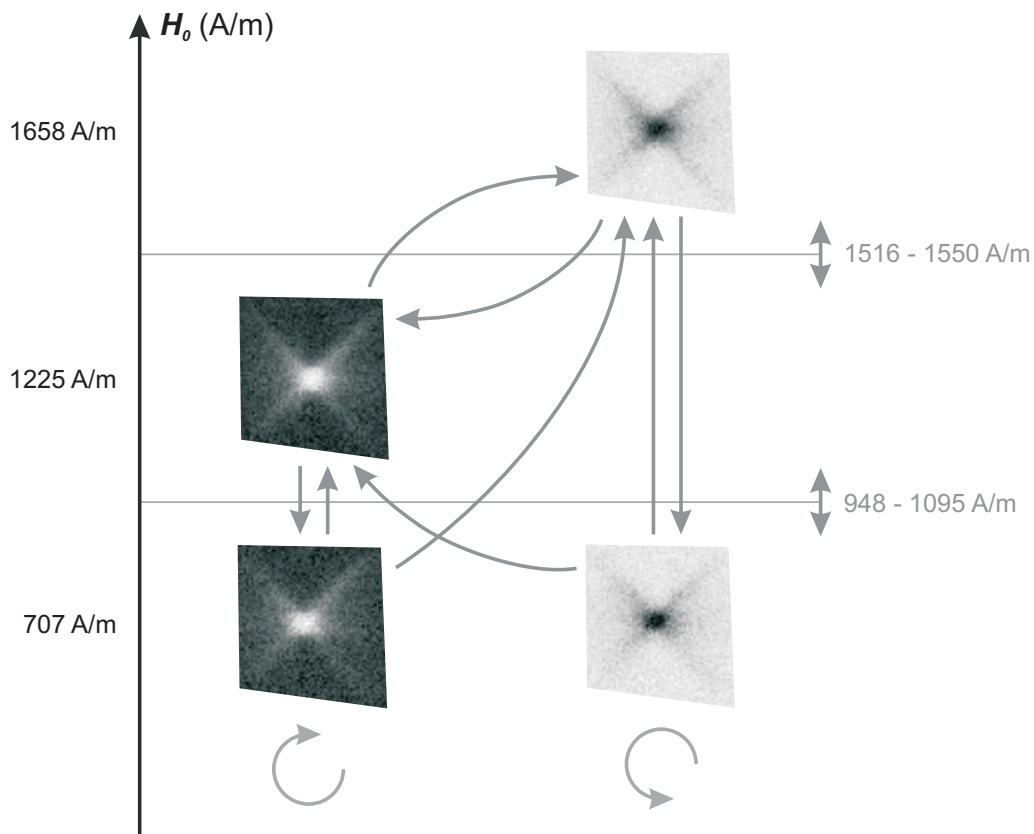


Figure 5.21: Hysteresis behaviour for a $1.5\ \mu\text{m} \times 1.5\ \mu\text{m}$, 50 nm thick Permalloy element with asymmetric edge. The images represent the differential contrast at a certain fixed phase with respect to the exciting field ($f = 250\ \text{MHz}$). The arrows constitute the scheme for the reversal of the direction of the out-of-plane core magnetization. The sense of gyration of the vortex structure is indicated by the circular arrows below.

5.4.3 Vortex core reversal by burst excitation

The reversal scheme, introduced in the previous paragraph, is the result of a thorough field amplitude scan. In order to not discard or miss any level, the ampli-

tude steps have to be chosen small enough (typically 1 mW steps $\hat{=} 20\text{--}90\text{ A/m}$), and multiple scans have to be performed. A simple increase and decrease of the field amplitude will only reveal part of the levels. Larger jumps need to be performed as well to reveal some “hidden” levels. For example the lower threshold in Figure 5.20 can only be estimated once the highest level is found and a jump is made to the lowest level. An increase of the field amplitude in small steps will then reveal the lower threshold. In this paragraph, another reversal scheme will be presented based on the knowledge attained formerly.

In-plane magnetization configuration

The gyrotropic motion was imaged for the same $1.5\ \mu\text{m} \times 1.5\ \mu\text{m}$, 50 nm thick Permalloy square as presented in the reversal scheme, shown in Figure 5.20. The frequency f was kept at 250 MHz and the field amplitude H_0 was chosen low enough, here 835 A/m, so it was situated in the region where both senses of gyration are possible (cf. Figure 5.20). Initially, the vortex structure gyrates clockwise, as shown in Figure 5.22. Jumps to higher field amplitudes and back, as performed in Paragraph 5.4.2, are capable to reverse the out-of-plane core magnetization. The idea is now to induce these jumps much faster than it is if the field amplitude

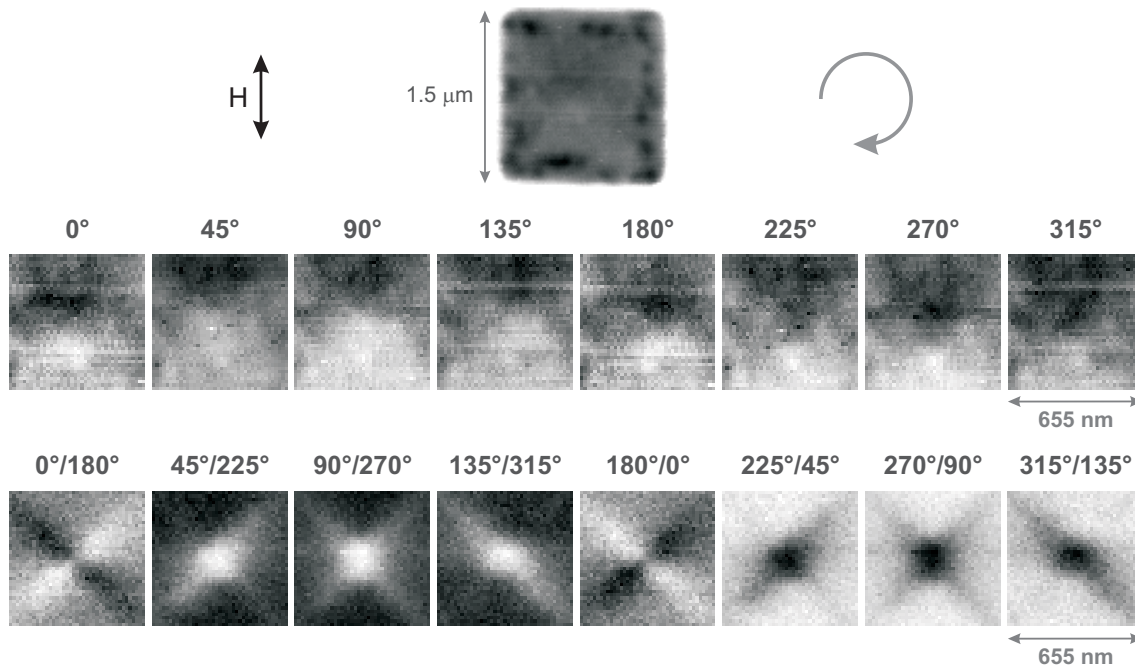


Figure 5.22: Dynamic response for a $1.5\ \mu\text{m} \times 1.5\ \mu\text{m}$, 50 nm thick vortex structure, excited by a continuous alternating magnetic field – before burst excitation. The static in-plane configuration of the Landau pattern is depicted on top of the figure. The upper row shows the in-plane contrast of the vortex structure at eight different phases with respect to the external field ($H_0 = 835\text{ A/m}$, $f = 250\text{ MHz}$). The corresponding differential images are depicted in the lower row.

would be changed manually, like in previous paragraphs. A short burst of the excitation field was thus applied. The amplitude of the burst has been varied up to a maximum value of about 1500 A/m, and the length of the burst was extended up to four periods of the exciting magnetic field (~ 16 ns). The response of the structure after a burst excitation, with a duration of two periods and a burst amplitude of about 1400 A/m, is shown in Figure 5.23. The change in sense of gyration can easily be observed in the differential images as well as in the in-plane magnetic contrast of the vortex structure, although less clearly. This indicates a reversal of the out-of-plane vortex core magnetization. An additional burst brought the sense of gyration back to the initial state. The direction of the out-of-plane vortex core magnetization can thus be reversed back and forth with consecutive bursts of the alternating field. At the maximum used field amplitude, a single period burst of the alternating magnetic field was sufficient to reverse the direction of the vortex core magnetization. At 250 MHz, this involves a duration of the burst of 4 ns.

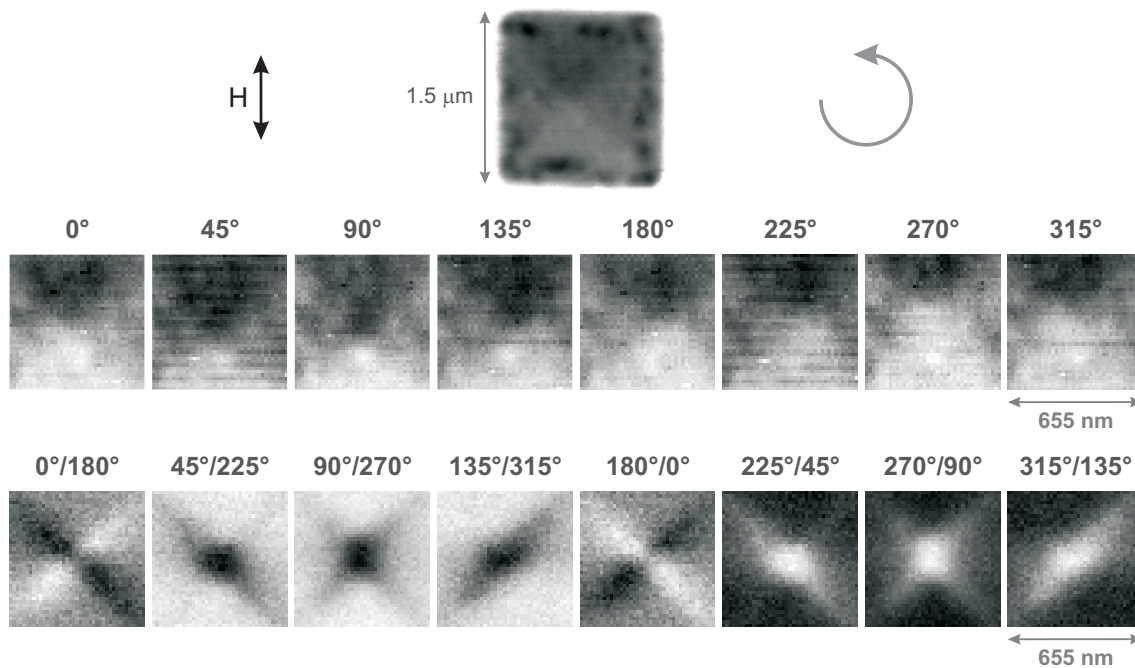


Figure 5.23: Dynamic response for a $1.5 \mu\text{m} \times 1.5 \mu\text{m}$, 50 nm thick vortex structure, excited by a continuous alternating magnetic field – after burst excitation. The static in-plane configuration of the Landau pattern is depicted on top of the figure. The upper row shows the in-plane contrast of the vortex structure at eight different phases with respect to the external field ($H_0 = 835$ A/m, $f = 250$ MHz). The corresponding differential images are depicted in the lower row.

The different levels, as observed in previous paragraph, seem to no longer play a significant role. Only a large enough field amplitude for the burst appears to be necessary to cause a reversal. Nevertheless the switching probabilities

were different starting from both core polarization, which in turn might again be related to the existence of the different levels. The burst has to reach one of the two upper levels in order to switch the core polarization. The probability to reach one of these two levels will of course be different for a fixed amplitude of the burst amplitude.

The in-plane magnetic contrast was visualized here, and the reversal process can thus only be observed in a change in sense of gyration. Therefore, a small in-plane alternating magnetic field is necessary to induce the gyrotropic motion of the vortex structure. This background field would no longer be necessary when the out-of-plane core magnetization is imaged directly. The core switching could then be observed immediately (cf. Section 4.2) without investigating the sense of gyration. Nevertheless, the resonant excitation appears to be primordial for the vortex core reversal. Indeed, no switching could be detected for a couple of periods of an alternating magnetic field without background excitation.

Out-of-plane magnetization configuration

The vortex motion was also recorded for a $500 \text{ nm} \times 500 \text{ nm}$, 40 nm thick Permalloy square. The sample was placed perpendicular with respect to the incoming photon beam so the out-of-plane component of the magnetization was imaged. The amplitude of the exciting magnetic field was set to 587 A/m , and a higher frequency of 437.5 MHz was used. The reversal of the direction of the out-of-plane vortex core magnetization was carried out with a burst of two periods ($\sim 4.6 \text{ ns}$) of the alternating magnetic field. The amplitude of the burst was about 2830 A/m . Two sequences of images were recorded before and after the application of the burst (upper and lower row of Figure 5.24, respectively). A dark spot indicates a vortex core moving clockwise before the application of a burst. The contrast changes after application of the burst, as well as the gyration sense. The procedure described by the Eqs. (5.2) & (5.3), was used to deduce the images shown in Figure 5.24. The position of the vortex core, at the different phases with respect to the alternating magnetic field, was extracted. A large discrepancy can be noticed in the extent of the gyrotropic vortex motion for the two cases, which will further be discussed in Paragraph 5.4.6.

The vortex core velocity was also deduced during these measurements. For this purpose, an ellipse was fit through the vortex core position at the eight phases and the circumference was found using the relation [98]:

$$O = \pi \left(1.5(a + b) - \sqrt{ab} \right), \quad (5.7)$$

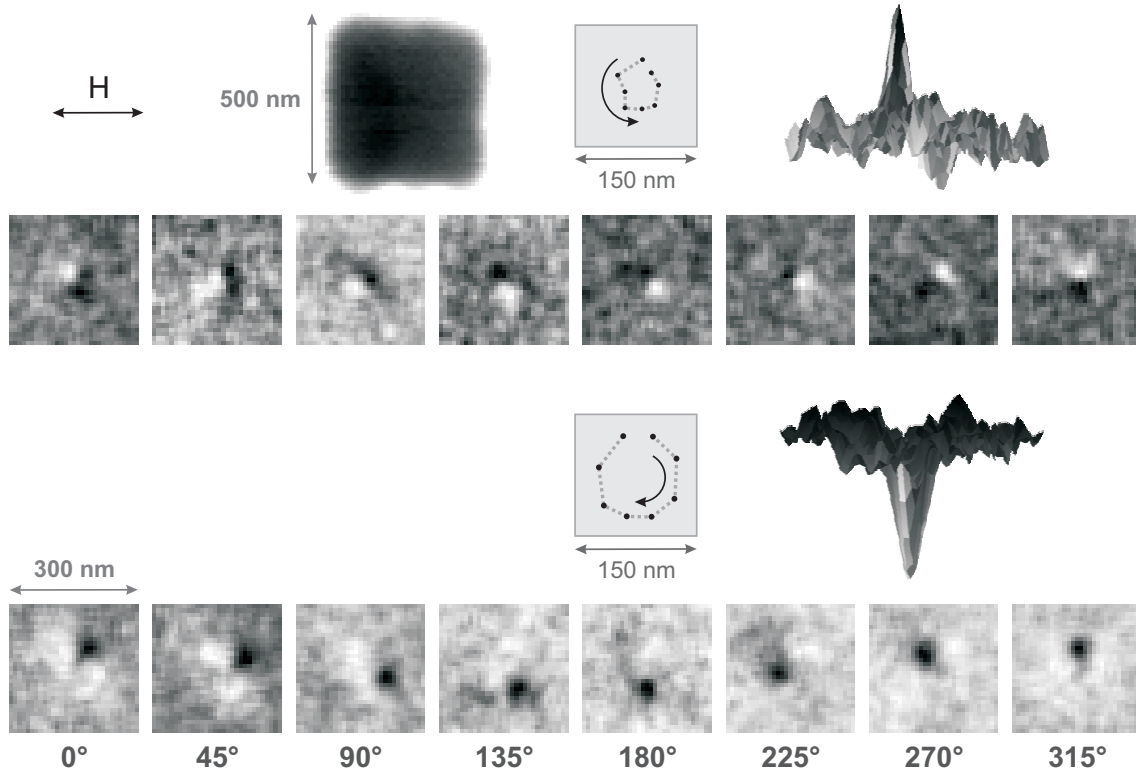


Figure 5.24: Dynamic response for a $500 \text{ nm} \times 500 \text{ nm}$, 40 nm thick vortex structure, excited by a continuous alternating magnetic field ($H_0 = 587 \text{ A/m}$, $f = 437.5 \text{ MHz}$). The “averaged” out-of-plane magnetic contrast Γ_i^{direct} is depicted at eight different phases with respect to the external field before (upper row) and after (lower row) the application of a burst, respectively. The position at the different phases is depicted in the insets, together with the “average” out-of-plane contrast at phase 270° .

with a and b being the major and minor radius, respectively. The vortex core velocity is then simply calculated by taking into account the driving frequency of the gyrotropic motion, which is the frequency of the externally applied field, here 437.5 MHz . An average vortex core velocity was then found of about 140 m/s for the vortex core pointing up, while a much smaller speed of 82 m/s was calculated when the vortex core is pointing down.

5.4.4 Vortex core reversal – mechanism

The reversal of the out-of-plane vortex core magnetization was already investigated using a static, perpendicular field. Large field amplitudes of about 4 MA/m were needed therefore and the mechanism which could be observed in micromagnetic simulations, is the nucleation of a Bloch point² at one side of

²A Bloch point is a singularity of the directional magnetization distribution. At this point, no direction of the magnetization can be assigned. Any direction of the magnetization is thus present in the close vicinity of a Bloch point.

the surface which is running across the thin film layer to the other side [33]. In the present experiments, small in-plane field amplitudes in the range of only 400 A/m were already able to reverse the core magnetization. The same brute force mechanism is thus rather inconceivable here.

In order to find a reversal mechanism, involving only small magnetic field amplitudes, micromagnetic simulations were performed with the OOMMF programme (cf. Paragraph 2.3.2) for a Permalloy structure with a single vortex as groundstate configuration. The mechanism which could be deduced from these simulations is the consecutive creation and annihilation of a vortex-antivortex pair. This is illustrated for a $500 \text{ nm} \times 500 \text{ nm} \times 40 \text{ nm}$ Permalloy square in Figure 5.25. The damping constant α was set to 0.05 and the square-structure was subdivided into small cells with a size of $2 \text{ nm} \times 2 \text{ nm} \times 40 \text{ nm}$. Standard

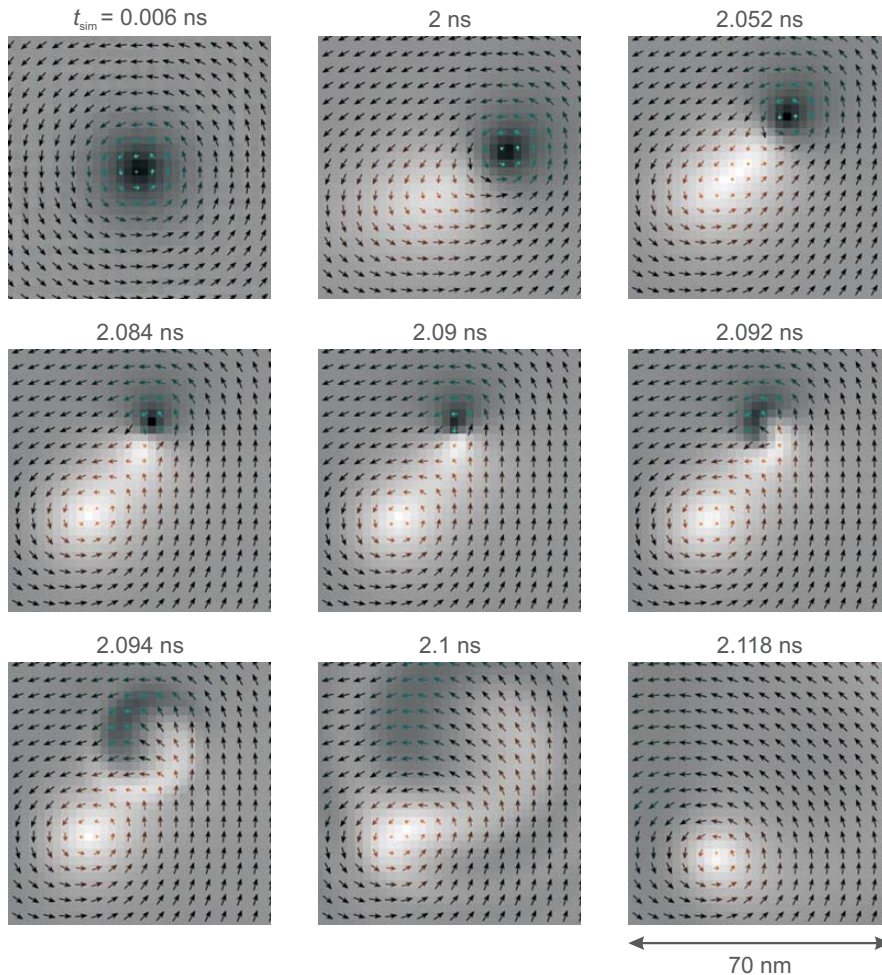


Figure 5.25: Snapshots at the corresponding simulation time t_{sim} of the reversal mechanism in a $500 \text{ nm} \times 500 \text{ nm}$, 40 nm thick vortex structure, excited by a continuous alternating magnetic field (black = negative component; white = positive component; the arrows indicate the in-plane distribution of the magnetization).

material parameters were used for Permalloy with $M_s = 8.6 \times 10^5$ A/m as the saturation magnetization and $A = 1.3 \times 10^{-11}$ J/m as the exchange constant. The magnetocrystalline anisotropy was neglected. The element was excited with an alternating magnetic field along the vertical direction, with an amplitude of 4000 A/m and the frequency f was set to 548 MHz, corresponding to the resonance frequency of the structure. The grayscale contrast is proportional to the out-of-plane magnetization component (black = negative; white = positive), and the arrows indicate the in-plane distribution of the magnetization.

The snapshots in Figure 5.25 show the region around the core ($70 \text{ nm} \times 70 \text{ nm}$ cut). The vortex core is originally down and starts gyrating under influence of the applied in-plane field (0.006 ns). The dynamic motion causes a deformation of the vortex core with an opposite direction of the magnetization with respect to the original core (2 ns). The deformed area is elongated in the direction towards the centre of the structure. It increases until its magnetization is pointing fully out of the plane³ (2.052 ns). The deformed area evolves then in a vortex-antivortex pair (2.084 ns). The antivortex moves towards the original vortex (2.09 ns), and eventually annihilates with the original vortex. The sudden annihilation process is accompanied by spin waves so that the energy concentrated in the cores quickly dissipates into the entire element (2.092–2.1 ns). A vortex structure with opposite magnetization direction remains (2.118 ns).

This reversal mechanism was not only observed when using a continuous sine excitation with high enough field amplitude but was also reported when the structure is excited with a fast pulse [99, 100] or a single burst of an alternating magnetic field [101]. This illustrates the general validity of the mechanism.

The simulation results presented in this thesis, were based on a 2D mesh. Nevertheless, the use of a 3D mesh resulted in the same mechanism, indicating the validity of the mechanism. On the other hand, the correctness is still arguable as in the continuum limit, the topological charge p is conserved. The switching process thus violates the model used in micromagnetics, as angles between neighbouring spins appear up to 100° . The simulation times mentioned above are thus only a rough indication of how fast the switching process occurs but no exact value can be given based on micromagnetic simulations. In conclusion, the switching between states is only due to lattice discreteness.

³This is the nucleation site for the vortex-antivortex pair creation ☺

Simulations vs. experiments

The vortex core reversal by burst excitation, as described in Paragraph 5.4.3, was the only switching scheme which could be reproduced by micromagnetic simulations. This was not only performed on squares but also on circular-shaped patterns. Hereby, the amplitude and length of the burst need to be adjusted correctly in order to observe a single switch of the vortex core. The reversal mechanism itself, on the other hand, was not observed during the measurements. Only the sense of gyration (and the contrast of the core magnetization), before and after the application of the burst, could be observed in order to distinguish a reversal process.

The switching with fast, unipolar pulses was till now only observed in micromagnetic simulations but not experimentally. The highest field amplitudes which were applied until now during the experiments were around 8 kA/m with a rise time of about 100 ps and a pulse width of about 200 ps. Micromagnetic simulations suggest either to increase the field amplitude and/or to reduce the rise time of the magnetic field pulses. Nevertheless, one has to bear in mind that a field amplitude of 8 kA/m is already a factor of 20 higher than the lowest found switching threshold using a continuous alternating magnetic field (~ 400 A/m). At long last, even if larger field amplitudes would be capable to switch the vortex core, such large field amplitudes combined with a certain pulse length could alter the magnetization distribution and no single vortex structure would be present anymore.

On the other hand, the occurrence of specific levels as found in the Paragraphs 5.4.1 & 5.4.2, when excited with a continuous alternating magnetic field, could not be reproduced in the performed micromagnetic simulations. In the simulations, the excitation with a sine field with low enough field amplitude, simply induces the gyrotropic motion without any reversal process. A field amplitude threshold exists although, which is for the above discussed simulation around 2400 A/m. Above this field amplitude, the excitation will not cause a simple reversal process but multiple reversal processes. The direction of the vortex core magnetization can thus not be held fixed above this threshold and starts to flip back and forth. The time between the flips and back-flips depends on the field amplitude. Near the threshold, it may last about 40 ns, but at slightly higher field amplitudes much shorter times (about 5 ns) occur. A further increase in field amplitude will simply cause consecutive switching processes. Double and triple switches could hereby easily be observed in the simulations which last for

only a couple of hundred picoseconds. Experimentally, such a random switching behaviour would result in a loss of the differential contrast as both senses of gyration, for the core pointing up and down, respectively, would cancel one another out.

Thus, the main conclusion from micromagnetic simulations is that a threshold exists for the field amplitude above which uncontrollable switching processes occur. This threshold will differ from the type of in-plane excitation which is applied to the structure (pulsed, burst or continuous sine excitation), and is at least double as large as the switching field amplitudes observed experimentally for continuous sine excitation. Nevertheless, this threshold amplitude is still a factor of about 100 less than the switching fields needed with a static perpendicular field. Finally, a reversal scheme with a clear transition to uncontrollable switching is, based on the experimental observations, clearly not the final explanation. This will even be more emphasized in the results and discussion of the next three paragraphs.

5.4.5 Hysteresis behaviour II: circular structures

As noticed in previous paragraphs, different levels are present for the direction of the out-of-plane core magnetization in magnetic vortex structures, depending on the amplitude of the externally applied field. Each level possesses specific properties, as discussed in Paragraph 5.4.2. Until now, results were only presented for square-shaped samples where three distinct levels could be observed. Two stable levels were found at higher field amplitudes where the direction of the out-of-plane vortex core magnetization stays fixed and is pointing up and down, or vice versa. A simple change in field amplitude could then reverse the out-of-plane core magnetization between these two levels. A third level was also present at lower field amplitudes where both directions of the core magnetization could be obtained, depending on the field amplitude history.

Circular-shaped structures with a single vortex differ from square-shaped Landau patterns mainly by the absence of domain walls, influencing directly the magnetization dynamics (cf. Figure 5.33). In the following, the dynamic response was imaged for a Permalloy disk with a diameter of $2\ \mu\text{m}$ and a thickness of 50 nm, and is shown in Figure 5.26. The sample was excited with an in-plane alternating magnetic field and the frequency f was set to 250 MHz. The exciting field was induced using a horizontal stripline, so the reversal process can be observed in the dots when looking at the differential contrast. Consecutive

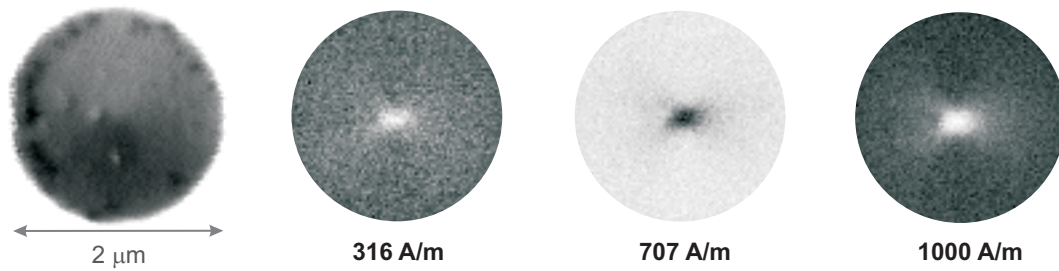


Figure 5.26: Dynamic response for a Permalloy disk with a diameter of $2\ \mu\text{m}$ and a thickness of $50\ \text{nm}$, excited by a continuous alternating magnetic field – multiple levels. The in-plane magnetic contrast is shown on the left side. The differential contrast is depicted at three different field amplitudes at one phase with respect to the external field ($f = 250\ \text{MHz}$).

scans were performed by increasing and decreasing gradually, in small steps, the external field amplitude. The differential contrast varies, for increasing and decreasing field amplitudes, from a white dot to a black dot to a white dot again. The sense of gyration could be determined from additional measurements at intermediate phases of the externally applied field. A white dot is indicating a vortex structure moving counterclockwise, while a black dot corresponds to a clockwise motion (not shown). Three stable levels are clearly present instead of the two, found in square-shaped structures (cf. Paragraphs 5.4.1 & 5.4.2). A level where both directions of the core magnetization can be present, was on the other hand not found.

The field amplitude thresholds were thereafter investigated for the same disk and are shown in Figure 5.27. The differential contrast was investigated near the thresholds at the different switching levels for a step-wise increase and decrease of the field amplitude in the left and right block, respectively. For increasing field amplitudes, shown by the differential images in the red area, a first reversal occurs around $590\ \text{A/m}$ (from a white to a black dot) and a second reversal was observed around $758\ \text{A/m}$ (from a black to a white dot). The blue area indicates the differential images for decreasing field amplitudes. The corresponding reversal processes occur now around $560\ \text{A/m}$ and $775\ \text{A/m}$, respectively. The second level, represented by a dark dot in the differential contrast (in the gray area), is thus broader for decreasing field amplitudes. In addition, in the upper row at $585\ \text{A/m}$, the differential contrast vanishes completely. This indicates that the out-of-plane vortex core magnetization is continuously switching back and forth. These consecutive reversal processes are not synchronized so the adopted stroboscopic imaging technique averages out all dynamic magnetic contributions. It is also important to note that the thresholds are extremely sharp. A small change

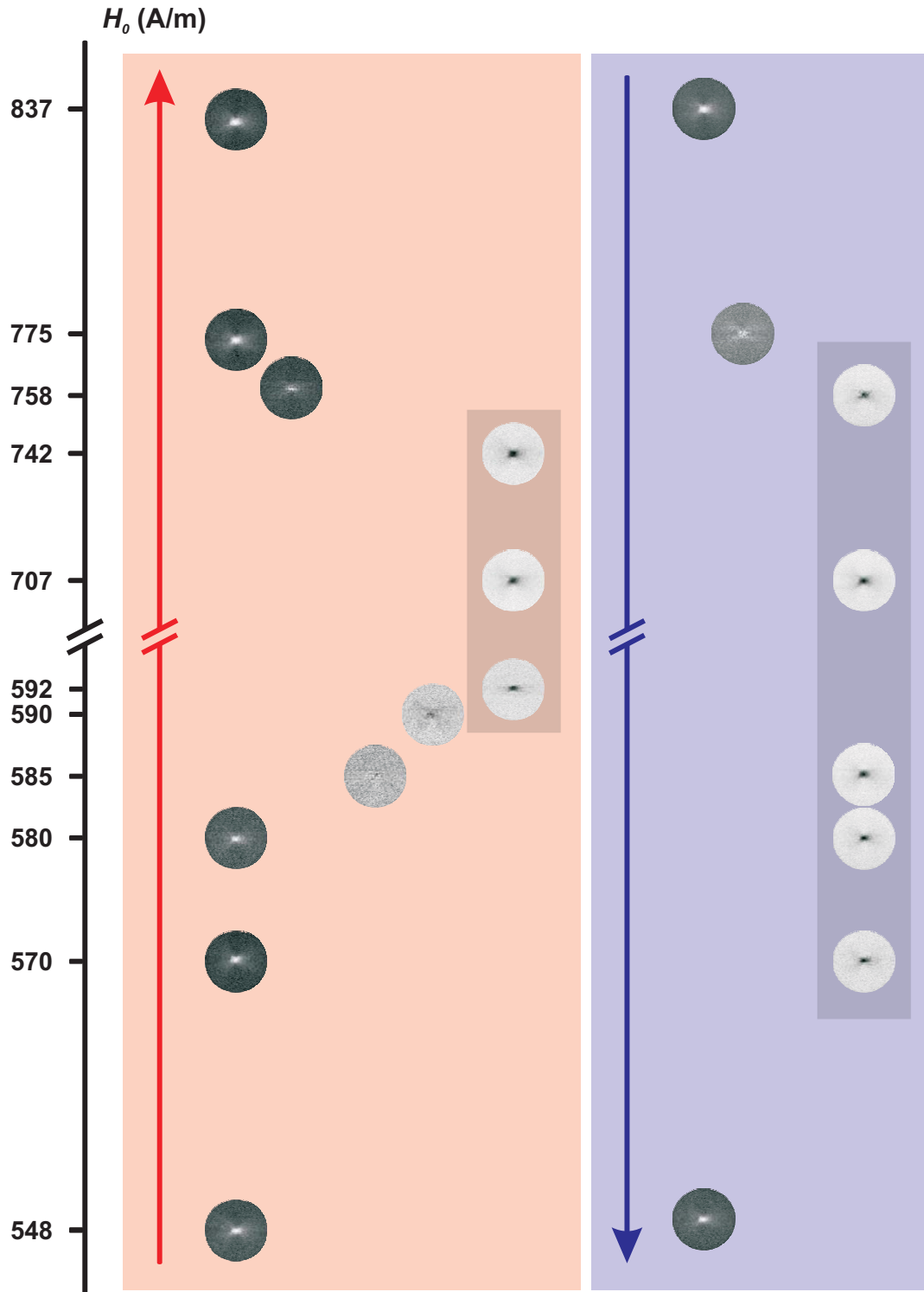


Figure 5.27: Dynamic response for a Permalloy disk with a diameter of $2\ \mu\text{m}$ and a thickness of $50\ \text{nm}$, excited by a continuous alternating magnetic field – thresholds of the switching levels. The differential contrast is depicted in the left column for increasing field amplitudes (red area/arrow). The response for decreasing field amplitudes is shown in the right column (blue area/arrow). The differential images were recorded at one phase with respect to the external field ($f = 250\ \text{MHz}$).

in field amplitude of only 10 A/m is already capable to reverse the vortex core magnetization.

Figure 5.28 shows the differential contrast for the same disk at higher field amplitudes and at a fixed phase with respect to the external field. The differential contrast changes for increasing field amplitudes from a white dot (vortex structure displaced downwards, using look-up table I in Figure 5.1) to a black/white cross (vortex structure displaced to the right), and at even higher field amplitudes, here at about 1304 A/m, a black dot (vortex structure displaced upwards) becomes more pronounced, but a black/white cross is still present. The dynamic contrast decreases at 1225 A/m & 1265 A/m, which indicates multiple reversal processes during one measurement at these specific field amplitudes. If these images with loss of differential contrast would correspond to a transition to a new switching level, the “black dot” at higher field amplitudes would then represent an additional level. Nevertheless, a clear black dot cannot be distinguished as was the case at 707 A/m in Figure 5.26, which in turn indicates a phase shift in the gyrotropic motion.

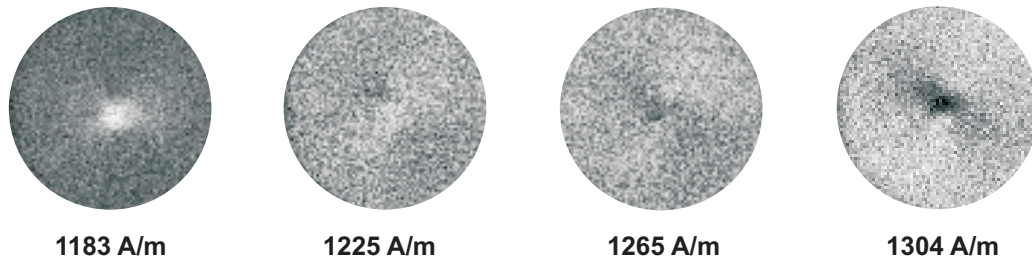


Figure 5.28: Dynamic response for a Permalloy disk with a diameter of $2\ \mu\text{m}$ and a thickness of 50 nm, excited by a continuous alternating magnetic field – phase shift at higher field amplitudes. The differential contrast is depicted for increasing field amplitudes at one phase with respect to the external field ($f = 250\ \text{MHz}$).

5.4.6 Hysteresis behaviour III: breaking of symmetry

- The hysteresis effect as mentioned in Paragraph 5.4.2 was also observed directly by imaging the out-of-plane component of the magnetization for a $500\ \text{nm} \times 500\ \text{nm} \times 40\ \text{nm}$ Permalloy square. Figure 5.29 shows the switching scheme, illustrated with surface plots representing the direct “averaged” magnetic contrast $\Gamma^{-/+}(\text{direct})$. The direction of the peaks corresponds to the direction of the out-of-plane vortex core magnetization. The structure was excited with an alternating magnetic field with a frequency of 437.5 MHz. Two stable levels could again be found where the vortex core has a certain polarization, but at

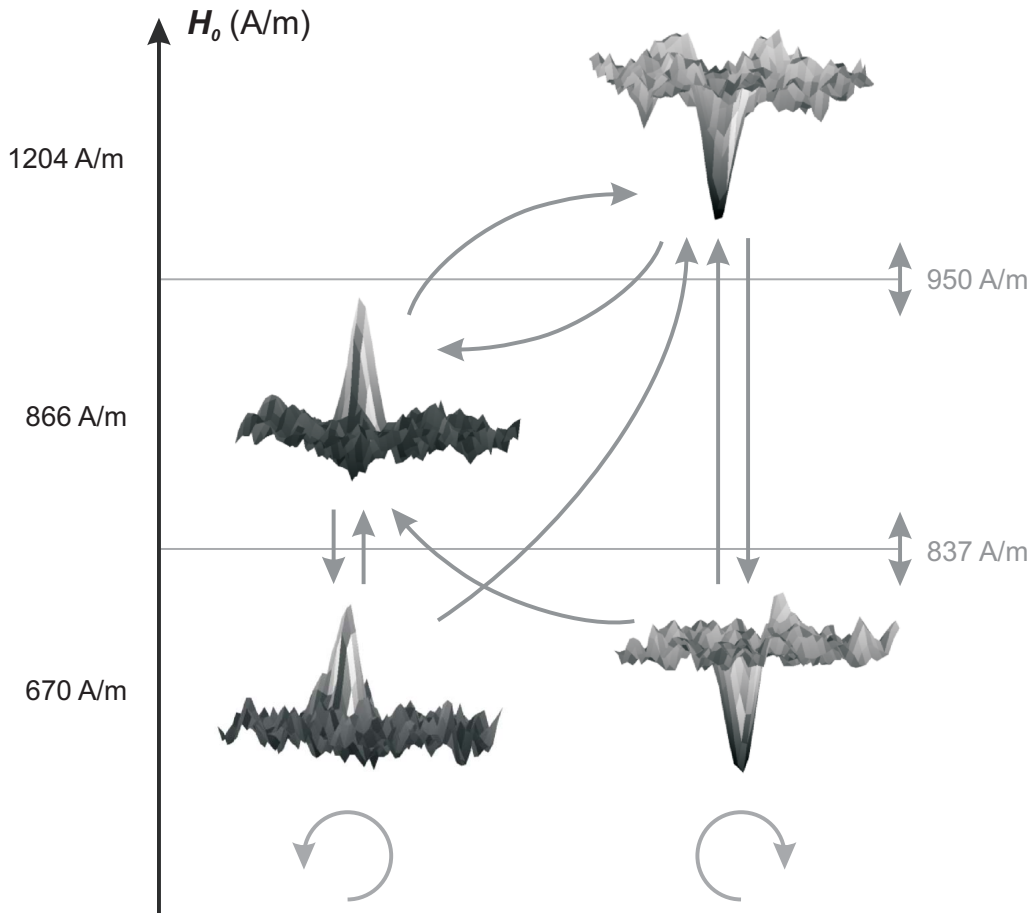


Figure 5.29: Hysteresis behaviour for a $500 \text{ nm} \times 500 \text{ nm}$, 40 nm thick Permalloy element. The surface plots represent the direct “averaged” magnetic contrast $\Gamma^{-/+}(\text{direct})$ at a certain fixed phase with respect to the exciting field ($f = 437.5 \text{ MHz}$). The arrows constitute the scheme for the reversal of the direction of the out-of-plane core magnetization. The sense of gyration of the vortex structure is indicated by the circular arrows below.

lower field amplitudes, a region is found where both directions of the core magnetization are possible. The two core directions can be obtained depending on the field amplitude history. The images from Figure 5.29 are magnified views of an area of $300 \text{ nm} \times 300 \text{ nm}$, taken at a phase of 270° with respect to the exciting alternating field. The arrows show how every state can be reached. The sense of gyration of the vortex structure is indicated by the circular arrows below.

- This sense of gyration is confirmed in Figure 5.30, where the vortex core motion can be followed for the four different cases. The position of the core is imaged at 8 different phases with respect to the external magnetic field. The vortex core gyrates clockwise when it is pointing down (black dot), and counterclockwise when it is pointing up (white dot). The procedure described by the Eqs. (5.5) & (5.6) was used to deduce the sequence of images, explaining at the

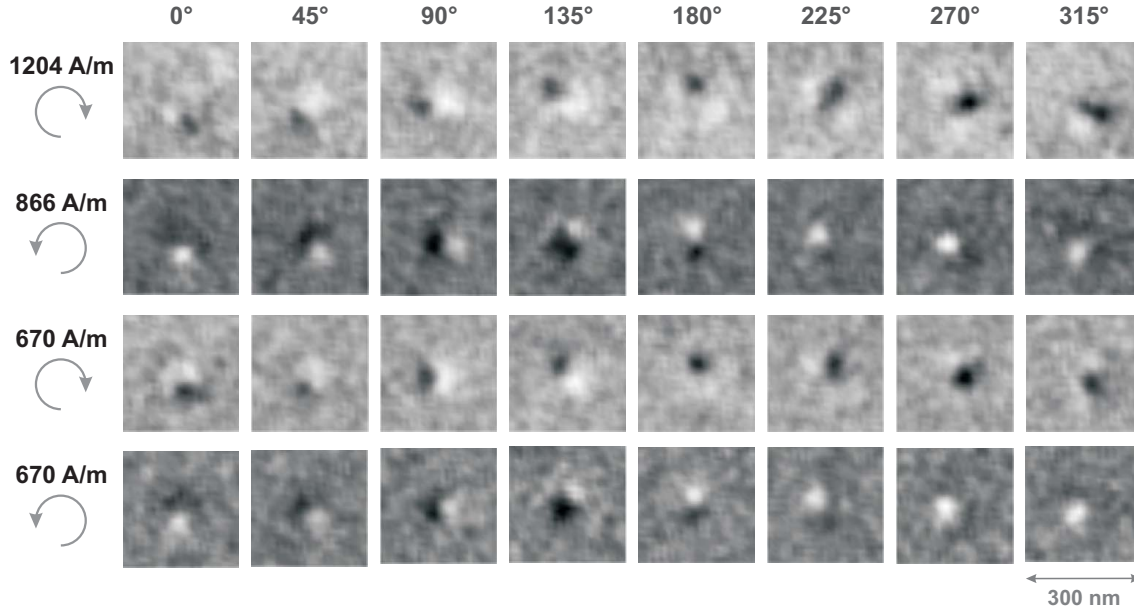


Figure 5.30: Dynamic response for a $500 \text{ nm} \times 500 \text{ nm}$, 40 nm thick vortex structure, excited by a continuous alternating magnetic field. The “averaged” out-of-plane magnetic contrast $\Gamma_i^{-/+}(\text{direct})$ is depicted at eight different phases with respect to the external field for the different levels found in Figure 5.29.

same time also the appearance of artefacts which is, e.g., very clear at phase 135° (cf. Paragraph 5.4.1).

- The vortex core velocity was also deduced from this data set, using the same procedure as described in Paragraph 5.4.3 (& Eq. (5.7)). Detailed field amplitude scans were performed and the vortex core velocity was extracted as a function of the field amplitude. The results of these scans are plotted in Figure 5.31. The switching thresholds from Figure 5.29 are indicated with vertical lines to specify when a reversal of the core magnetization occurs. The dashed lines are only a guide to the eye for the lower switching threshold, but no reversal is occurring at that threshold during that specific amplitude scan (in panel (a) & (c)). The yellow arrows in the panels (a) - (c) indicate whether the field amplitude was increased or decreased.

First, a scan was started at a low field amplitude, at around 500 A/m (corresponding to the lower left case in Figure 5.29), for a vortex core pointing up (blue curve in the panels (a) & (d) in Figure 5.31). The field amplitude was then increased in small steps, indicated by the yellow arrow. The vortex core moves faster with increasing field amplitude. The velocity increases in first approximation linearly with the field amplitude until around 950 A/m . An abrupt increase is observed in the speed around 950 A/m , where the vortex core switches from

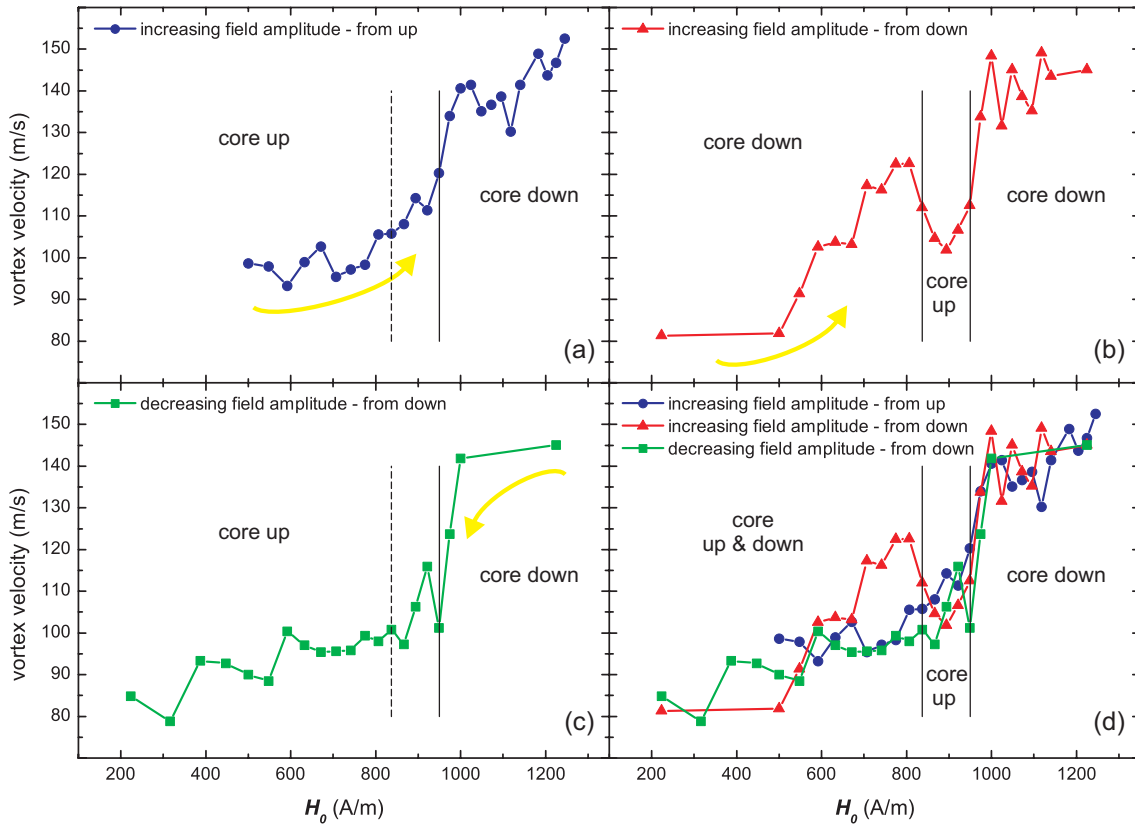


Figure 5.31: Vortex core velocity during the gyrotropic motion, as a function of the amplitude of the alternating magnetic field, for a $500 \text{ nm} \times 500 \text{ nm}$, 40 nm thick Permalloy element. Different field amplitude scans are shown. Starting from a state at low field amplitude with the core pointing up (panel (a)) and down (panel (b)), respectively, the amplitude is increased gradually. The amplitude is decreased from a high field amplitude state with the core pointing down in panel (c). The curves from panel (a) - (c) are collected in panel (d). The field amplitude thresholds for switching are indicated with the vertical lines. The dashed lines in panel (a) & (c) are a guide to the eye for the lower switching threshold. No switching is occurring at this threshold in panel (a) & (c).

up to down (reversal at the higher threshold in Figure 5.29). A further increase of the field amplitude, after the reversal, is not causing a large change in the velocity anymore.

A jump in the field amplitude was made afterwards going back to a lower field amplitude, at about 200 A/m (lower right case in Figure 5.29). A scan is now started with originally the vortex core pointing down (red curve in the panels (b) & (d) in Figure 5.31). The velocity increases now much faster with increasing field amplitude. The speed collapses when it switches at about 837 A/m (reversal at the lower threshold in Figure 5.29). The vortex core is now pointing up again and for increasing field amplitude, the course of the speed is the same as observed for the blue curve with a switch around 950 A/m .

Now starting from a vortex core pointing down, and excited with a high field amplitude (upper right case in Figure 5.29), the field amplitude is gradually lowered (green curve in the panels (c) & (d) in Figure 5.31). The speed makes a jump as expected at around 950 A/m, where the vortex core switches to up (reversal at the higher threshold in Figure 5.29). The speed then gradually decreases with decreasing field amplitude and no switching occurs furthermore.

All three curves were brought together in panel (d). A distinct difference can now be observed in the speed for the vortex core pointing up (red curve) and down (blue & green curves), respectively, in the region between 700–800 A/m. The same behaviour was already observed in the results presented in Figure 5.24.

- The trajectories of the vortex core, from the above presented data, are depicted in Figure 5.32 for the vortex core pointing up and down, respectively, at a field amplitude H_0 of 670 A/m & 775 A/m (cf. these four points in the blue and red curves of Figure 5.31). A blue dot is used to indicate the vortex core position at phase 0° . The consecutive phase steps (in 45° steps) can be found simply by following the gray arrows. In the first row, at 670 A/m, the extent of the gyrotropic motion is fairly the same for both core polarizations. The difference in extent of the vortex core motion can on the other hand clearly be observed in the second row, at 775 A/m. This was also clearly visible in Figure 5.31, where a discrepancy arose in the vortex core speed in a certain range of the applied field amplitude. A hairneedle stripline was used, so the vortex core is coinciding at the upper and lower position in the vortex gyration, when both trajectories would be overlaid (cf. discussion in Paragraph 5.4.1). The first row of Figure 5.32 illustrates this behaviour, where the core positions coincide at the lower position at a phase between 0° and 45° . Interestingly enough, this is not the case in the second row of Figure 5.32. For the core pointing up, the core position at phase 0° is at the lowest point of the “circular” trajectory. The position at the same phase for the core pointing down, is clearly not coinciding with this lowest point. This phase shift can also be observed, but less clearly, in Figure 5.24. As the excitation frequency remains the same for both core polarizations, this indicates a slightly different resonance frequency of the gyrotropic motion for both cases. These observations indicate that in a certain low field amplitude range, the vortex structure is moving in a different potential for the two opposite core polarizations. The possible occurrence of different resonance frequencies in the vortex structure was already noted in Paragraph 5.2.1.

5.4.7 Discussion

There is still a considerable amount of doubt about the origin of the field amplitude dependent asymmetry in the response of a vortex structure. This asymmetry does not only show up in the above mentioned vortex core trajectories at a fixed field amplitude of the alternating field. The symmetry of the system is also violated in general due to the appearance of a stable core polarization at specific field amplitudes of the exciting field (cf. Paragraphs 5.4.1 & 5.4.2). Down the bottom line, two different principles can be envisioned for the explanation.

- Until now no geometrical or structural asymmetries were considered in the discussion. Different surface roughness at both sides of the sample or local imperfections might influence the motion when the vortex core is pointing up or down. Nevertheless, such randomly distributed imperfections seem to be rather inconceivable to resolve the current problems as the same reversal scheme could be observed in different structures (cf. Figures 5.20, 5.21 & 5.29), exhibiting different defect or roughness distributions. The answer seems thus to have a more fundamental origin.

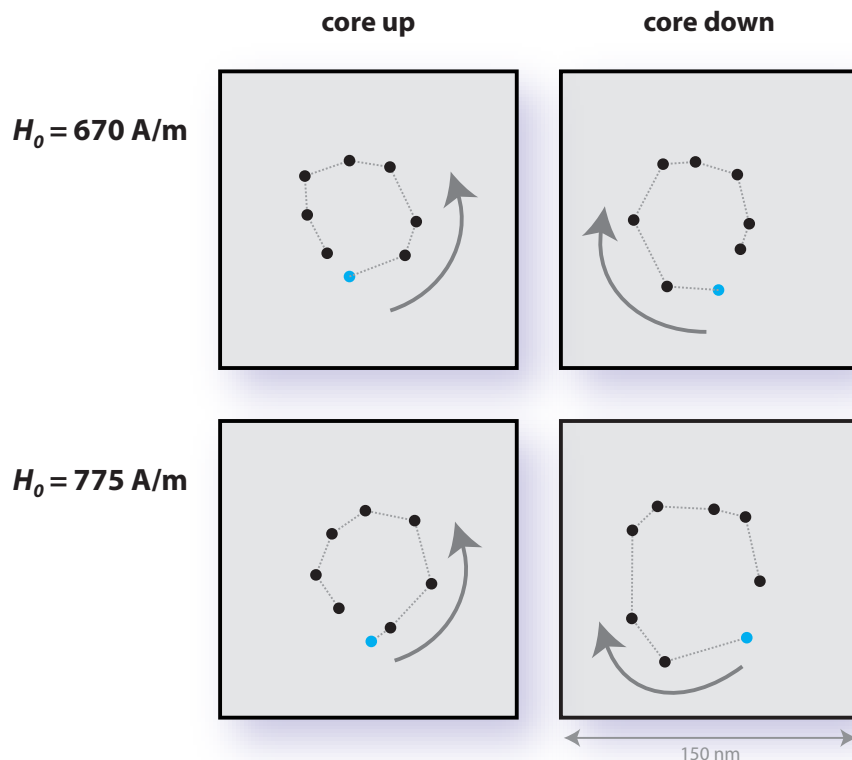


Figure 5.32: Illustration of the asymmetry in the vortex core trajectories for a core pointing up and down, respectively, in a $500 \text{ nm} \times 500 \text{ nm}$, 40 nm thick Permalloy element. The field amplitude H_0 was set to 670 A/m & 775 A/m .

- Another cause for this asymmetry can be the applied field. Assuming a perfectly symmetric Landau pattern, an alternating magnetic field at the gyrotropic resonance frequency will induce a circular motion of the vortex structure. The sense of gyration depends only on the direction of the magnetization in the vortex core (up or down), but the in-plane magnetization configuration, surrounding the core, stays hereby the same. The vortex core is thus moving in the same, or the opposite sense with respect to the in-plane flux closure, depending on the core polarization.

Together with the in-plane magnetization around the vortex core, the influence of domain walls was until now also neglected. Even if the asymmetry is also present when domain walls are absent, as observed in the switching behaviour in circular samples (cf. Paragraph 5.4.5), the influence of domain walls in square-shaped samples cannot be neglected. A clear observation supporting this statement is shown in Figure 5.33. The out-of-plane magnetic contrast was imaged for a $1.5\ \mu\text{m} \times 1.5\ \mu\text{m}$, 50 nm thick Permalloy element, excited with an in-plane alternating magnetic field with an amplitude of H_0 of 630 A/m. The frequency f was set to 187.5 MHz. The figure shows the differential contrast, and beside the gyrotropic vortex core motion in the middle, a complex excitation mode can be observed along the four domain walls. The spins along the lower right “Néel wall” appear to precess uniformly out of the plane (e.g. at $90^\circ/270^\circ$) while at the other three domain walls, out-of-plane components arise around the middle of the domain walls. This out-of-plane substructure also moves longitudinally along the domain wall, like a fixed spring. This can most clearly be seen in the lower left domain wall at, e.g. $90^\circ/270^\circ$, where black and white dots are formed diagonally.

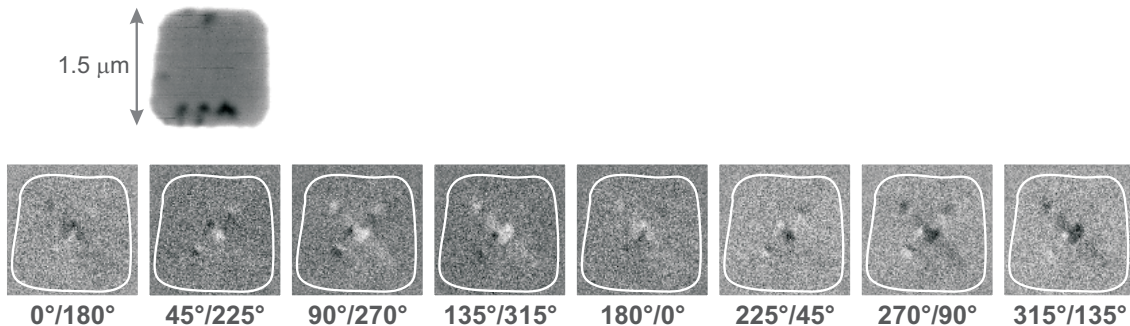


Figure 5.33: Dynamic response for a $1.5\ \mu\text{m} \times 1.5\ \mu\text{m}$, 50 nm thick vortex structure, excited by a continuous alternating magnetic field ($H_0 = 630\ \text{A/m}$, $f = 187.5\ \text{MHz}$). The out-of-plane magnetic contrast was recorded at eight different phases with respect to the external field. The corresponding differential images are depicted.

Nonetheless, simple two dimensional micromagnetic simulations do not show this behaviour, nor the influence of the in-plane magnetization around the vortex core on the asymmetry of the trajectories, owing either to a wrong conception of the problem or to inadequate simulations. The results in Figure 5.33 indicate that specific modes can be excited with an alternating field with a frequency in the sub-GHz range. The occurrence of different levels might thus be the result of the interaction between the gyrotropic motion with other modes. Some modes may also be induced by the gyrotropic motion itself.

CHAPTER 6

CONCLUSIONS AND PERSPECTIVES

“Welcome to the end of the thought process.”

— DR. GREGORY HOUSE

6.1 CONCLUSIONS

Magnetic thin film structures were studied by means of a scanning transmission x-ray microscope. The static configuration of micron-sized vortex structures was imaged. The in-plane as well as the out-of-plane magnetic contrast were recorded. The in-plane curling magnetization can clearly be observed thanks to the XMCD effect. The vortex core size and the total magnetic contrast of Ni at the core, could also be evaluated for a Permalloy structure with a single vortex. Beside single layers, stacks of two different ferromagnetic layers (Permalloy & Co) with an insulating Cu layer in between, were also probed separately by taking advantage of the element specificity of the XMCD effect. Complex domain patterns appear due to a coupling between the magnetic layers.

In order to investigate the dynamic behaviour of such structures, a stroboscopic measurement technique was implemented into the scanning transmission x-ray microscope. Time-resolved studies could be performed with a time resolution of about 70–100 ps and a lateral resolution of 30–40 nm. The lateral size of the vortex structures was chosen between 200 nm–2 μ m, with a thickness ranging from 30–50 nm. The confined patterns were excited using three different excitation types: pulsed excitation, sine excitation, and burst excitation. The in-plane as well as the out-of-plane, time dependent magnetization distribution were imaged.

The gyrotropic mode in ferromagnetic structures with a single vortex, was investigated intensively. Not only was the gyrotropic motion imaged, providing

qualitative information, but quantitative results were derived as well. In the first instance, a differential imaging technique was introduced reducing drastically the signal-to-noise-ratio. The gyrotropic motion was then observed by recording images of the relaxation process after a fast in-plane field pulse excitation. The resonance frequency of the gyrotropic mode was determined as a function of the aspect ratio of the patterns. The excitation of a vortex structure with single bursts, showed that the vortex core was gyrating with a constantly increasing phase shift. Furthermore, the gyrotropic motion was observed using a resonant sine excitation with a frequency close to the gyrotropic resonance frequency. At very low field amplitudes, a linear response was observed for the extent of the gyrotropic motion (\sim velocity) as a function of the field amplitude. Non-linear effects occur at slightly higher field amplitudes of the exciting field. The reversal of the out-of-plane vortex core magnetization was performed by changing the amplitude of the alternating magnetic field. The reversal was observed indirectly by investigating the sense of gyration, but also directly by imaging the out-of-plane magnetic contrast. Different field amplitude levels were observed with a fixed vortex core polarization, but both states can appear at lower field amplitudes, showing a complex hysteresis behaviour. A different reversal scheme was introduced as well where the out-of-plane vortex core magnetization could be reversed by applying short in-plane bursts of an alternating magnetic field. Two dimensional micromagnetic simulations indicated that the reversal process is the result of the consecutive creation and annihilation of a vortex-antivortex pair. Finally, the vortex core velocity was determined as a function of the field amplitude of the alternating magnetic field. Clear jumps occur at the corresponding switching thresholds. Additionally, in a specific field amplitude range, a clear discrepancy can be distinguished in the vortex core speed for a core pointing up and down, respectively.

The gyrotropic motion was also imaged for a trilayer system composed of two different ferromagnetic layers (Permalloy & Co) with an insulating Cu layer in between. The stack was excited with an alternating magnetic field and due to the coupling between the ferromagnetic layers, different dynamic motions appear in the two layers. The motion in the Co layer deviates from a gyrotropic motion.

6.2 PERSPECTIVES

The results presented in this work provide important insights in the magnetization dynamics of ferromagnetic vortex structures, but also form the basis for further research. The pulsed excitation experiments described in this work give

an adequate method to study the relaxation behaviour on individual ferromagnetic structures. Modes up to 3 GHz can be addressed with a time resolution of 100 ps, which is amply sufficient to study the gyrotropic mode on a sub-micron length scale. The good lateral resolution allows in addition to probe substructures of the system, like domain walls and the vortex core in magnetic Landau patterns. The controlled introduction of artificial defects, e.g., treatment with a focussed ion beam (FIB), can also be investigated through this way.

The current state of the time-resolved imaging technique used in this work also still leaves room for improvement. The amount of images recorded simultaneously was till now limited to a maximum number of 12 counting channels with a minimum time spacing, in multi bunch mode, of 2 ns between the different channels. The synchronization between the excitation and the probing photon flashes was done obeying the following relation:

$$m \times T_{exc} = \frac{328}{500 \text{ MHz}}. \quad (6.1)$$

In words, a whole number of times the period of the excitation T_{exc} gives exactly the orbit clock ($328/500 \text{ MHz} =$ the time needed for an electron bunch to perform one turn in the storage ring). The repetition rate or frequency of the excitation f_{exc} can be derived following:

$$\frac{1}{T_{exc}} = f_{exc} = 500 \text{ MHz} \times \frac{m}{328} = 500 \text{ MHz} \times \frac{m}{2 \times 2 \times 2 \times 41}. \quad (6.2)$$

For the synchronization, irrational numbers are prohibited in the choice of f_{exc} . m needs thus to be the prime number 41 or a multiple of 41. This method was sufficient to perform a rough investigation of the dynamics in vortex structures. Finer time steps can only be achieved by performing additional measurements by changing the delay of the excitation. Such a measurement scheme is unfortunately prone to thermal drifts and mechanical vibrations, causing misalignments and distortions of the consecutively recorded images. However the amount of simultaneously recorded images can be extended so that the interleaving time steps can be imaged as well. The repetition rate of the excitation needs then to be chosen in this way that a whole number of times the period of the excitation gives now a defined number (n) of times the orbit clock (instead of once):

$$f_{exc} = 500 \text{ MHz} \times \frac{m}{n \times 2 \times 2 \times 2 \times 41}. \quad (6.3)$$

m and n are now chosen in this way that the excitation is not synchronized with all photon flashes, but only after a certain amount of photon flashes. More specifically, m may not be a multiple of the common divisors of n , 2 and 41.

The acquisition needs to be adjusted accordingly. The “unsynchronized” photon flashes probe the dynamic response at the interleaving time steps. In this way, beam fluctuations are also averaged out. Although the measuring time would increase considerably depending on how fine the time steps need to be, no further realignments would be necessary in the analysis. In this way trajectories can be determined more accurately so that the vortex core dynamics can be studied in more detail.

The dynamics of the magnetization reversal in magnetic particles is of great relevance for applications in high density magnetic recording media and spintronic circuits. Although the reversal of the out-of-plane vortex core magnetization is still not fully understood, magnetic structures with a single vortex can be considered for the implementation in magnetic data storage devices with several advantages, e.g., high thermal stability, insensitivity to external static fields, and minimal cross-talk between neighbouring patterns. Therefore two main points need to be addressed:

- Possible technological implementations would require a reliable switching scheme. Simple in-plane alternating magnetic fields introduce many uncontrollable and until now not understood hysteresis phenomena. Micromagnetic simulations nevertheless indicate that the application of an in-plane rotating field $\mathbf{H} = H_0(\cos(2\pi ft), \sin(2\pi ft), 0)$ is capable to reverse the vortex core reliably [102]. Such fields can be realized using crossed striplines. The switching back process can simply be achieved by changing the phase of the excitation through one of the striplines.
- A remaining critical problem is the reading out of the direction of the core magnetization. As the core region has a width of only 10–20 nm, a very good sensor is needed to amplify the out-of-plane magnetic signal of the core. Such amplification can be thought of by introducing a soft magnetic layer with perpendicular magnetization, like FeGd [103]. Stacks would eventually have to be produced in order to measure a magnetoresistive signal. This unfortunately complicates the dynamics due to coupling mechanisms between the magnetic layers (cf. Section 5.3).

It should also be remarked that a large variety of dynamic processes still lies hidden. Exploring the physical limits of these processes and furthermore developing improved magnetic switching strategies form the current challenges in magnetization dynamics. Time-resolved scanning transmission x-ray microscopy most certainly belongs to one of the techniques that can help solve

these intricate questions. Better lateral and time resolution are needed though. The improvement of the lateral resolution is binded to the development of better zone plates, or other x-ray optics. On the other hand, the time resolution can be improved by reducing the electron bunch length, e.g., by lowering the momentum-compactness factor α or by strong rf focussing [104]. Another way is to introduce a correlation between the longitudinal temporal coordinate and a more easily accessible quantity like the transverse coordinate or angle, so that the radiation can be selected from a bunch slice or the radiation pulses can be compressed [104]. Nevertheless, these methods imply a serious reduction of the photon flux. This can be remedied, not by altering the electron bunches itself, but by adjusting the detection scheme so that it is independent of the width of the probing x-ray flashes. Therefore a fast enough detector needs to be implemented in order to measure precisely the arrival times of the photons, in the detector. A time resolution of about 10 ps is then expected.

Finally, as an endnote, a roadmap can be proposed for future measurements in order to uncover the doubts posed by the appearance of different switching levels in ferromagnetic structures with a single vortex. A first step lies in an improved and more controlled preparation of the samples. Epitaxial depositions can be considered to improve the surface roughness. On the other hand, the surface roughness of the structures can largely be influenced by the substrate. A rough substrate automatically will cause rough sample surfaces. Thus, instead of evaporating the structures on top of a (rough) stripline, the structures could first be deposited on the very smooth Si_3N_4 membrane with the Cu stripline on top of the structures. A better lithography is also needed so that arrays can be produced of identical patterns. This automatically leads to step two where more systematic measurements are necessary. The initial state of the vortex core magnetization (up or down), right after the sample preparation, is an important information which was until now not investigated. Whether both states are distributed equally or there is already in the static case a preference for the vortex core to be pointing in one of the two directions, can already indicate how important the sample preparation is. It is then important to know whether or not a very small in-plane alternating magnetic field will influence the vortex core polarization. Again, an equal distribution of both states or an unequal one is important to consider. In a third step, the gyrotropic mode needs to be characterized quantitatively, i.e., investigation of the resonance frequency and the damping behaviour. This can be achieved by performing pulsed excitation measurements. Eventually, in a next step, detailed field amplitude scans need to be performed in order to investigate the different levels. Caution is needed though when performing field amplitude scans on large arrays

of identical patterns. Images are in principle recorded with the STXM of single structures, but a field amplitude scan on a single structure may induce reversal processes in the other structures, which cannot be observed in that case. This inevitably causes complications in order to perform systematic measurements. A field amplitude scan of all structures in parallel would thus seem to be the most accurate but also the most time consuming method. Finally, once the levels are investigated, single vortex structures should be investigated in more detail by determining the trajectory and speed of the moving vortex core. The promised improvement in lateral and time resolution will also allow to observe spin wave modes. The interaction of these modes with the gyrotropic motion can then be investigated and especially the possible influence on the multiple switching levels.

APPENDIX A

THE ADVANCED LIGHT SOURCE (ALS)

The Advanced Light Source (ALS) is a third-generation synchrotron light source and is operated by Lawrence Berkeley National Laboratory in California. The facility generates intense light optimized for spectroscopy and imaging in the ultra-violet and soft x-ray regions of the electromagnetic spectrum. The facility is funded by the U.S. Department of Energy's Office of Basic Energy Sciences. Table A.1 shows typical parameters of the storage ring. Figure A.1 shows a simple schematic of the synchrotron radiation source at the ALS.

Electron beam energy	1 – 1.9 GeV
Injection energy	1 – 1.5 GeV
γ	3720
Bunch spacing	
multi bunch mode	2 ns
two bunch mode	328 ns
Beam current	
multi bunch mode	400 mA
two bunch mode	2×25 mA
Circumference	196.8 m
RF frequency	499.642 MHz
Number of straight sections	12
Beam lifetime	
multi bunch mode	~ 8 hours @ 400 mA
two bunch mode	~ 60 minutes @ 40 mA
Horizontal emittance	6.3 nm rad
Vertical emittance	0.13 nm rad
Energy spread ($\Delta E/E$, rms)	1×10^{-3}
Pulse duration (FWHM)	70 ps ¹

Table A.1: Typical parameters of the storage ring for the Advanced Light Source (ALS), operated by the Lawrence Berkeley National Laboratory in California (USA).

¹In multi bunch mode, the bunch length is deliberately increased using harmonic cavities to improve the beam lifetime. In two bunch mode, the bunch length is current dependent and decreases from about 70 ps at high bunch current to below 40 ps at small current.

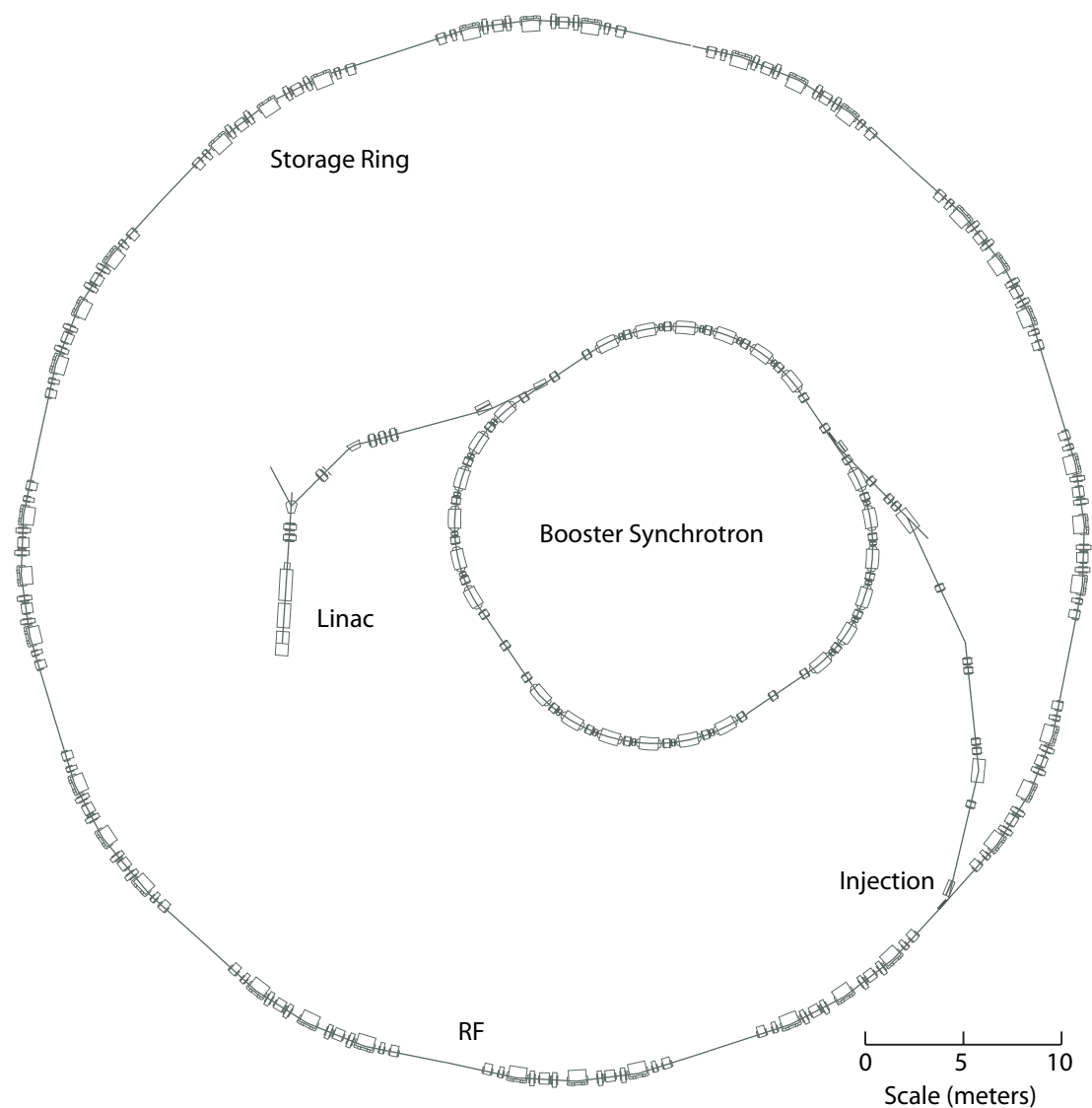


Figure A.1: Illustration of the synchrotron radiation source at the ALS. The sketch shows a linear accelerator (linac) and booster synchrotron that bring electrons up to an energy, matched to storage ring magnet settings; an injection system, which directs electrons into the ring; and a radio frequency (rf) generator to replenish the energy lost to synchrotron radiation as the electrons pass bending magnets, undulators, and wigglers.

APPENDIX B

STRIPLINE CHARACTERIZATION

The field values and distribution generated by a stripline can be calculated analytically. Using the notation from Figure B.1, and for a current I flowing in the stripline; an in-plane magnetic field H is generated with amplitude H_0 [105]:

$$H_0 = -\frac{I}{8\pi ab} \left[u \left[\frac{1}{2} \ln \left(\frac{g^2 + u^2}{h^2 + u^2} \right) + \frac{g}{u} \arctan \left(\frac{u}{g} \right) - \frac{h}{u} \arctan \left(\frac{u}{h} \right) \right] - v \left[\frac{1}{2} \ln \left(\frac{g^2 + v^2}{v^2 + h^2} \right) + \frac{g}{v} \arctan \left(\frac{v}{g} \right) - \frac{h}{v} \arctan \left(\frac{v}{h} \right) \right] \right], \quad (\text{B.1})$$

with $u = a - X$, $v = -a - X$, $g = b - Y$, and $h = -b - Y$. The field amplitude on the surface of the stripline, at $(X, Y) = (0, b)$, can then be evaluated and the following relation results:

$$H_0 \approx \frac{I}{4a}. \quad (\text{B.2})$$

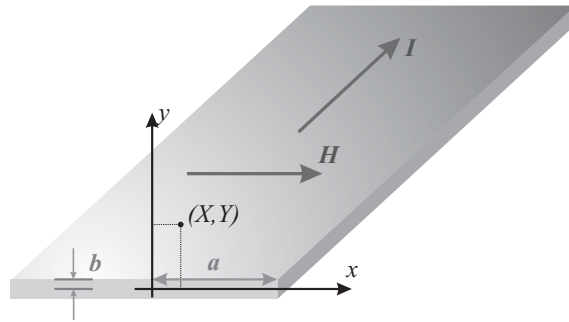


Figure B.1: Sketch of a stripline with the corresponding dimensions, used for the field calculations.

A power (in mW) is measured during the experiments and converted into a current I , considering a 50Ω impedance-matched stripline [21]. The field amplitude (in A/m) can then simply be calculated using Eq. (B.2).

All equations and field amplitude values, presented in this work, were introduced using the International System of Units (SI). However, most of the specialized literature in the field of magnetism still employs the CGS system of units and interchange the terms field & induction. Therefore Table B.1 was added for a fast conversion.

P (mW)	I (A)	H_0 (A/m)	B_0 (mT) ($B_0 = \mu_0 H_0$)	B_0 (G) = H_0 (Oe) (1 G $\hat{=}$ 0.1 mT)
0.5	0.0032	158.11	0.20	2.0
1	0.0045	223.61	0.28	2.8
2	0.0063	316.23	0.40	4.0
3	0.0077	387.30	0.49	4.9
4	0.0089	447.21	0.56	5.6
5	0.0100	500.00	0.63	6.3
6	0.0110	547.72	0.69	6.9
7	0.0118	591.61	0.74	7.4
8	0.0126	632.46	0.79	7.9
9	0.0134	670.82	0.84	8.4
10	0.0141	707.11	0.89	8.9
15	0.0173	866.03	1.09	10.9
20	0.0200	1000.00	1.26	12.6
25	0.0224	1118.03	1.40	14.0
30	0.0245	1224.74	1.54	15.4
35	0.0265	1322.88	1.66	16.6
40	0.0283	1414.21	1.78	17.8
45	0.0300	1500.00	1.88	18.8
50	0.0316	1581.14	1.99	19.9
60	0.0346	1732.05	2.18	21.8
70	0.0374	1870.83	2.35	23.5
80	0.0400	2000.00	2.51	25.1
90	0.0424	2121.32	2.67	26.7
100	0.0447	2236.07	2.81	28.1

Table B.1: Conversion table for the field amplitude H_0 (in A/m & Oe), and the induction B_0 (in mT & G). The first two columns are the measured power P (in mW) and current I (in A), respectively.

BIBLIOGRAPHY

- [1] A. Hubert and R. Schäfer. *Magnetic Domains. The Analysis of Magnetic Microstructures*. Springer-Verlag Berlin Heidelberg, 1998.
- [2] M. R. Freeman and B. C. Choi. Advances in magnetic microscopy. *Science*, 294:1484–1488, 2001.
- [3] H. J. Williams, F. G. Foster, and E. A. Wood. Observation of magnetic domains by the Kerr effect. *Phys. Rev.*, 82:119–120, 1951.
- [4] J. N. Chapman. The investigation of magnetic domain structures in thin foils by electron microscopy. *J. Phys. D*, 17:623–647, 1984.
- [5] S. McVitie, J. N. Chapman, L. Zhou, L. J. Heyderman, and W. A. P. Nicholson. In-situ magnetising experiments using coherent magnetic imaging in TEM. *Journal of Magnetism and Magnetic Materials*, 148:232–236, 1995.
- [6] K. Koike and K. Hayakawa. Scanning electron microscope observation of magnetic domains using spin-polarized secondary electrons. *Jpn. J. Appl. Phys.*, 23:L187–L188, 1984.
- [7] M. R. Koblischka, U. Hartmann, and T. Sulzbach. Improving the lateral resolution of the MFM technique to the 10 nm range. *Journal of Magnetism and Magnetic Materials*, 272–276:2138–2140, 2004.
- [8] R. Wiesendanger, H.-J. Güntherodt, G. Güntherodt, R. J. Gambino, and R. Ruf. Observation of vacuum tunneling of spin-polarized electrons with the scanning tunneling microscope. *Phys. Rev. Lett.*, 65:247–250, 1990.
- [9] M. Johnson and J. Clarke. Spin-polarized scanning tunneling microscope: Concept, design, and preliminary results from a prototype operated in air. *Journal of Applied Physics*, 67:6141–6152, 1990.
- [10] S. Heinze, M. Bode, A. Kubetzka, O. Pietzsch, X. Nie, S. Blügel, and R. Wiesendanger. Real-space imaging of two-dimensional antiferromagnetism on the atomic scale. *Science*, 288:1805–1808, 2000.

- [11] H. Pinkvos, H. Poppa, E. Bauer, and J. Hurst. Spin-polarized low-energy electron microscopy study of the magnetic microstructure of ultra-thin epitaxial cobalt films on W(110). *Ultramicroscopy*, 47:339–345, 1992.
- [12] J. Stöhr, Y. Wu, B. D. Hermsmeier, M. G. Samant, G. R. Harp, S. Koranda, D. Dunham, and B. P. Tonner. Element-specific magnetic microscopy with circularly polarized x-rays. *Science*, 259:658–661, 1993.
- [13] C. M. Schneider, K. Holldack, M. Kinzler, M. Grunze, H. P. Oepen, F. Schäfers, Petersen H., K. Meinel, and J. Kirschner. Magnetic spectroscopy from Fe(100). *Appl. Phys. Lett.*, 63:2432–2434, 1993.
- [14] P. Fischer, G. Schütz, G. Schmahl, P. Guttman, and D. Raasch. Imaging of magnetic domains with the x-ray microscope at BESSY using x-ray magnetic circular dichroism. *Zeitschrift für Physik B Condensed Matter*, 101:313–316, 1996.
- [15] H. Stoll, A. Puzic, B. van Waeyenberge, P. Fischer, J. Raabe, M. Buess, T. Haug, R. Höllinger, C. Back, D. Weiss, and G. Denbeaux. High-resolution imaging of fast magnetization dynamics in magnetic nanostructures. *Appl. Phys. Lett.*, 84:3328–3330, 2004.
- [16] A. Puzic, B. Van Waeyenberge, K. W. Chou, P. Fischer, H. Stoll, G. Schütz, T. Tyliczszak, K. Rott, H. Brückl, G. Reiss, I. Neudecker, T. Haug, M. Buess, and C. H. Back. Spatially resolved ferromagnetic resonance: Imaging of ferromagnetic eigenmodes. *Journal of Applied Physics*, 97:10E704, 2005.
- [17] W. F. Brown. *Micromagnetics*. New York: Interscience, 1963.
- [18] A. Aharoni. *Introduction to the Theory of Ferromagnetism*. Monographs on Physics, Oxford University Press, 1996.
- [19] L. D. Landau and E. Lifshitz. On the theory of the dispersion of magnetic permeability in ferromagnetic bodies. *Phys. Z. Sowjetunion*, 8:153–169, 1935.
- [20] C. Kittel. Physical theory of ferromagnetic domains. *Reviews of Modern Physics*, 21:541–583, 1949.
- [21] A. Puzic. *Untersuchungen zur Spindynamik in nanostrukturierten ferromagnetischen Schichtsystemen*. Diplomarbeit, Universität Stuttgart, 2002.
- [22] G. Bertotti. *Hysteresis in Magnetism For Physicists, Materials Scientists, and Engineers*. Academic Press, 1998.

- [23] M. E. Schabes. Micromagnetic theory of non-uniform magnetization processes in magnetic recording particles. *Journal of Magnetism and Magnetic Materials*, 95:249–288, 1991.
- [24] H. Kronmüller and R. Hertel. Computational micromagnetism of magnetic structures and magnetisation processes in small particles. *Journal of Magnetism and Magnetic Materials*, 215–216:11–17, 2000.
- [25] N. A. Usov and S. E. Peschany. Magnetization curling in a fine cylindrical particle. *Journal of Magnetism and Magnetic Materials*, 118:L290–L294, 1993.
- [26] R. Höllinger, A. Killinger, and U. Krey. Statics and fast dynamics of nanomagnets with vortex structure. *Journal of Magnetism and Magnetic Materials*, 261:178–189, 2003.
- [27] H. A. M. van den Berg. Self-consistent domain theory in soft ferromagnetic media. I. Solenoidal distributions in elliptical thin-film elements. *Journal of Applied Physics*, 57:2168–2173, 1985.
- [28] H. A. M. van den Berg. Self-consistent domain theory in soft-ferromagnetic media. II. Basic domain structures in thin-film objects. *Journal of Applied Physics*, 60:1104–1113, 1986.
- [29] H. A. M. van den Berg and A. H. J. van den Brandt. Self-consistent domain theory in soft-ferromagnetic media. III. Composite domain structures in thin-film objects. *Journal of Applied Physics*, 62:1952–1959, 1987.
- [30] W. Scholz, K. Yu. Guslienko, V. Novosad, D. Suess, T. Schrefl, R. W. Chantrell, and J. Fidler. Transition from single-domain to vortex state in soft magnetic cylindrical nanodots. *Journal of Magnetism and Magnetic Materials*, 266:155–163, 2003.
- [31] A. Wachowiak, J. Wiebe, M. Bode, O. Pietzsch, M. Morgenstern, and R. Wiesendanger. Direct observation of internal spin structure of magnetic vortex cores. *Science*, 298:577–580, 2002.
- [32] T. Okuno, K. Shigeto, T. Ono, K. Mibu, and T. Shinjo. MFM study of magnetic vortex cores in circular permalloy dots: behavior in external field. *Journal of Magnetism and Magnetic Materials*, 240:1–6, 2002.
- [33] A. Thiaville, J.M. García, R. Dittrich, J. Miltat, and T. Schrefl. Micromagnetic study of Bloch-point-mediated vortex core reversal. *Phys. Rev. B*, 67:094410, 2003.

- [34] T. L. Gilbert. A Lagrangian formulation of the gyromagnetic equation of the magnetization field. *Phys. Rev.*, 100:1243, 1955.
- [35] I. Neudecker, G. Woltersdorf, B. Heinrich, T. Okuno, G. Gubbiotti, and C. H. Back. Comparison of frequency, field, and time domain ferromagnetic resonance methods. *Journal of Magnetism and Magnetic Materials*, 307:148–156, 2006.
- [36] M. Buess, R. Höllinger, T. Haug, K. Perzlmaier, U. Krey, D. Pescia, M. R. Scheinfein, D. Weiss, and C. H. Back. Fourier transform imaging of spin vortex eigenmodes. *Phys. Rev. Lett.*, 93:077207, 2004.
- [37] M. Buess, T. P. J. Knowles, R. Höllinger, T. Haug, U. Krey, D. Weiss, D. Pescia, M. R. Scheinfein, and C. H. Back. Excitations with negative dispersion in a spin vortex. *Phys. Rev. B*, 71:104415, 2005.
- [38] X. Zhu, Z. Liu, V. Metlushko, P. Grütter, and M. R. Freeman. Broadband spin dynamics of the magnetic vortex state: Effect of the pulsed field direction. *Phys. Rev. B*, 71:180408(R), 2005.
- [39] C. E. Zaspel, B. A. Ivanov, J. P. Park, and P. A. Crowell. Excitations in vortex-state permalloy dots. *Phys. Rev. B*, 72:024427, 2005.
- [40] B. E. Argyle, E. Terrenzio, and J. C. Slonczewski. Magnetic vortex dynamics using the optical Cotton-Mouton effect. *Phys. Rev. Lett.*, 53:190–193, 1984.
- [41] J. P. Park, P. Eames, D. M. Engebretson, J. Berezovsky, and P. A. Crowell. Imaging of spin dynamics in closure domain and vortex structures. *Phys. Rev. B*, 67:020403, 2003.
- [42] J. P. Park and P. A. Crowell. Interactions of spin waves with a magnetic vortex. *Phys. Rev. Lett.*, 95:167201, 2005.
- [43] J. Raabe, C. Quitmann, C. H. Back, F. Nolting, S. Johnson, and C. Buehler. Quantitative analysis of magnetic excitations in Landau flux-closure structures using synchrotron-radiation microscopy. *Phys. Rev. Lett.*, 94:217204, 2005.
- [44] A. A. Thiele. Steady-state motion of magnetic domains. *Phys. Rev. Lett.*, 30:230–233, 1973.
- [45] A. A. Thiele. Applications of the gyrocoupling vector and dissipation dyadic in the dynamics of magnetic domains. *Journal of Applied Physics*, 45:377–393, 1974.

- [46] D. L. Huber. Dynamics of vortices in quasi-two-dimensional planar magnets. *Physics Letters*, 76A:406–407, 1980.
- [47] D. L. Huber. Dynamics of spin vortices in two-dimensional planar magnets. *Phys. Rev. B*, 26:3758–3765, Oct 1982.
- [48] G. M. Wysin. Magnetic vortex mass in two-dimensional easy-plane magnets. *Phys. Rev. B*, 54:15156–15162, 1996.
- [49] S. Hikami and T. Tsuneto. Phase transition of quasi-two dimensional planar system. *Progress of Theoretical Physics*, 63:387–401, 1980.
- [50] M. J. Donahue and D. G. Porter. *OOMMF User's Guide, Version 1.0*. NISTIR 6376, National Institute of Standards and Technology, Gaithersburg, MD, Sept 1999.
- [51] B. T. Thole, P. Carra, F. Sette, and G. van der Laan. X-ray circular dichroism as a probe of orbital magnetization. *Phys. Rev. Lett.*, 68:1943–1946, 1992.
- [52] P. Carra, B. T. Thole, M. Altarelli, and X. Wang. X-ray circular dichroism and local magnetic fields. *Phys. Rev. Lett.*, 70:694–697, 1993.
- [53] G. van der Laan. Angular momentum sum rules for x-ray absorption. *Phys. Rev. B*, 57:112–115, 1998.
- [54] M. Born and E. Wolf. *Principles of optics - 7th ed.* Cambridge University Press, 1999.
- [55] D. Attwood. *Soft x-rays and extreme ultraviolet radiation*. Cambridge University Press, 2000.
- [56] J. Stöhr and H. C. Siegmann. *Magnetism: From Fundamentals to Nanoscale Dynamics*. Springer, 2006.
- [57] C. T. Chen, Y. U. Idzerda, H. J. Lin, N. V. Smith, G. Meigs, E. Chaban, G. H. Ho, E. Pellegrin, and F. Sette. Experimental confirmation of the x-ray magnetic circular dichroism sum rules for iron and cobalt. *Phys. Rev. Lett.*, 75:152–155, 1995.
- [58] C. T. Chen, N. V. Smith, and F. Sette. Exchange, spin-orbit, and correlation effects in the soft-x-ray magnetic-circular-dichroism spectrum of nickel. *Phys. Rev. B*, 43:6785–6787, 1991.

- [59] J. E. Prieto, F. Heigl, O. Krupin, G. Kaindl, and K. Starke. Magneto-optics of Gd and Tb in the soft x-ray resonance regions. *Phys. Rev. B*, 68:134453, 2003.
- [60] G. Schütz, W. Wagner, W. Wilhelm, P. Kienle, R. Zeller, R. Frahm, and G. Materlik. Absorption of circularly polarized x rays in iron. *Phys. Rev. Lett.*, 58:737–740, 1987.
- [61] Y. Kagoshima, T. Miyahara, M. Ando, J. Wang, and S. Aoki. Magnetic domain-specific microspectroscopy with a scanning x-ray microscope using circularly polarized undulator radiation. *Journal of Applied Physics*, 80:3124–3126, 1996.
- [62] W. Chao, B. D. Harteneck, J. A. Liddle, E. H. Anderson, and D. T. Attwood. Soft x-ray microscopy at a spatial resolution better than 15 nm. *Nature*, 435:1210–1213, 2005.
- [63] A. L. D. Kilcoyne, T. Tyliczszak, W. F. Steele, S. Fakra, P. P. Hitchcock, K. Franck, E. Anderson, B. Harteneck, E. G. Rightor, G. E. Mitchell, A. P. Hitchcock, L. Yang, T. Warwick, and H. Ade. Interferometer-controlled scanning transmission x-ray microscopes at the advanced light source. *Journal of Synchrotron Radiation*, 75:125–136, 2003.
- [64] H. Bluhm, K. Andersson, T. Araki, K. Benzerara, G. E. Brown, J. J. Dynes, S. Ghosal, M. K. Gilles, H.-Ch. Hansen, J. C. Hemminger, A. P. Hitchcock, G. Ketteler, A. L. D. Kilcoyne, E. Kneedler, J. R. Lawrence, G. G. Leppard, J. Majzlam, B. S. Mun, S. C. B. Myneni, A. Nilsson, H. Ogasawara, D. F. Ogletree, K. Pecher, M. Salmeron, D. K. Shuh, B. Tonner, T. Tyliczszak, T. Warwick, and T. H. Yoone. Soft x-ray microscopy and spectroscopy at the molecular environmental science beamline at the advanced light source. *Journal of Electron Spectroscopy and Related Phenomena*, 150:86–104, 2006.
- [65] S. Sasaki, K. Kakuno, T. Takada, T. Shimada, K. Yanagida, and Y. Miyahara. Design of a new type of planar undulator for generating variably polarized radiation. *Nuclear Instruments and Methods in Physics Research A*, 331:763–767, 1993.
- [66] S. Sasaki. Analyses for a planar variably-polarizing undulator. *Nuclear Instruments and Methods in Physics Research A*, 347:83–86, 1994.
- [67] A. T. Young, V. Martynov, and H. A. Padmore. Magnetic high-resolution spectroscopy with beamline 4.0.1-2: An elliptically polarizing undulator

- beamline at the advanced light source. *Journal of Electron Spectroscopy and Related Phenomena*, 101–103:885–889, 1999.
- [68] M. R. Howells. Plane grating monochromators for synchrotron radiation. *Nuclear Instruments and Methods*, 177:127–139, 1980.
- [69] T. Warwick, N. Andresen, J. Comins, K. Kaznacheyev, J. B. Kortright, J. P. McKean, H. A. Padmore, D. K. Shuh, T. Stevens, and T. Tyliczszak. *Synchrotron Radiation Instrumentation 2003 AIP Conference Proceedings*, volume 705. 2004.
- [70] H. Petersen. The plane grating and elliptical mirror: a new optical configuration for monochromators. *Optics Communications*, 40:402–406, 1982.
- [71] R. Follath and F. Senf. New plane-grating monochromators for third generation synchrotron radiation light sources. *Nuclear Instruments and Methods in Physics Research A*, 390:388–394, 1997.
- [72] Hamamatsu Photonics - Si APD S2382. <http://www.hamamatsu.com/>.
- [73] Avtech Electrosystems - Bias tee, model AVX-T. <http://www.avtechpulse.com/>.
- [74] Kuhne electronic - Low noise broadband amplifiers, type KU 0180 A & KU 0515 A. <http://www.kuhne-electronic.de/>.
- [75] Avtech Electrosystems - Pulse generators, model AVM-2-PS, AVM-3-PS & AVMR-2-PS. <http://www.avtechpulse.com/>.
- [76] Aeroflex - Digital RF signal generator, type IFR 3416. <http://www.aeroflex.com/>.
- [77] Mini-Circuits - Double balanced frequency mixer, model ZX05-1L. <http://www.minicircuits.com/>.
- [78] M. P. Fahmie. A system for providing high quality triggers to experimental areas. *Proceedings of the 1999 Particle Accelerator Conference, New York*, IEEE Catalog Nr. 99CH36366 2:756–758, 1999.
- [79] Y. Acremann, V. Chembrolu, J. P. Strachan, T. Tyliczszak, and J. Stöhr. Software defined photon counting system for time resolved x-ray experiments. *Review of Scientific Instruments*, 78:014702, 2007.
- [80] Picosecond Pulse Labs - Pickoff tee, model 5370–20 dB Tee. <http://www.picosecond.com/>.

- [81] Mini-Circuits - Bias tee, model ZFBT-6GW-FT. <http://www.minicircuits.com/>.
- [82] Mini-Circuits - Low pass filter, model VLFX-950. <http://www.minicircuits.com/>.
- [83] H. A. M. van den Berg and D. K. Vatvani. Wall clusters in thin soft ferromagnetic configurations. *Journal of Applied Physics*, 52:6830–6839, 1981.
- [84] H. A. M. van den Berg. Conversions of free wall clusters in soft magnetic layers. *Journal of Magnetism and Magnetic Materials*, 27:85–97, 1982.
- [85] H. A. M. van den Berg. Order in the domain structure in soft-magnetic thin-film elements: A review. *IBM J. Res. Develop.*, 33:540–582, 1989.
- [86] S. S. P. Parkin, K. P. Roche, M. G. Samant, P. M. Rice, R. B. Beyers, R. E. Scheuerlein, E. J. O’Sullivan, S. L. Brown, J. Bucchigano, D. W. Abraham, Y. Lu, M. Rooks, P. L. Trouilloud, R. A. Wanner, and W. J. Gallagher. Exchange-biased magnetic tunnel junctions and application to nonvolatile magnetic random access memory. *Journal of Applied Physics*, 85:5828–5833, 1999.
- [87] M. Klaua, D. Ullmann, J. Barthel, W. Wulfhekel, J. Kirschner, R. Urban, T. L. Monchesky, A. Enders, J. F. Cochran, and B. Heinrich. Growth, structure, electronic, and magnetic properties of MgO/Fe(001) bilayers and Fe/Mgo/Fe(001) trilayers. *Phys. Rev. B*, 64:134411, 2001.
- [88] M. Hehn, O. Lenoble, D. Lacour, C. Féry, M. Piécuch, C. Tiusan, and K. Ounadjela. Tunneling magnetoresistance and induced domain structure in Al₂O₃-based junctions. *Phys. Rev. B*, 61:11643–11648, 2000.
- [89] F. Biragnet, J. Devenyi, G. Clerc, O Massenet, R. Montmory, and A. Yelon. Interactions between domain walls in coupled films. *physica status solidi (b)*, 16:569–576, 1966.
- [90] E. Feldtkeller and H. Thomas. Struktur und Energie von Blochlinien in dünnen ferromagnetischen Schichten. *Phys. Kondens. Materie*, 4:8–14, 1965.
- [91] D. Jiles. *Introduction to magnetism and magnetic materials*. New York: Chapman and Hall, 1991.
- [92] W. K. Hiebert, A. Stankiewicz, and M. R. Freeman. Direct observation of magnetic relaxation in a small permalloy disk by time-resolved scanning kerr microscopy. *Phys. Rev. Lett.*, 79:1134–1137, 1997.

- [93] S. B. Choe, Y. Acremann, A. Scholl, A. Bauer, A. Doran, J. Stöhr, and H. A. Padmore. Vortex core-driven magnetization dynamics. *Science*, 304:420–422, 2004.
- [94] V. Novosad, F. Y. Fradin, P. E. Roy, K. S. Buchanan, K. Yu. Guslienko, and S. D. Bader. Magnetic vortex resonance in patterned ferromagnetic dots. *Phys. Rev. B*, 72:024455, 2005.
- [95] K. Yu. Guslienko, B. A. Ivanov, V. Novosad, Y. Otani, H. Shima, and K. Fukamichi. Eigenfrequencies of vortex state excitations in magnetic submicron-size disks. *Journal of Applied Physics*, 91:8037–8039, 2002.
- [96] K. Yu. Guslienko, W. Scholz, R. W. Chantrell, and V. Novosad. Vortex-state oscillations in soft magnetic cylindrical dots. *Phys. Rev. B*, 71:144407, 2005.
- [97] J. P. Zagorodny, Y. Gaididei, D. D. Sheka, J. G. Caputo, K. Yu. Guslienko, and F. G. Mertens. Importance of the internal shape mode in magnetic vortex dynamics. *Phys. Rev. Lett.*, 93:167201, 2004.
- [98] I. N. Bronstein and K. A. Semendjajew. *Taschenbuch der Mathematik*. Verlag Nauka, Moskau, 1989.
- [99] Q. F. Xiao, J. Rudge, B. C. Choi, Y. K. Hong, and G. Donohoe. Dynamics of vortex core switching in ferromagnetic nanodisks. *Appl. Phys. Lett.*, 89:262507, 2006.
- [100] R. Hertel, S. Gliga, M. Fähnle, and C. M. Schneider. Ultrafast nanomagnetic toggle switching of vortex cores. *Phys. Rev. Lett.*, 98:117201, 2007.
- [101] B. Van Waeyenberge, A. Puzic, H. Stoll, K. W. Chou, T. Tyliszczak, R. Hertel, M. Fähnle, H. Brückl, K. Rott, G. Reiss, I. Neudecker, D. Weiss, C. H. Back, and G. Schütz. Magnetic vortex core reversal by excitation with short bursts of an alternating field. *Nature*, 444:461–464, 2006.
- [102] Y. Gaididei, T. Kampeter, F. G. Mertens, and A. R. Bishop. Switching between different vortex states in two-dimensional easy-plane magnets due to an ac magnetic field. *Phys. Rev. B*, 61:9449–9452, 2000.
- [103] T. Eimüller, R. Kalchgruber, P. Fischer, G. Schütz, P. Guttman, G. Schmahl, M. Köhler, K. Prügl, M. Scholz, F. Bammes, and G. Bayreuther. Quantitative imaging of magnetization reversal in FeGd multilayers by magnetic transmission x-ray microscopy. *Journal of Applied Physics*, 87:6478–6480, 2000.

- [104] S. Kahn. Short radiation pulses in storage rings. *Proceedings of FLS 2006, Hamburg, Germany*, page PLT14.
- [105] D. Chumakov, J. McCord, R. Schäfer, L. Schultz, H. Vinzelberg, R. Kaltofen, and I. Mönch. Nanosecond time-scale switching of permalloy thin film elements studied by wide-field time-resolved Kerr microscopy. *Phys. Rev. B*, 71:014410, 2005.

LIST OF FIGURES

2.1	Precessional motion of the magnetization.	9
2.2	Illustration of the formation of domains and the corresponding stray field.	12
2.3	Illustration of two types of 180° domain walls.	13
2.4	Illustration of magnetic structures with a single vortex.	15
2.5	Damped precessional motion of the magnetization.	17
2.6	Illustration of the relation between the sense of gyration of a magnetic Landau structure and the direction of the out-of-plane vortex core magnetization.	20
3.1	The electromagnetic spectrum from the infrared (IR) to the x-ray regions.	21
3.2	Illustration of the XMCD effect for the absorption at the <i>L</i> edge in Fe.	23
3.3	Schematic layout of the Molecular Environmental Science (MES) beamline (11.0.2) at the Advanced Light Source.	25
3.4	Illustration of narrow cone undulator radiation that is generated by electrons traversing a periodic magnet structure.	26
3.5	Schematic view of the magnetic structure for generating variably polarized undulator radiation.	27
3.6	Spectral photon flux and brightness from the elliptically polarizing undulator at the Advanced Light Source in circular and elliptical mode.	29
3.7	Principle monochromator	30
3.8	Illustration of the time structure in the ALS storage ring for multi bunch operation.	31
3.9	Principle drawing of a scanning transmission x-ray microscope.	32
3.10	Illustration of a zone plate.	33
3.11	Block diagram of the amplifier chain for the amplification of the APD signals.	37
3.12	Time-resolved scanning transmission x-ray microscopy.	38

3.13	Different types of striplines for the generation of an in-plane magnetic field.	39
3.14	Illustration of the sample/stripline setup.	40
3.15	Illustration of the stroboscopic measuring technique with pulsed and sine excitation.	41
3.16	Illustration of the burst excitation.	42
3.17	Experimental setup for pulsed excitation.	43
3.18	Experimental setup for sine excitation.	44
3.19	Experimental setup for burst excitation.	45
4.1	Static images taken for zero external field at two different polarization of the photons.	48
4.2	Static images taken for zero external field at the L_3 absorption edges of Ni (852.7 eV) and Co (778.1 eV).	51
4.3	Direct observation of the vortex core on absence of an external magnetic field.	53
5.1	Differential imaging – look-up table I.	57
5.2	Differential imaging – look-up table II.	58
5.3	Dynamic response for a $1\ \mu\text{m} \times 1\ \mu\text{m}$, 40 nm thick element, observed by pulsed excitation in multibunch mode.	60
5.4	Dynamic response for a $1.5\ \mu\text{m} \times 1.5\ \mu\text{m}$, 40 nm thick element, observed by pulsed excitation in multibunch mode.	61
5.5	Resonance frequency as a function of the aspect ratio, observed by pulsed excitation in multibunch mode.	62
5.6	Gyrotropic motion for a $1.5\ \mu\text{m} \times 1.5\ \mu\text{m}$, 50 nm thick vortex structure – in-plane magnetization configuration.	63
5.7	Vortex core displacement as a function of the amplitude of the alternating magnetic field for a $1.5\ \mu\text{m} \times 1.5\ \mu\text{m}$, 40 nm thick Permalloy element.	65
5.8	Dynamic response for a $640\ \text{nm} \times 960\ \text{nm}$, 40 nm thick ellipse.	66
5.9	Gyrotropic motion for a $1\ \mu\text{m} \times 1\ \mu\text{m}$, 50 nm thick vortex structure.	67
5.10	Gyrotropic motion for a $500\ \text{nm} \times 500\ \text{nm}$, 40 nm thick vortex structure.	68
5.11	Gyrotropic motion for a $200\ \text{nm} \times 200\ \text{nm}$, 40 nm thick vortex structure.	69
5.12	In-plane burst excitation of a $1.5\ \mu\text{m} \times 1.5\ \mu\text{m}$, 50 nm thick Permalloy sample.	71

5.13	Differential images for a $1.5 \mu\text{m} \times 1.5 \mu\text{m}$, 50 nm thick vortex structure excited by an in-plane field burst.	72
5.14	Dynamic response of a $1.5 \mu\text{m} \times 1.5 \mu\text{m}$ trilayer system, composed of Permalloy(20 nm)/Cu(5 nm)/Co(20 nm).	74
5.15	Gyrotropic motion for a $1.5 \mu\text{m} \times 1.5 \mu\text{m}$, 50 nm thick vortex structure – low power state.	76
5.16	Gyrotropic motion for a $1.5 \mu\text{m} \times 1.5 \mu\text{m}$, 50 nm thick vortex structure – high power state.	77
5.17	Illustration of the trajectories of a vortex structure, before and after the reversal process, in case of a horizontal stripline.	78
5.18	Gyrotropic motion for a $1.5 \mu\text{m} \times 1.5 \mu\text{m}$, 40 nm thick vortex structure – hairneedle stripline.	79
5.19	Gyrotropic motion for a $500 \text{ nm} \times 500 \text{ nm}$, 40 nm thick vortex structure – out-of-plane magnetic contrast.	80
5.20	Hysteresis behaviour for a $1.5 \mu\text{m} \times 1.5 \mu\text{m}$, 50 nm thick Permalloy element.	82
5.21	Hysteresis behaviour for a $1.5 \mu\text{m} \times 1.5 \mu\text{m}$, 50 nm thick Permalloy element with asymmetric edge.	83
5.22	Gyrotropic motion for a $1.5 \mu\text{m} \times 1.5 \mu\text{m}$, 50 nm thick vortex structure – before burst excitation.	84
5.23	Gyrotropic motion for a $1.5 \mu\text{m} \times 1.5 \mu\text{m}$, 50 nm thick vortex structure – after burst excitation.	85
5.24	Gyrotropic motion for a $500 \text{ nm} \times 500 \text{ nm}$, 40 nm thick vortex structure – out-of-plane magnetic contrast.	87
5.25	Micromagnetic simulation for a $500 \text{ nm} \times 500 \text{ nm}$, 40 nm thick vortex structure – reversal mechanism.	88
5.26	Gyrotropic motion for a Permalloy disk with a diameter of $2 \mu\text{m}$ and a thickness of 50 nm – multiple levels.	92
5.27	Gyrotropic motion for a Permalloy disk with a diameter of $2 \mu\text{m}$ and a thickness of 50 nm – thresholds of the switching levels.	93
5.28	Gyrotropic motion for a Permalloy disk with a diameter of $2 \mu\text{m}$ and a thickness of 50 nm – phase shift at higher field amplitudes.	94
5.29	Hysteresis behaviour for a $500 \text{ nm} \times 500 \text{ nm}$, 40 nm thick Permalloy element.	95
5.30	Hysteresis behaviour for a $500 \text{ nm} \times 500 \text{ nm}$, 40 nm thick vortex structure – gyrotropic motion.	96
5.31	Vortex core velocity as a function of the amplitude of the alternating magnetic field for a $500 \text{ nm} \times 500 \text{ nm}$, 40 nm thick Permalloy element.	97

5.32	Illustration of the asymmetry in the vortex core trajectories.	99
5.33	Dynamic response for a $1.5 \mu\text{m} \times 1.5 \mu\text{m}$, 50 nm thick vortex structure – domain wall dynamics.	100
A.1	Illustration of the synchrotron radiation source at the ALS.	110
B.1	Field calculations for a stripline.	111

LIST OF TABLES

2.1	Typical material parameters for several magnetic materials.	14
3.1	Photon energy ranges for the EPU polarization modes at the Advanced Light Source (ALS), operated by the Lawrence Berkeley National Laboratory in California (USA).	28
3.2	Zone plate parameters.	35
3.3	General characteristics of Hamamatsu Si APD S2382.	36
3.4	Specifications Avtech pulse generators.	40
A.1	Typical parameters of the storage ring for the Advanced Light Source (ALS), operated by the Lawrence Berkeley National Laboratory in California (USA).	109
B.1	Conversion table for the field amplitude.	112

LIST OF PUBLICATIONS

Before PhD period:

- J. Heyse, C. Wagemans, K. W. Chou, L. De Smet, J. Wagemans, and O. Serot. High resolution measurements of the $^{234}\text{U}(n,f)$ cross section. *Proceedings of the Seminar on fission – Pont d'Oye V*, p. 255–261, 2003.
- M. Agundez, D. Ruiz, S. Van Petegem, J. De Baerdemaeker, K. W. Chou, D. Segers, and Y. Houbaert. Defect study on deformed FeSi alloys by positron annihilation techniques. *phys. stat. sol. (a)*, 202:1751-1757, 2005.
- K. W. Chou, J. De Baerdemaeker, V. Peral, D. Ruiz, Y. Houbaert, and D. Segers. Defect study on deformed FeSi alloys by positron annihilation techniques. *Acta Physica Polonica A*, 107:799–804, 2005.

During PhD period:

- A. Puzic, B. Van Waeyenberge, K. W. Chou, P. Fischer, H. Stoll, G. Schütz, T. Tyliczszak, K. Rott, H. Brückl, G. Reiss, I. Neudecker, T. Haug, M. Buess, and C. H. Back. Spatially resolved ferromagnetic resonance: Imaging of ferromagnetic eigenmodes. *Journal of Applied Physics*, 97:10E704, 2005.
- K. W. Chou, A. Puzic, H. Stoll, G. Schütz, B. Van Waeyenberge, T. Tyliczszak, K. Rott, G. Reiss, H. Brückl, I. Neudecker, D. Weiss, and C. H. Back. Vortex dynamics in coupled ferromagnetic multilayer structures. *Journal of Applied Physics*, 99:08F305, 2006.
- B. Van Waeyenberge, A. Puzic, H. Stoll, K. W. Chou, T. Tyliczszak, R. Hertel, M. Fähnle, H. Brückl, K. Rott, G. Reiss, I. Neudecker, D. Weiss, C. H. Back, and G. Schütz. Magnetic vortex core reversal by excitation with short bursts of an alternating field. *Nature*, 444:461–464, 2006.
- K. Kuepper, L. Bischoff, Ch. Akhmadaliev, J. Fassbender, H. Stoll, K. W. Chou, A. Puzic, K. Fauth, D. Dolgos, G. Schütz, B. Van Waeyenberge, T. Tyliczszak, I. Neudecker, G. Woltersdorf, and C. H. Back. Vortex dynamics in Permalloy disks with artificial defects: Suppression of the gyrotropic mode. *Applied Physics Letters*, 90:062506, 2007.

- K. W. Chou, A. Puzic, H. Stoll, D. Dolgos, G. Schütz, B. Van Waeyenberge, A. Vansteenkiste, T. Tyliczszak, G. Woltersdorf, and C. H. Back. Direct observation of the vortex core magnetization and its dynamics. *Applied Physics Letters*, 90:202505, 2007.

KANG WEI CHOU

CURRICULUM VITAE

- 10.1.1980 born in Mouscron, Belgium
Belgian nationality
- 1986 – 1992 Sint-Joris Basisschool Menen, Belgium – primary school
- 1992 – 1998 Sint-Aloysiuscollege Menen – high school
- 1998 – 2000 first cycle in civil engineering at the university of Ghent, Belgium
- 2000 – 2003 second cycle in engineering physics at the university of Ghent
thesis: fission cross section measurements and
applications in transmutation
- 2003 – 2004 scientific researcher at the university of Ghent
topic: defect studies of metal alloys by means of
positron annihilation techniques
- 1.10.2004 – ... PhD student at the Max Planck Institute for Metals Research in
Stuttgart – Department Schütz

"Goodbye for now, and good mental health!"
— DR. FRASIER CRANE